UNIVERSITÉ GRENOBLE ALPES

THÈSE

pour obtenir le grade de

DOCTEUR DE L'UNIVERSITÉ GRENOBLE ALPES

Spécialité : **Signal, Image, Parole, Télécoms**

Arrêté ministériel : 7 août 2006

Présentée par
Cindy BERNARD

Thèse dirigée par **Cornel IOANA**

préparée au sein du laboratoire
Grenoble Images Parole Signal Automatique (GIPSA-Lab)
dans **l'Ecole Doctorale d'électronique, électrotechnique, automatique et traitement du signal (EEATS)**

Caractérisation des phénomènes physiques par analyse parcimonieuse des signaux transitoires

Thèse soutenue publiquement le **24 septembre 2015**,
devant le jury composé de:

Marie CHABERT
PR INP-ENSEEIHT Toulouse, Rapporteur
Alexandru SERBANESCU
PR Académie technique militaire de Bucarest - Roumanie, Rapporteur
Jérôme MARS
PR Grenoble-INP, Examinateur, Président du jury
Ramon MIRALLES
eq. MCF Université polytechnique de Valence - Espagne, Examinateur
Antonia PAPANDREOU-SUPPAPPOLA
PR Arizona State University - Etats-Unis, Examinateur
Srdjan STANKOVIC
PR Universiré du Monténégro, Examinateur
Alexandre GIRARD
ING EDF R&D, Examinateur
Cornel IOANA
MCF Grenoble-INP, Directeur de thèse

Remerciements/Acknowledgements

Tout d'abord, j'aimerais remercier les membres de mon jury de thèse: les rapporteurs Mme Marie Chabert et M. Alexandru Serbanescu, le président M. Jérôme Mars, et les examinateurs Mme Antonia Papandreou-Suppappola, M. Ramon Miralles, M. Srdjan Stankovic et M. Alexandre Girard. Ces scientifiques extraordinaires m'ont accordé un grand honneur en acceptant d'évaluer mes travaux de thèse et je leur en suis très reconnaissante. Donc merci beaucoup pour vos retours constructifs!

Ces travaux de thèse n'auraient bien évidemment jamais eu lieu sans mon directeur de thèse M. Cornel Ioana : c'est donc à lui que j'adresse mes plus grands remerciements. Merci de m'avoir aiguillée, de m'avoir fait confiance tout au long de ces 5 dernières années et de m'avoir permis de voyager dans le cadre de nombreuses collaborations internationales. Tout ceci n'aurait pas pu être possible sans lui!

I would like to thank all the people I met during my stay in Podgorica, Montenegro: Professor Srdjan, Mrs Irena Orovic and Andjela Draganic. It was a great pleasure to discuss science and history over coffee with the three of you!

I would like to thank all the people I met during my stay in Toronto and that will probably never read those lines: Hasan, Dr Krishnan, Tristan, Justine, Adrien, Sybille, Mélissandre, Martin, Lucie, Mario, Sarah, Julia, Laetitia, Audrey, Olivier, Hugo, Valentin et Noémie. This stay would not have been the same without all of you!

I also would like to thank all the people I met during my stay at the Arizona State University in Tempe, AZ, and more especially Professor Antonia Papandreou-Suppappola. She was so kind and so welcoming, I was not sure I wanted to go back to France! :D I also would like to thank John, Jessie, Meng and Brian from the lab. I did not stay long but they knew how to make me feel confortable and I really enjoyed the hot chinese restaurant. Thank you as well to Matt for letting me stay at his place for an entire month and inviting me to an awesome weekend in the Arizona desert. Thank you as well to Ellen, and her sons Nathan and Mitchell for giving me so many great talks. It was a great pleasure meeting you all!

Une thèse au Gipsa ne serait bien évidemment pas une thèse réussie sans la participation de toutes les personnes qui font vivre le laboratoire. Je remercie donc mes chers collègues et amis du bureau D1146 : Céline, Arnaud, Raluca, Pascal, Fardin, Rafael, Fakri et Tuan pour tous ces bons moments que nous avons pu partager ensemble! Les rails de café, les cartes postales kitsch, les shokobons, le thé, les vidéos de chats, les gros titres du 20 minutes, le tableau des humeurs, les plantes ikéa, les pourrissages de bureau, etc... Puis tous les gens des bureaux annexes rencontrés lors des innombrables pauses café, des repas du midi et des coinches: Florian, Romain, Quentin, Tim, Tim, Edouard, Ion, Lucas, Raphaël, Aude, Robin, Taïamiti, Alexis, Rémy, Guillaume, Maël, Maëlle, Miguel, les bébés doctorants, etc... J'en oublie certainement, mais c'est involontaire! La liste des personnes à remercier est bien longue et ma mémoire commence à décliner!! ;)

Je continue en remerciant également les différentes générations du Gipsadoc qui nous ont organisé de superbes activités et de super rencontres internationales d'hiver et d'été! Un grand merci également à Emmanuelle pour son soutien lors des CDL. Sans toi, l'expérience n'aurait pas été la même...

J'aimerais également remercier Lucia qui sait prendre soin de tous les doctorants et avec qui j'ai pu échanger de nombreuses fois! La vie du labo n'aurait pas été la même sans toi! Merci pour tout... Merci de nous apprendre à nous défendre, merci de nous donner les informations manquantes, et merci de nous nourrir avec tous les restes des workshops!! :D

J'aimerais aussi remercier tous mes amis de Grenoble et d'ailleurs, qui sont toujours là pour moi quand j'en ai besoin: Sovannarita, Pierre, Guillaume et Isabelle, Cyrielle, Arthur, Virginie et Emerick. Une mention spéciale également pour Sova, son frère et ses parents que je considère comme ma famille adoptive sur Grenoble! Merci de prendre soin de moi et de m'avoir accueillie comme l'une des vôtres...

Je voudrais de plus remercier Dr Laurent Olivier, Dr Bruno Wirtz, Dr Jo Kovacik et Laurent Forelle pour tous ces magnifiques étés que nous avons passés ensemble. Ma vie n'aurait également pas été la même sans tous ces bons moments à fouiller dans la boue et à chercher des barrettes de chite. :D

Pour finir, j'adresse un merci tout spécial à l'ensemble de ma famille sans laquelle je ne serais pas là aujourd'hui! Un grand merci à mes parents Marie-Laure et Didier: sans votre soutien je ne sais pas ce que je ferai!! à ma soeur Pauline, mon frère Emilien et mon neveu Noah pour exister tout simplement! :D à mon grand père Jean-Claude, ma tante Sylvie et mon oncle Philippe qui sont toujours présents pour mes remises de diplômes! Merci également au reste de la famille qui est toujours là au moins par la pensée: Elodie et Bastien, Mathilde et Solène, Alexia, Nathan, Martin, Sandrine et Michel, Fanny et Laurent, Tata Madeleine et Tonton Jean, Hélène. Un énorme merci également à Christiane et Pascal, Jean-Yves, Christine et Jean-Pierre. Bien que les liens du sang n'existent pas, vous faites bel et bien tous partie de la famille! :D Merci également à Benoit pour continuer à me supporter tout simplement!

Merci encore une fois à tous!

Contents

List of Figures

List of Tables

Table of acronyms and abbreviations

CS	Compressive Sensing
ECG	Electrocardiography
EMD	Empirical Mode Decomposition
GCD	Generalized Complex-time Distributions
GCM	Generalized Complex-time Moment
HOS	High Order Statistics
IFL	Instantaneous Frequency Law
IMF	Intrinsec Mode Function
MLPDA	Multi-Lag Phase Diagram Analysis
MSE	Mean Square Error
NMPS	Nonlinear Modulation Phase Signal
PD	Partial Discharge
PDA	Phase Diagram Analysis
PDL	Phase Derivative Law
RPA	Recurrence Plot Analysis
RQA	Recurrence Quantification Analysis
STFT	Short Time Fourier Transform
SVD	Singular Value Decomposition
TF	Time-Frequency
TS	Time-Scale
WBCS	Warping-based Compressive Sensing

Introduction

Transient signal representation

Transient signal analysis is a complex problem since signals with very short duration are characterized by a reduced number of samples. Although different representations can be used to analyze transient signals, it is difficult to decompose them into appropriate basis functions.

The general aim of this thesis is to propose and investigate alternative analysis methods that explore the transient signals characteristics of exhibiting sudden changes in their parameters. Specifically, we consider the general signal representation for a transient signal:

$$s(t) = A(t)\, e^{j\Phi(t)} \tag{1}$$

where $A(t)$ is the instantaneous amplitude parameter and $\Phi(t)$ is the instantaneous phase parameter. Based on how these parameters change, the thesis studies the following three different types of transient signals that are commonly found in real-life applications.

Transient signals characterized by phase discontinuities of a particular order

When the transient signal in (1) exhibits phase discontinuities, then it can be modeled as:

$$s(t) = \sum_k A_k e^{j a_k \cos(2k\pi t)} \tag{2}$$

where A_k is the instantaneous amplitude parameter of the K^{th} component and a_k is the amplitude of its instantaneous phase parameter.

In particular, the transient signal has multiple components whose instantaneous phase is a high-order (infinite) derivable function. The high nonlinearity of this function makes the signal analysis quite complicated, and new representation methods are then required. Such signals are encountered in several applications where the micro-Doppler effect is present, such as radar [STD06, TAR+07] and acoustics [Jos10].

Transient signals characterized by sudden amplitude changes

Transient signals that are characterized by sudden amplitude changes are usually present in mechanical, electrical, electromagnetic phenomena. Such signals can be given by:

$$s(t) = A(t) \;\; t \in [t_0, t_0 + D] \tag{3}$$

where the duration D is assumed much shorter than the signal's observation time, and t_0 is the starting time of the signal. The amplitude function $A(t)$ of the signal in (3) is assumed to have high order derivatives.

The methods proposed in our work will contribute to offer a potential interesting solution, attempting to provide a general analysis framework of such signals.

An example of a transient signal in (3) is the electrocardiogram (ECG) as it is characterized by typical variations of amplitude. Another widely encountered case, that is a major part of our study, is a signal that is observed at a given distance from the source and that consists of not only a transient at the origin (as it is generated by the phenomenon) but also of propagation and receiver processing effects. Two application examples of such signals are as follows:

- Electrical transients

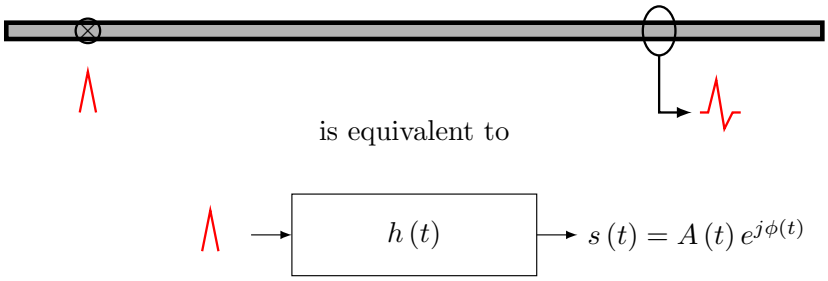

Figure 1: The propagation of an electrical transient through a cable is really complicated to model due to the diversity of the physical phenomena involved, such as dispersion and reflections.

Electrical transient analysis is of capital importance for power networks surveillance. Phenomena that generate such transient signals include partial discharge (PD) (Figure 1) and electrical arches. These phenomena have been extensively studied as they are important for the health management of the power distribution. Some studies strictly attempted to model analytically the transients generated by these phenomena. As in any modeling, the assumptions made are not always valid and this restricts the generalization of these models. In addition, the analysis can be complex as the sensors are often far from the source.

- Acoustic pressure transients in passive configurations

Another example of capital importance for hydropower production surveillance is the passive monitoring of hydraulic shocks in penstock pipes (Figure 2). Water hammer is a pressure surge caused when a fluid in motion is forced to stop or change direction suddenly. Such pressure surges commonly occur when a valve is closed at an end of a pipeline system, and a pressure wave propagates in the pipe. Although these surges are inevitable, they can be really dangerous if the wave does not propagate as designed by the engineer, resulting in multiple system damages. Some characteristics of the transients are of great interest as they reflect the propagation of the shock wave and can reveal if the penstock has been damaged.

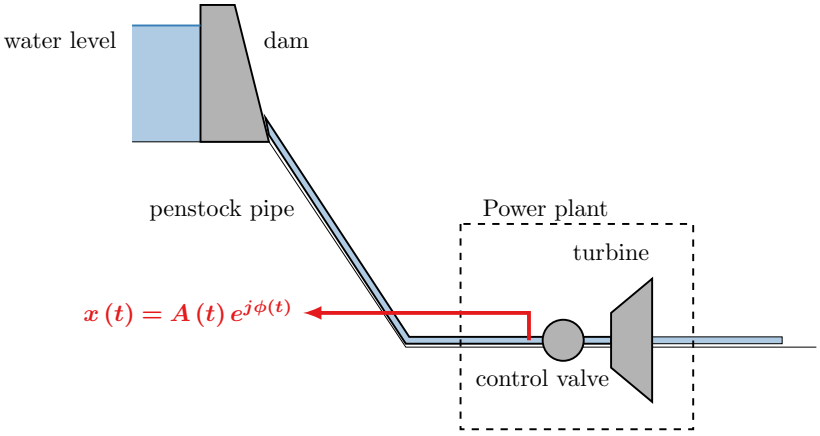

Figure 2: General illustration of a hydraulic power plant. Acoustic pressure transients are usually recorded before the control valve in order to monitor the hydraulic shocks.

Transient signals characterized by nonlinear variation of the instantaneous phase

$$s(t) = A(t)\, e^{j(2\pi f_0 t + \Phi(t))},\ \Phi(t) \in \mathcal{C}^4 \tag{4}$$

Tansient signals whose instantaneous phase varies nonlinearly often appear in real-life applications as typical natural signals. Examples include the signals emitted by bats or mammals [HCIS98] which are well adapted to the propagating environment (Figures 3 and 4[1]).

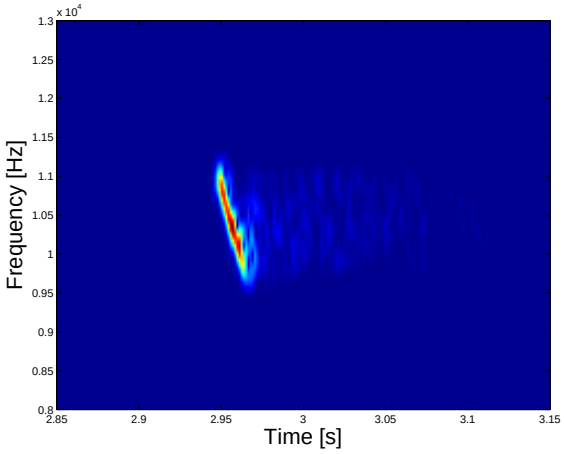

Figure 3: Spectrogram of an echolocation bat signal.

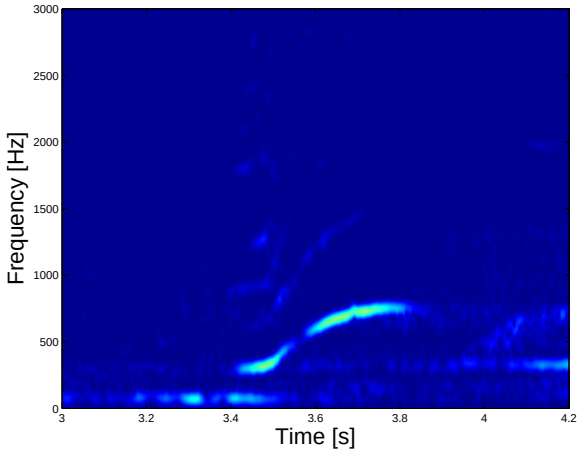

Figure 4: Spectrogram of a signal emmitted by a whale.

Othe examples include the signals obtained during sensing of an environment (Figure 5),in order to estimate important environment parameters. The transmission and propagation of acoustic transients in environments characterized by distortions such as multipath and

[1]Sounds bank `www.universal-soundbank.com/bruitages-animaux.htm`

frequency dependent attenuation, are important to study in order to ensure the efficiency of acoustic sensing that aims to characterize the environment.

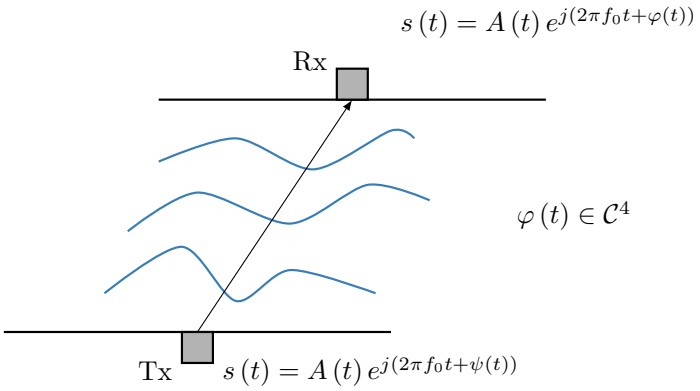

Figure 5: Depiction of active acoustic sensing.

Transient signal analysis approaches

There are several approaches for analyzing transient signals. Three of such approaches include: statistical approach, linear projection-based approach, and data-driven analysis. There are advantages and disadvantages to these different approaches, as discussed in Chapter 1. These approaches show the importance of transient analysis in many contexts. Although some of these methods are used for signal detection, other characterizations are also needed to extract additional knowledge for discrimination or classification purposes.

The approaches proposed in our work are included in the three main types and will contribute over a potential interesting solution, attempting to provide a general analysis framework for transient signals. In further chapters, the improvement provided by the proposed techniques will be compared with the state of the art.

Thesis organization

The thesis is organized as follows. In Chapter 1, we discuss three approaches commonly used to analyze transient signals: the statistical approach, linear projection-based approach and data-driven approach.

Then, Chapter 2 adresses the problem of projective approaches for the representation of signals having fast-varying time-frequency components, and is divided into two parts. First part focuses on complex time distributions as a way to produce high concentrated distributions along the different phase derivatives of a signal. The actual method presents a major drawback as its utilization is limited to narrow band signals. We propose to expand it to deal with time-frequency structures with larger bandwidth. The second part aims to recover signals having

nonlinear modulation phase signals disturbed by nonstationary and other coherent signals. Generally performed by tracking algorithms, those signals are of great interest as they are well adapted to dispersive environments. However, if they overlap in time and frequency or if parts of the signals are missing, tracking algorithms usually fail to provide a good estimation. The proposed method for separation and extraction combines warping operators and compressive sensing to successfully achieve this goal. A comparison with a classical approach is also provided to compare the results.

Chapter 3 then focuses on the study of signals having sudden amplitude changes by data-driven techniques. We design the concept of multi-lag phase diagram analysis that takes advantage of the lag diversity in phase diagram to explore similarities between transients. To do so, parsimonious parameters are extracted from each phase space representations and their evolution is then compared with respect to the lags. The different parameters and their extractions are presented and examples are provided.

In Chapter 4, we present some applications that show the potential of the proposed approaches developed in the previous chapters to some real-life contexts. We first propose a new framework for ECG time-series segmentation, then work on electrical transient characterization, some results in passive acoustic for hydraulic power plant, and finally, we present the characterization of simulated acoustic transients obtained in an active configuration.

In conclusion, we present a synthesis of our thesis, the main contributions we proposed and some perspectives for further works.

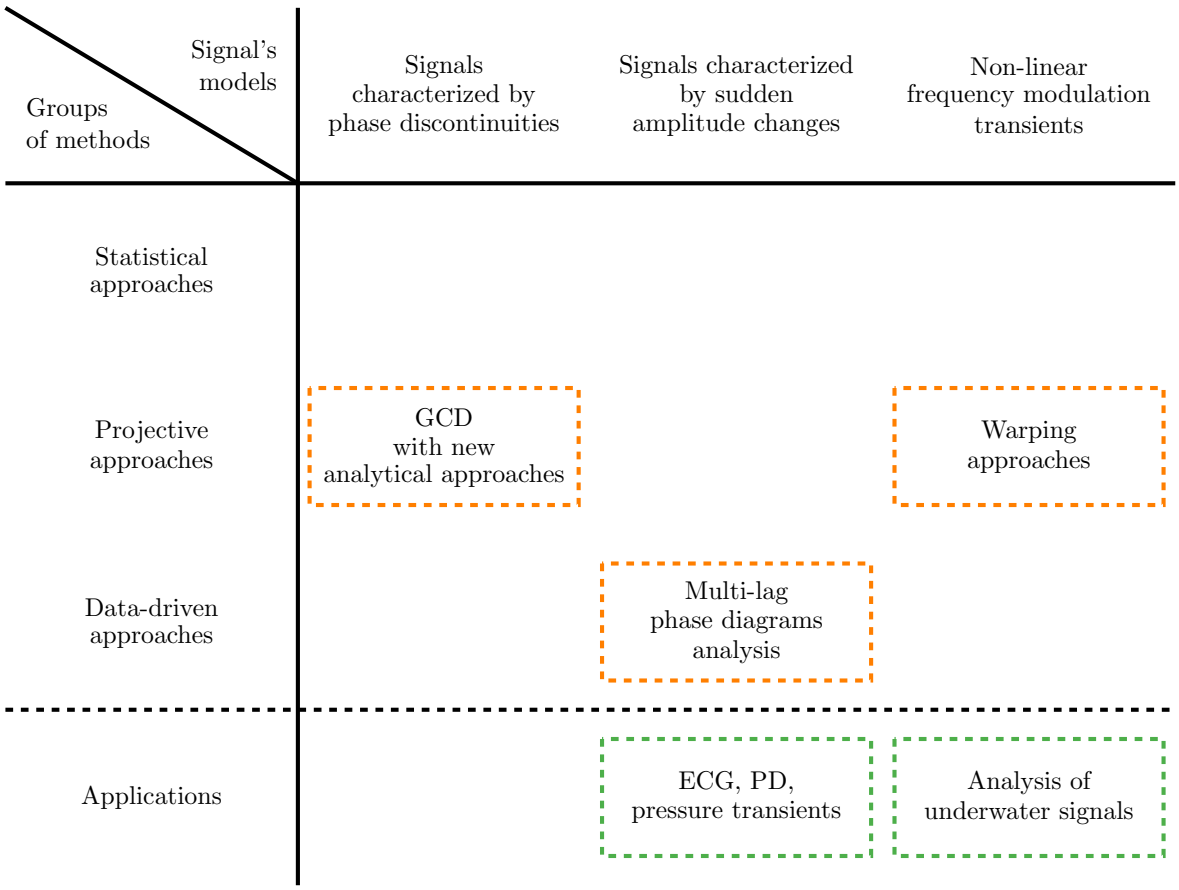

Figure 6: Overall thesis structure

Chapter 1

Brief overview of transient analysis methods

Contents

The signal types discussed in the previous section were subject of an uncountable number of works. The description of all the method types is a very difficult and complex task, because of the multitude and the diversity of the existing approaches. Without pretending to provide an extensive classification of the existing techniques, we propose to organize the techniques into three different classes of approaches according to the way how the signal behaviour is considered.

1.1 Statistical approaches

This very wide analysis domain considers signals as series of samples:

$$s(t) = \{s(t_i)\}_{i=1,\dots,N} \tag{1.1}$$

and then studies their statiscal properties as if they were random variables. Two well-known measurements that are usually calculated on them are the mean μ and the variance μ_2 defined as follows:

$$\mu = \mathbb{E}[s] \tag{1.2}$$

$$\mu_2 = \mathbb{E}\left[s^2\right] \tag{1.3}$$

where $\mathbb{E}$ denotes the average over the probability distribution.

The same way, high order statistics HOS refers to functions which use the third or higher order moment of a sample [LAC97]. We defined the n-th order moment μ_n of signal s as follows:

$$\mu_n = \mathbb{E}[s^n] \tag{1.4}$$

Statistic approaches are mainly based on the supposition that transients do not have a Gaussian histogram. This is the feature that distinguished them from noise which is supposed to be Gaussian. As an example, the third moment known as the skewness is a measure of the asymmetry of the signal probability distribution, while the fourth moment (known as kurtosis) refers to its peakedness.

Although the statistical approaches allow us making the consideration concerning the transient nature of signals, being very useful for detection (especially in conjunction with time-frequency and time-scale representation [RA98, RA01]) the fine characterization of transients is not guaranteed.

1.2 Linear projection-based approaches

It is in human nature to compare things with what they know. This philosophical statement finds a equivalent in signal processing, materialized by the decomposition of any signal $s(t)$ in a set of elementary functions belonging to a dictionnary $\mathcal{D}$.

$$s(t) = \sum_{\Theta} C_{\Theta} \psi_{\Theta}(t) \tag{1.5}$$

where $\psi_{\Theta}(t)$ is the elementary function characterized by the set of parameters Θ and C_{Θ} are the projection coefficients showing by their amplitude what is the contribution of $\psi_{\Theta}(t)$ in the structure of $s(t)$. These coefficients are generally computed by the inner product:

$$C_{\Theta} = \langle s(t), \psi_{\Theta}(t) \rangle \tag{1.6}$$

$$= \int_t s(t) \psi^*_{\Theta}(t) \, dt \tag{1.7}$$

Among the possible infinite (large number of choices), let us recall few well-known representation based on the signal projection.

The Fourier transform

The well-known Fourier transform allows to express a signal $s(t)$ in terms of sinusoids of different frequencies by using the elementary functions defined as below:

$$\psi_k(t) = e^{2j\pi f_k t} \tag{1.8}$$

where f_k corresponds to the frequency.

Therefore, the Fourier transform $S(f)$ of the signal $s(t)$ is calculated as follows:

$$S(f) = \int_{-\infty}^{\infty} s(t) e^{-2j\pi f t} dt \tag{1.9}$$

The major advantage of this central signal analysis tool is that all the frequency content of the signal can be analyzed with the Fourier transform. However, if the studied signal is nonstationary, the frequency content might change over time and then not be the same at two different instants of observation. That is, this property limits the study of transient signals; this is why the Short Time Fourier transform was developed in order to analyze the frequency content of nonstationary signals over time.

The Short Time Fourier transform (STFT)

The Short-time Fourier transform (STFT) is one of the most famous time-frequency representation methods used to study nonstationary signals and is a straightforward extension of the Fourier transform. The signal is decomposed in a basis of windowed elementary function defined as:

$$\psi_{k,n}(t) = h(t - kT)\, e^{2j\pi f_n t} \tag{1.10}$$

where T corresponds to the duration of the window $h(t)$.

It enables to evaluate the frequency content of a signal over time. The general formulation is as follows:

$$STFT[s(t)] = X(\tau, f) \tag{1.11}$$

$$= \int_{-\infty}^{\infty} s(t)\, w(t - \tau) \exp^{-j2\pi f t}\, dt \tag{1.12}$$

When dealing with the energetic version of the STFT, we speak about the spectrogram:

$$\rho(\tau, f) = |X(\tau, f)|^2 \tag{1.13}$$

Those representations are really famous for non-stationary signal analysis, however, they still present a drawback materialized by a trade-off between the resolution in frequency and the resolution in time known as the Heisenberg uncertainty [Coh95]. If someone wants to obtain a good localization of a phenomenon, he needs to choose a window of small duration that then leads to a poor resolution in frequency. On the contrary, a good resolution in frequency is achieved by a larger window that then provides a bad localization in time. To overcome this limitation, windows can be overlapped to improve the resolutions, but the trade-off would still exists.

The Wavelet Transform

The wavelet transform [Mal99, MS95, Dau90, Dau92] is used to decomposed a signal $s(t)$ in an orthonormal basis constructed from a family of functions $\psi_{n,m}(t)$ called wavelets:

$$\psi_{n,m}(t) = \frac{1}{\sqrt{2^m}} \psi_0 \left(\frac{t}{2m} - n \right) \tag{1.14}$$

where $\psi_0(t)$ corresponds to the mother wavelet, m is the dilation factor and n is the translation.

The idea is to propose an orthonormal basis that is elaborated from a mother wavelet $\psi_0(t)$ and its dilated and delayed wavelets. The signal is then projected onto this basis in order to know with which scale and delay the similarity is the most important.

$$W_\psi s(n,m) = \int_{-\infty}^{\infty} s(t)\, \psi^*_{n,m}(t)\, dt \tag{1.15}$$

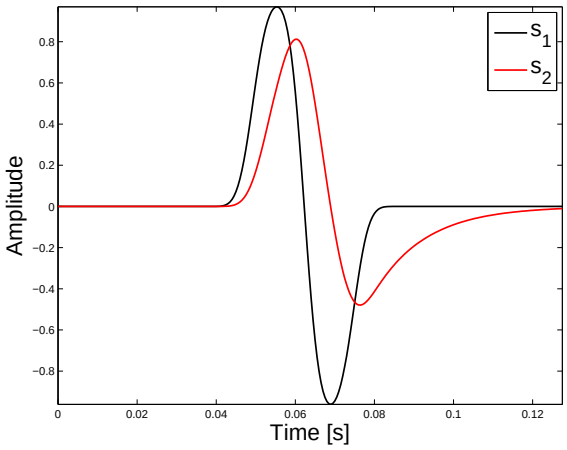

Figure 1.1: Studied signals.

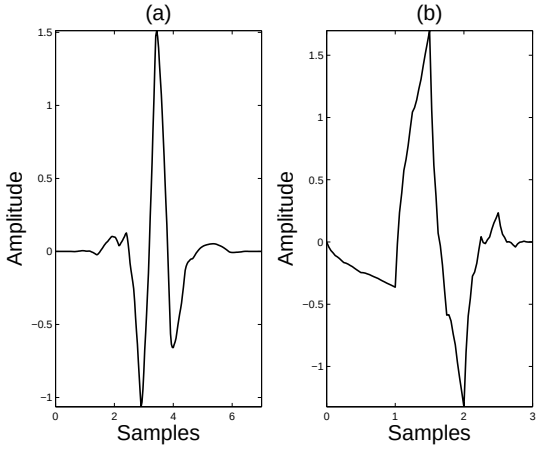

Figure 1.2: (a) Symlet mother wavelet. (b) Daubechies 2 mother wavelet.

It is well-known that a good wavelet representation requires the definition of the appropriate mother wavelet. In order to illustrate this matter, let consider two signals $s_1(t)$ and $s_2(t)$ that are related by a low pass filtering and the two following mother wavelets: Symlet and Daubechies (Figure 1.2). As we can see in Figure 1.1, the two signals are really similar because they have almost the same shape and their frequency content are almost identical. The two selected mother wavelets are quite different and it seems that the Daubechies wavelet has the closest shape to the analyzed signals. We perform a time-scale decomposition for both signals using the two wavelets. Results are displayed in Figure 1.3. As we can expect, results are quite different. By looking at the maximal values, we can detect where are located the signals but both decompositions tell us that the waveform does not fit them properly.

As we highlighted with this example, this method requires an a priori knowledge of the waveform we are interested analyzing which can be quite difficult when dealing with more complex waveforms.

Compressive sensing (CS)

Compressive sensing [SMF10] has emerged in the work of Candès et al [CRT06, CT06], Donoho [Don06] and Baraniuk [Bar07] and is a sampling model that allows us to go beyond Shannon

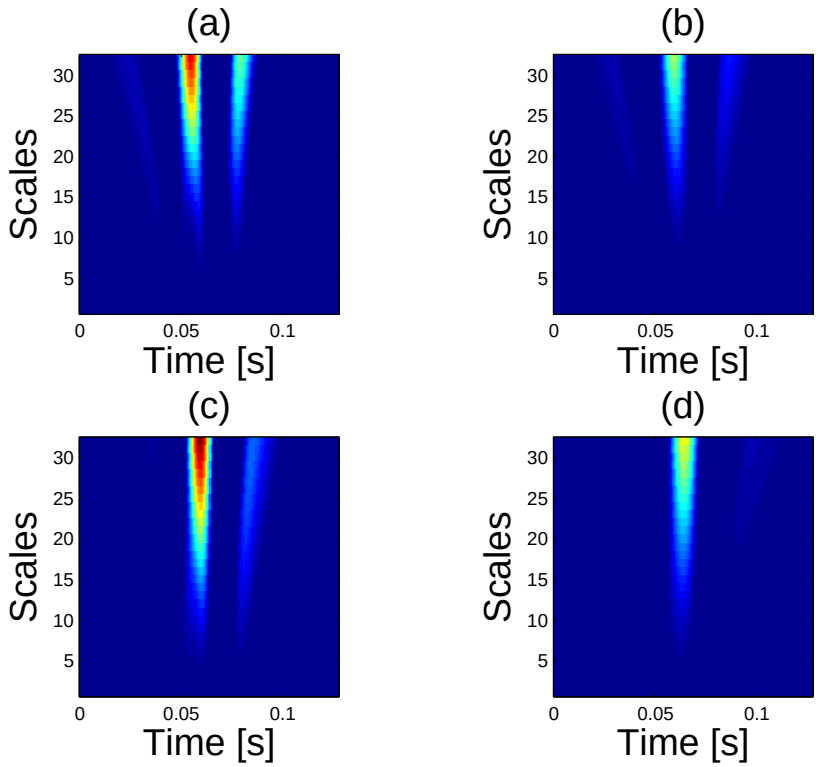

Figure 1.3: Wavelet decompositions by using the Symlet mother wavelet on the first row, and the Daubechies mother wavelet on the second row, for the two studied signals: $s_1(t)$ on the first column and $s_2(t)$ on the second column.

limit by exploiting the sparsity structure of the signal. The theory asserts that certain signals can be recovered from fewer measurements m than data samples N. It relies on two conditions:

- **sparsity**: the information contained in the signal can be smaller than its bandwidth and be easily represented in a dictionnary,
- **incoherence between the sensing modality and the dictionnary**: while the signal need to be sparse in the dictionnary, it also needs to be spread out in the domain where it was acquired. To do so, the sensing vectors need to be as dense as possible in the dictionnary.

If those two conditions are met, CS shows that it is possible to simultaneously sense and compress the signal without acquiring N samples.

Distributions

A particular domain of projective based representation approaches is the one of distributions. Starting from the projections of instantaneous correlation function $s(t-\tau/2)\,s^*(t+\tau/2)$ on

the $\left\{e^{j\omega_k t}\right\}_k$ basis, a broad class Cohen's class [Coh95] of distributions has been defined and used. One of these well-known distributions is the Wigner-Ville distribution. However, this distribution has to deal with cross-terms: the apparition of cross-terms when dealing with multi-components signals, and also inner interferences due to undesired nonlinearity effects of nonstationnarity. All those terms reduce considerably the interpretation of the distribution in the time-frequency plane. In order to reduce these effects, the concept of complex arguments has been introduced [Sta02]. It takes advantage of the complex frequency argument (in the Laplace domain) and a corresponding complex lag in the time domain to produce almost completely concentrated representations along the different phase derivative order of a signal. They are known as **Generalized Complex-time Distributions** (*GCD*). Though, the computation of the distribution involves the analytic extension of the signal in the complex domain that is performed by the analytic continuation and therefore, restricts the application to narrow bandwidth signals. Subsequently, in the next Chapter, we propose a method to extend it to signals having larger frequency variation.

1.3 Data-driven analysis techniques

This group of techniques does not assume any model of analyzing data. They are mainly focused on the study of sample organisation in time. Among possible approaches, we mention here the Empirical Mode Decomposition (EMD) and the phase diagram.

Empirical Mode Decomposition

The EMD, also known as the Hilbert-Huang transform [HS05], corresponds to a way of decomposing a signal into so-called intrinsic mode functions called IMF: each of them representing a simple oscillatory mode.

Empirical Mode Decomposition has proved itself efficient for analyzing the different modes included in a signal without determining set up parameters. However, this data-driven method presents a major drawback, known as mode mixing problem as the decomposition's result is not unique and can be changed from one realisation to another. Even if some elements of solution has been proposed over the time [HW08], we need to keep in mind that this empirical algorithm has not been proven yet and is still controversial.

Phase diagrams

Another famous data-driven technique is the signal analysis by phase diagrams also represented by recurrence plot analysis (RPA) which has been introduced by Eckmann et al. [EKR87] in 1987 in order to visualize recurrences of higher-dimensional phase space trajectories in nonlinear data time series. By recurrence, we refer to the return of a state of a system to a previously visited point.

RPA is based on three major steps: time-delay embedding (1980-1981) [Tak81, PCFS80], recurrence plots (1987) and recurrence quantification analysis (RQA)(1992-2002) [ZW92, MK02]. More details about the history of RPA can be found in [Mar08] and an international website gathers all the advances and communications of the community [RPA].

To begin with, the analyzed signal $s(n)$ defined for $n \in \{1, \ldots, N\}$ is first turned into a trajectory $\overrightarrow{v}[s, \tau, m]$ by forming vectors from groups of samples. The signal is vectorized through **the spatial-embedding process** set up by two parameters: m the embedding dimension and τ the time delay which can be seen as an integer decimation factor. Phase space vectors computed at instant n are defined as follows:

$$\overrightarrow{v_n}[s, \tau, m] = [s(n), s(n+\tau), \ldots, s(n+(m-1)\tau)] \tag{1.16}$$

Vector construction is illustrated by Figure 1.4. As an example, at instant n_0, we only consider $s(n)$ samples for $n \in [n_0, n_0 + (m-1)\tau]$ and then keep every τ samples.

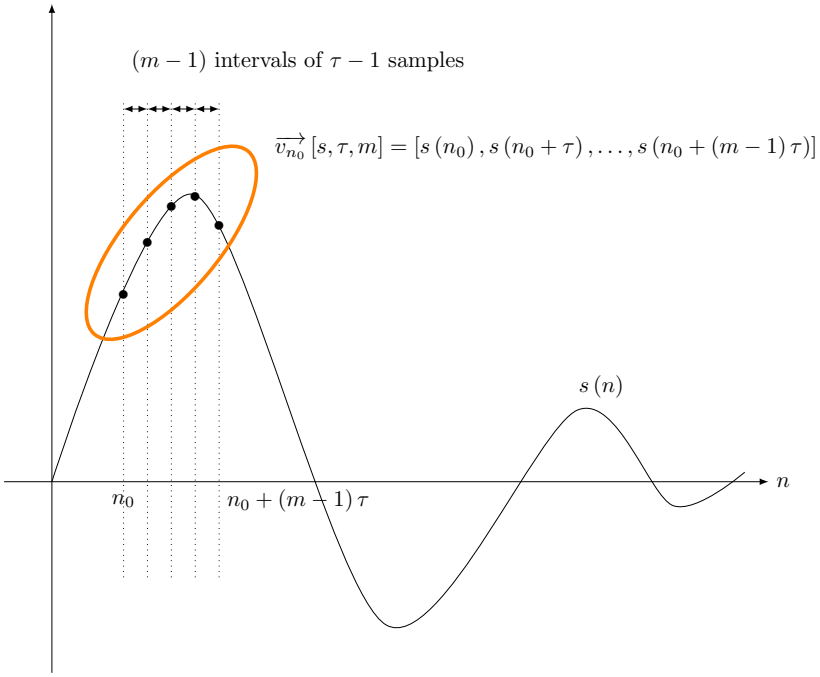

Figure 1.4: Creation of a phase space vector at instant n_0 using the parameters τ and m.

The vector construction is then repeated for each sample of the signal, which creates the phase space diagram. As an example, Figure 1.5 presents the creation of a phase diagram for $m = 3$ and $\tau = 2$ samples.

Classical RPA then computes the distances $\mathcal{D}$ between each phase space vectors that are recorded in a matrix D called distance matrix such as:

$$D_{i,j} = \mathcal{D}\{\overrightarrow{v_i}[s, \tau, m], \overrightarrow{v_j}[s, \tau, m]\} \tag{1.17}$$

Many distances $\mathcal{D}$ can be chosen sush as the classical euclidean metric or the Manhattan distance, etc... Therefore, Ioana et al.[IDS+14] developed several distances that permitted to highlight different properties of signals depending on the purpose of the analysis.

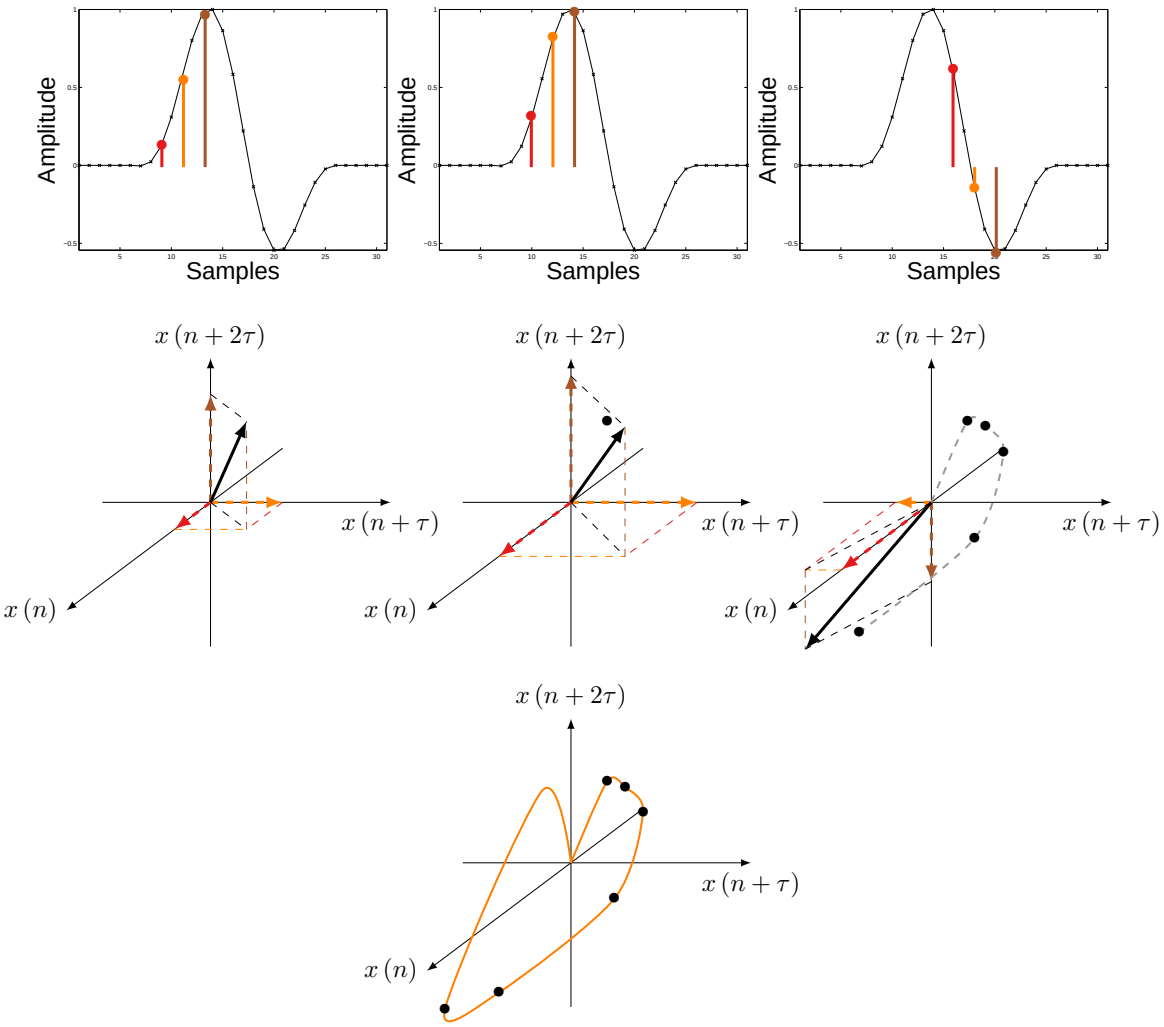

Figure 1.5: Creation of a phase diagram for a given signal, $m = 3$ and $\tau = 2$.

Then by thresholding the distance matrix, recurrences are enlightened in the recurrence matrix R also known as **recurrence plot (RP)**.

$$R_{i,j}^{\tau,m,\epsilon} = \Theta\left(\epsilon - D_{i,j}\right) \tag{1.18}$$

where Θ is the Heavyside function and ϵ is the recurrence threshold. A recurrence is enlightened if the distance between two vectors is inferior to the recurrence threshold. The Heavyside function then provides a value of 1. On the contrary, if the distance is superior to the threshold, then the recurrence matrix provides a value of 0.

The summary of recurrence plot analysis is presented in Figure 1.6.

Finally, the last step is the computation of recurrence quantifications on RP: this is what is called **Recurrence Quantification Analysis (RQA)**. Several types of measures exist in literature that either quantify black point density, diagonal lines, or vertical lines [MCTK07].

But one of the most famous measure is the recurrence rate RR that corresponds to the density of recurrence points in a RP:

$$RR = \frac{1}{N^2} \sum_{i,j=1}^{N} R_{i,j} \tag{1.19}$$

The idea of building trajectories from successive samples of a signal was supported by Taken's theorem, which states that a dynamical system attractor can be reconstructed from a series of observations of the state of the dynamical system, embedded in a dimension that is greater than twice the size of the attractor. However, the conditions of this theorem are not satisfied by real world signals that are not noise-free and do not have infinite resolution. Nevertheless, we must notice that many informations can be hidden inside the signals about the global dynamics of the system that produce them. The difficulty in revealing this information through time-delay embedding consists in choosing proper values for m and τ. Various techniques have been proposed in the literature [Sma05] to solve this problem, such as false nearest neighbours or successive embeddings for the embedding dimension, and autocorrelation or mutual information for the delay. However, **there is no universal best choice for parameters m and τ** as it highly depends on the application.

1.4 Summary

In this Chapter, we have presented a brief overview of the existing methods for transient analysis. All of them present advantages but also drawbacks that can eventually be improved. In the further chapters, we propose to focus on two classes of approaches: the linear projections and the data-driven analysis techniques. Next chapter is therefore dedicated to the study of signals having fast-varying time-frequency components and is adressed with the class of projection-based approaches through GCD and also compressive sensing.

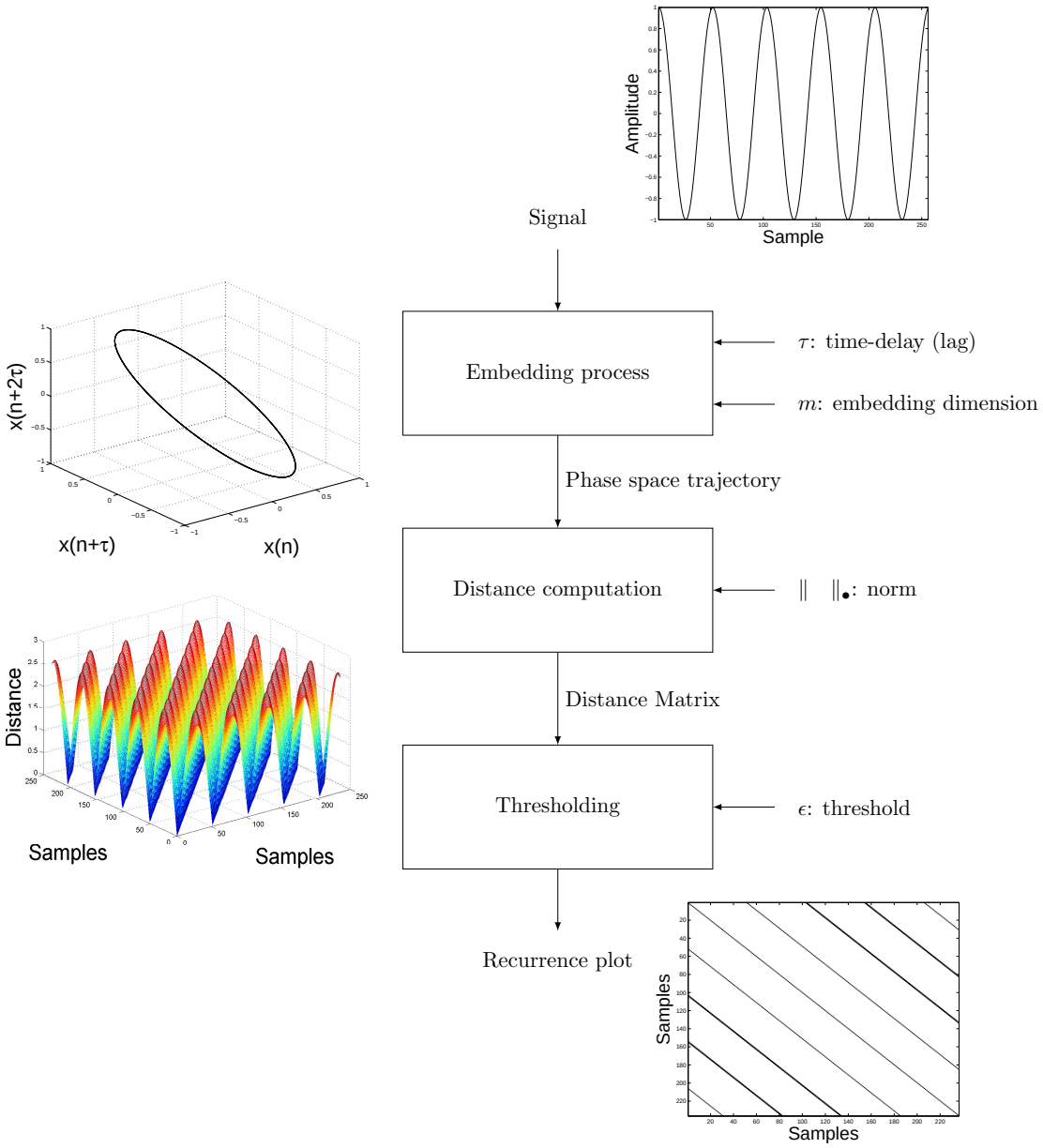

Figure 1.6: Recurrence plot analysis is computed through 3 steps: the time-delay embedding process, the distance matrix, and finally the recurrence matrix.

Chapter 2

Representation of signals having fast-varying time-frequency components

Contents

In this Chapter, we propose to focus on the representation of signals having fast-varying time-frequency components using projection-based approaches. In a first part, we focus on the generalized complex-time distribution and propose a method to extend its application to signals having larger frequency variations as it is limited to narrow bandwidth signals for now. In a second part, we propose to study the recovery of nonlinear modulation phase signals when samples are missing from the observation. It takes advantages of time-axis transformations and compressive sensing.

2.1 Generalized Complex-time Distributions

Time-frequency representations are very helpful to characterize the richness of the information contained in nonstationary signals. It can help to monitor the appearance of short transient electrical signals and the beat of an heart, for example. The subject has been largely covered with the Cohen's class representation [Coh95], wavelet transform, etc... Generally, they characterize the frequency content of a signal over the time, with some specific limitations like inner interferences, cross-terms, artefacts, trade-off between time and frequency resolutions, etc...

Recently, complex time distribution concept has been introduced in [Sta02] as a way to produce high concentrated distributions along the different phase derivatives of a signal. The main idea is to use the high order moments of the signals calculated for complex-time lags. It has also been shown that it was possible to deal with multi-component signals [GIS+08]. This technique has however some drawbacks as it involves the calculation of signal samples at complex coordinates through analytic continuation [SS96]. This estimation leads to poor representations as it can produce a divergence. A numerical example proves the efficiency of the modified analytical continuation technique extending also the capacity of the complex time distribution to deal with time-frequency structures with larger bandwidth.

In this section, we propose a method to overcome the limitations introduced by the analytical continuation in the case of signals with a spread time-frequency variation. This method is based on the compression of the signal spectrum to a bandwidth that ensures the efficiency of the analytical continuation technique. Then, the application of generalized complex time distribution will allow an accurate estimation of the different phase derivative law. The spectrum expanding brings this estimation to the correct time-frequency location.

2.1.1 General presentation of complex time distributions

The complex time distribution concept has been introduced in [SS96] as a way to reduce inner terms in Wigner-Ville distributions when dealing with nonlinear time-frequency structures. It takes advantages of complex-time signal arguments that enable to provide distributions that are concentrated along the *K-th* derivative of the phase for regular signals [Sta02, Cor06, CSI+07, GIS+08, Got10].

Let consider the signal $s(t)$ defined as:

$$s(t) = Ae^{j\Phi(t)} \tag{2.1}$$

with A the signal amplitude that is constant or can slowly vary and $\Phi(t)$ its phase.

We consider the phase as a real analytic function. Then, by using the Taylor's series expansion of the phase, we can write:

$$\Phi(t+\tau) = \sum_k \Phi^{(k)}(t)\frac{\tau^k}{k!} \tag{2.2}$$

This equation brings forward the different phase derivatives of the signal. Phase integration in the complex plane using the theory of Cauchy's integral theorem [Rud87] then allows to focus on a particular phase derivative:

$$\Phi^{(K)}(t) = \frac{K!}{2j\pi} \oint_{\gamma} \frac{\Phi(z)}{(z-t)^{K+1}} dz \tag{2.3}$$

where γ describes the contour integral of the equation. This equation shows the interest of the complex time concept as it enables to compute the K^{th} order derivate of Φ at instant n as the complex integral over the integration path γ.

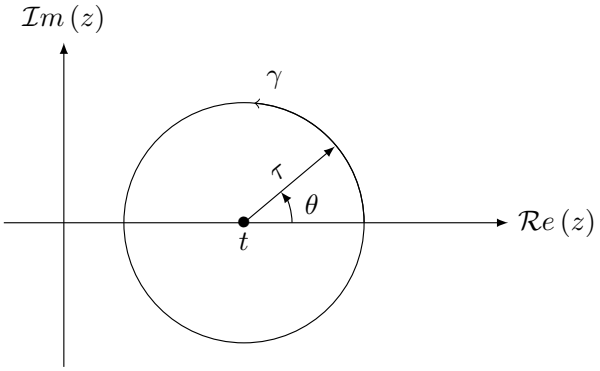

Figure 2.1: Integral contour γ used to compute the Cauchy integral in complex plane.

We here consider γ the integral contour as the circle of center t and radius τ taken counter-clockwise (Figure 2.1). Then by considering $z = t + \tau e^{j\theta}$, Equation 2.3 becomes:

$$\Phi^{(K)}(t) = \frac{K!}{2\pi\tau^K} \int_0^{2\pi} \Phi\left(t + \tau e^{j\theta}\right) e^{-jK\theta} d\theta \tag{2.4}$$

We can now consider the discrete form of the equation for the N roots of unity defined for $\theta = 2\pi p/N$ and $p = 0, \ldots, N-1$ which are represented in Figure 2.2. Equation 2.4 becomes:

$$\Phi^{(K)}(t) = \frac{K!}{2\pi\tau^K} \sum_{p=0}^{N-1} \Phi\left(t + \tau e^{j\frac{2\pi p}{N}}\right) e^{-j\frac{2\pi pK}{N}} + \epsilon \tag{2.5}$$

where ϵ stands for the discretisation error.

Let $\omega_{N,p} = e^{j2\pi p/N}$ be the roots of unity, we also know that:

$$\sum_{p=0}^{N-1} \omega_{N,p}^{k} = \begin{cases} N & \text{if } k = 0 \ (mod N) \\ 0 & \text{otherwise} \end{cases} \tag{2.6}$$

By using this property, the Taylor series expansion (Equation 2.2) and the variable change $\tau \rightarrow \sqrt[K]{\tau \frac{K!}{N}}$, the previous expression then becomes:

$$\sum_{p=0}^{N-1} \Phi\left(t + \omega_{N,p} \sqrt[K]{\tau \frac{K!}{N}}\right) \omega_{N,p}^{N-K} = \Phi^{(K)}(t)\tau + Q(t,\tau) \tag{2.7}$$

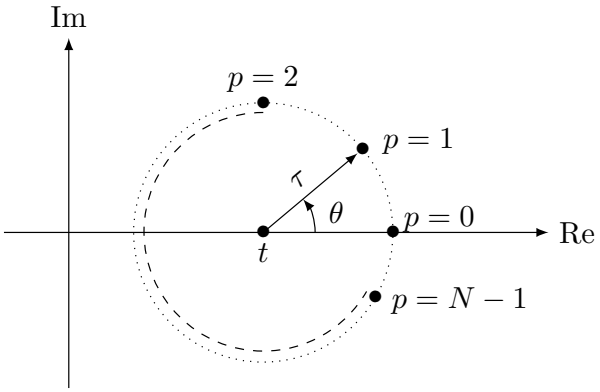

Figure 2.2: Representation of the roots of unity

where $Q(t,\tau)$ corresponds to the spread function which only contains the derivatives of order $Nk+K$, defined as:

$$Q(t,\tau) = N\sum_{p=1}^{\infty}\Phi^{(Np+K)}(t)\frac{\tau^{\frac{Np}{K}+1}}{(Np+K)!}\left(\frac{K!}{N}\right)^{\frac{Np}{K}+1} \tag{2.8}$$

Therefore, we define the generalized complex-time moment (GCM):

$$GCM_N^K[s](t,\tau) = \prod_{p=0}^{N-1} s^{\omega_{N,p}^{N-K}}\left(t+\omega_{N,p}\sqrt[K]{\frac{K!}{N}}\tau\right) \tag{2.9}$$

$$= e^{j\Phi(K)(t)\tau+jQ(t,\tau)} \tag{2.10}$$

The Fourier transform of the GCM produces the generalized complex time distribution (GCD):

$$GCD_N^K[s](t,\omega) = TF_\tau\left[GCM_N^K[s](t,\tau)\right] \tag{2.11}$$

$$= \delta\left(\omega-\Phi^{(K)}(t)\right) \underset{\omega}{*} TF_\tau[Ae^{jQ(t,\tau)}] \tag{2.12}$$

As stated by this definition, the *K-th* order distribution of the signal, obtained for N complex-lags, highly concentrates the energy around the *K-th* order derivate of the phase law. This concentration is optimal if the Φ 's derivates of orders greater than $N+K$ are 0. Observing Equation 2.8, it can be noticed that the first term appearing in the spreading function is the phase derivative of order $K+N$, the second one is of order $K+2N$,... Thus the parameter N highly affects the spreading function. We can conclude that a high value of N reduces interferences since Q is reduced and distribution concentration will be less sensitive to higher order phase derivatives. This theory has been well developed in [Cor06, CSI+07, Got10].

However, the computation of GCM implies the calculation of signal samples at complex coordinates (complex lags), this is called the analytic continuation.

2.1.2 Limitation introduced by the analytical continuation

The analytical continuation of a signal $s(t)$ is performed as defined in [SS96].

$$s(t+jm) = \int_{-\infty}^{\infty} S(f) e^{-2\pi mf} e^{j2\pi ft} df \tag{2.13}$$

where $S(f)$ is the Fourier transform of signal $s(t)$.

The calculation involves the multiplication of the spectrum by the exponential $e^{-2\pi mf}$ which has different effects on the spectrum. Those are shown in Figure 2.3 for a test signal $s(t) = e^{j6\cos(2\pi t)}$ and different values of m. When the frequencies are positive, they are strongly attenuated due to the decreasing exponential. In the meantime, negative frequencies are strongly amplified, which can lead to a divergence in certain cases (Figure 2.3(c)). If we consider a second test signal $s(t) = e^{j6\cos(2\pi t/2)}$ that has a bandwidth twice smaller (Figure 2.4), we can notice that the spectrum is less affected by the analytical continuation. Generally speaking, the use of Fourier base constitutes a problem when we deal with wide-band signals as their half higher band are strongly impacted by the prolongation.

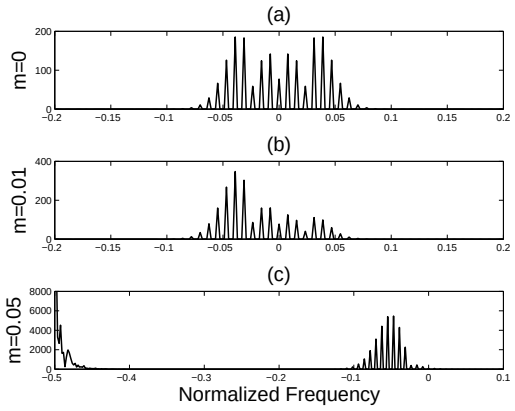

Figure 2.3: This Figure represents the spectrum $S(f)$ of the signal $s(t) = e^{j6\cos(2\pi t)}$ multiplied by an exponential $e^{-2\pi mf}$ for different value of m: (a) $m = 0$, (b) $m = 0.01$ and (c) $m = 0.05$.

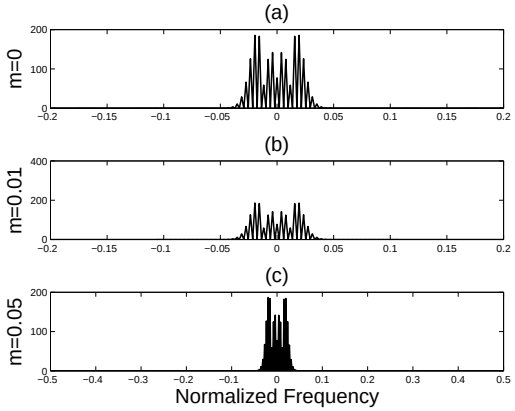

Figure 2.4: This Figure represents the spectrum $S(f)$ of the signal $s(t) = e^{j6\cos(2\pi t/2)}$ multiplied by an exponential $e^{-2\pi mf}$ for different value of m: (a) $m = 0$, (b) $m = 0.01$ and (c) $m = 0.05$.

Therefore, it is really important to note that **the analytic continuation is strongly affected by the choice of m and the bandwidth of the studied signal**. A strong value of m induces a very fast decreasing exponential that will completely affect the bandwidth and in the meantime, a large bandwidth will be more sensitive to the multiplication with a decreasing exponential. As a consequence, the best scenario would be to study small bandwidth signals using really small values of m to limit the negative effects of the analytic continuation. This restricts considerably the capabilities of wide-band signals (such as transients) analysis and our contribution is aimed to reduce this limitation.

In order to illustrate the limitation in terms of analytical continuation, let consider two

signals defined as:

$$s_1(t) = e^{j\left(6\cos(\pi t)+\frac{4}{3}\cos(2\pi t)+\frac{4}{3}\cos(4\pi t)\right)} \tag{2.14}$$

$$s_2(t) = e^{j(18\cos(\pi t)+4\cos(5\pi t)+4\cos(15\pi t))} \tag{2.15}$$

Figure 2.5 shows the theoretical instantaneous frequency laws for s_1 and s_2, as well as the results of the generalized complex time distribution using $N = 6$ and $K = 1$. We notice that if the GCD gives good results for s_1 we can no longer estimate the first phase derivative for s_2. This is due to the computation of the analytical continuation and the large bandwidth of s_2 which is six times larger than s_1's.

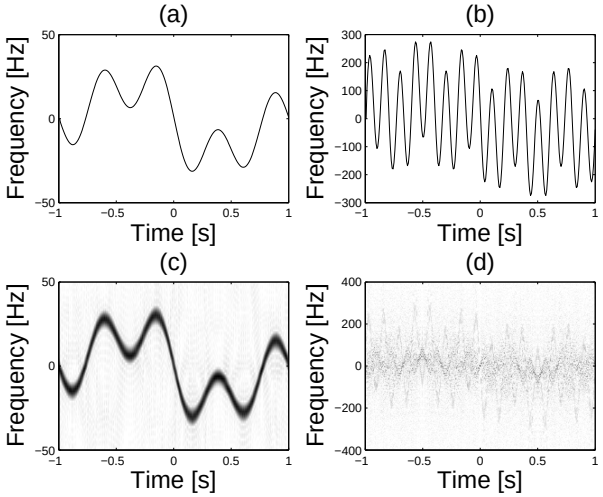

Figure 2.5: This figure represents the theoretical instantenous frequency laws for (a) $s_1(t)$ and (b) $s_2(t)$ and the classical GCD associated for (c) $s_1(t)$ and (d) $s_2(t)$.

2.1.3 Time-scaled complex time distributions

In this section, we propose a method for the analytical continuation in the case of wideband signals. It consists in modifying the frequency support of the analyzed signal s, in order to reduce the attenuation of the analytical continuation term.

Let consider a signal $B(t)$ defined as:

$$B(t) = s\left(\alpha t\right) \tag{2.16}$$

with $\alpha > 1$ a dilation coefficient and $s\left(t\right)$ a signal defined as Equation 2.1. The dilation of the temporal signal leads in the frequency domain to a contraction of the bandwidth. This is actually the concept of the time-scale representation that we use at this point [Mal99]. Considering the complex-time moment of $B\left(t\right)$, we have:

$$GCM_N^K[B](t,\tau) = \prod_{p=0}^{N-1} s^{\omega_{N,p}^{N-K}}\left(\alpha t + \alpha\omega_{N,p}\sqrt[K]{\frac{K!}{N}\tau}\right) \tag{2.17}$$

We can clearly notice that the main impact directly concerns the analytical continuation. We then focus on its calculation. According to the Taylor serie expansion (Equation 2.2), we have:

$$s\left(\alpha t + j\alpha m\right) = \sum_{k=0}^{\infty} \frac{s^{(k)}\left(\alpha t\right)}{k!} \left(j\alpha m\right)^k \tag{2.18}$$

Knowing the following Fourier 's formula:

$$s^{(k)}(t) = \int_{-\infty}^{\infty} \left(j2\pi f\right)^k S(f) e^{j2\pi ft} df \tag{2.19}$$

we then obtain:

$$s^{(k)}\left(\alpha t\right) = \int_{-\infty}^{\infty} \left(j2\pi f\right)^k S(f) e^{j2\pi\alpha ft} df \tag{2.20}$$

Considering the variable change $f \rightarrow f/\alpha$, we obtain:

$$s^{(k)}\left(\alpha t\right) = |a|^k \int_{-\infty}^{\infty} \left(j2\pi \frac{f}{\alpha}\right)^k S\left(\frac{f}{\alpha}\right) e^{j2\pi ft} \frac{df}{\alpha} \tag{2.21}$$

Taking into account Equations 2.18 and 2.21, we then deduce:

$$s\left(\alpha t + j\alpha m\right) = \frac{1}{\alpha} \int_{-\infty}^{\infty} S\left(\frac{f}{\alpha}\right) \sum_{k=0}^{\infty} \frac{\left(-2\pi mf\right)^k}{k!} e^{j2\pi ft} df \tag{2.22}$$

Finally, we obtain the contracted analytical continuation:

$$s\left(\alpha t + j\alpha m\right) = \frac{1}{\alpha} \int_{-\infty}^{\infty} S\left(\frac{f}{\alpha}\right) e^{-2\pi mf} e^{j2\pi ft} df \tag{2.23}$$

We can see that this leads to a contraction of the spectrum, and as a matter of fact, its bandwidth will be less affected by the attenuation term $e^{-2\pi mf}$. We defined $s_\alpha\left(t\right)$ as the signal $s\left(t\right)$ whose frequency support is contracted by the dilation coefficient α, ie $S_\alpha(f) = S\left(\frac{f}{\alpha}\right)$. Thus, we obtain:

$$s\left(\alpha t + j\alpha m\right) = \frac{1}{\alpha} s_\alpha(t + jm) \tag{2.24}$$

As we can notice, the two signals are still related. The GCM then becomes:

$$\begin{aligned} GCM_N^K[B]\left(t,\tau\right) &= \prod_{p=0}^{N-1} \left(\frac{1}{\alpha} s_\alpha\left(t + \omega_{N,p} \sqrt[K]{\frac{K!}{N}\tau}\right)\right)^{\omega_{N,p}^{N-K}} \\ &= \left(\frac{1}{\alpha}\right)^{\sum_{p=0}^{N-1} \omega_{N,p}^{N-K}} GCM_N^K[s_\alpha](t,\tau) \end{aligned} \tag{2.25}$$

Two scenarios then need to be studied:

- When $N = K$ (modulo N), ie when the number of roots of unity is equal to the phase derivative order, then we have:

$$GCM_N^K[B](t,\tau) = \frac{1}{\alpha^N} GCM_N^K[s_\alpha](t,\tau) \tag{2.26}$$

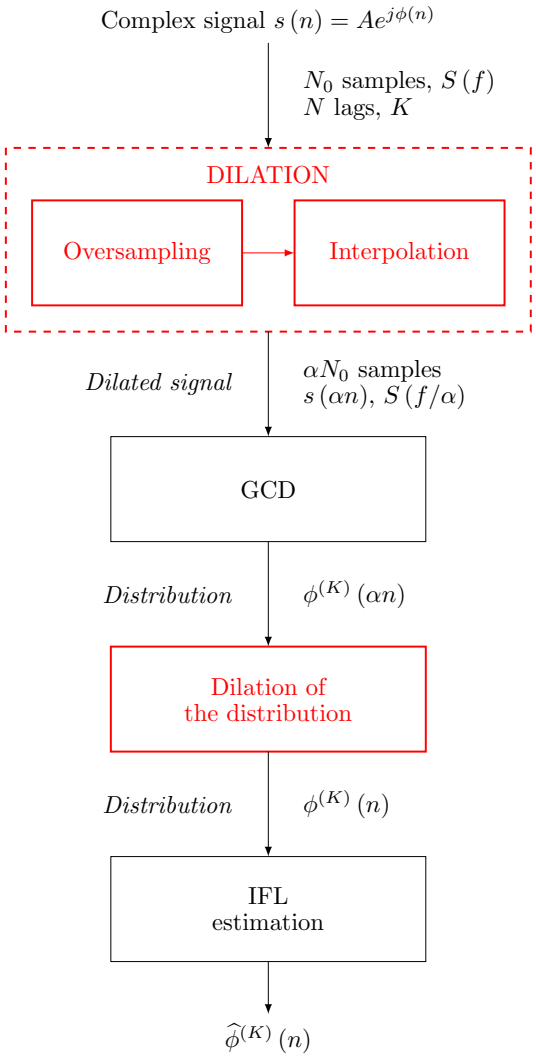

Figure 2.6: This Figure represents the procedure used to perform the time-scaled GCD.

- Otherwise:

$$GCM_N^K[B](t,\tau) = GCM_N^K[s_\alpha](t,\tau) \tag{2.27}$$

In both cases, we can conclude that the GCD provides the same results with a different intensity when the factor $\frac{1}{\alpha^N}$ appears. Equation 2.27 shows that it is possible to extract the *K-th* phase derivative order distribution of a signal by using its dilated version. We then need to expand the distribution to obtain the real distribution for signal s. This is performed by using Equation 2.28, which corresponds to a two dimensionnal warping [PSHBB98]:

$$GCD_N^K[s](t,\omega) = \alpha GCD_N^K[B](t,\omega) \tag{2.28}$$

The procedure is detailled in Figure 2.6. However, a question still remains: how do we choose the dilatation coefficient α? For now, this choice is not straightforward due to its high

dependance on the analyzed signal. A first approach would consist in performing the time-scaled complex time distribution for multiple value of α and then to choose the distribution that offers the best concentration in term of **phase derivative law** (PDL) estimation.

2.1.4 PDL estimation

The traditional procedure used to extract the PDL estimate $PDL\,(t)$ from the GCD distribution is actually quite simple. At each instant t, the method localizes the maximum of the distribution as follows:

$$PDL\,(t) = \underset{\omega}{argmax}\left[GCD_N^K[s]\,(t,\omega)\right] \tag{2.29}$$

However, due to the presence of artefacts on the distribution, this method sometimes fails to provide a good estimation at every instant t. In order to overcome this limitation, we have developed a technique that does not select automatically the maximum of the distribution. The procedure is described below and illustrated in Figure 2.7.

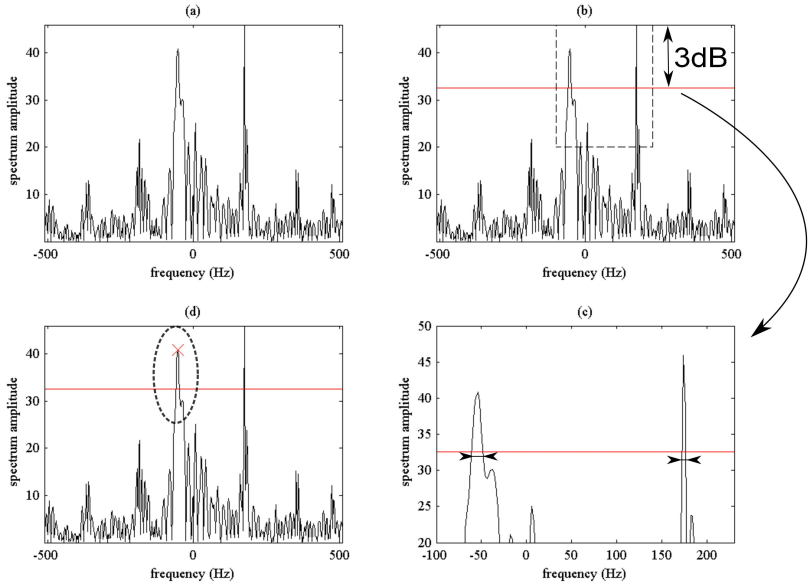

Figure 2.7: (a) represents the spectrum at a given instant of the distribution. Classical PDL estimation would choose the higher peak as the PDL estimate. However by considering all the peaks whose values are greater than the attenuation at 3dB G_{3dB}(b), we have two potential results. By observing both bandwidth of the peaks (c), we select the greater one as the new PDL estimation (d).

At every instant t, the spectrum of the distribution is observed and we calculate the value G_{3dB} corresponding to a $3dB$ attenuation relative to the highest value of the spectrum. All the peaks higher than G_{3dB} and their bandwidth (related to G_{3dB}) are then considered as possible PDL estimates. We then compare the bandwidths and select the most important one.

Why do we have to choose the biggest one? The GCD provides a distribution that is high-concentrated around the Kth phase derivative which implies that spectrums must have a minimum bandwidth at each instant t. If the selected peak's bandwidth is too narrow, then it is possible that it only represents an artefact of calculation.

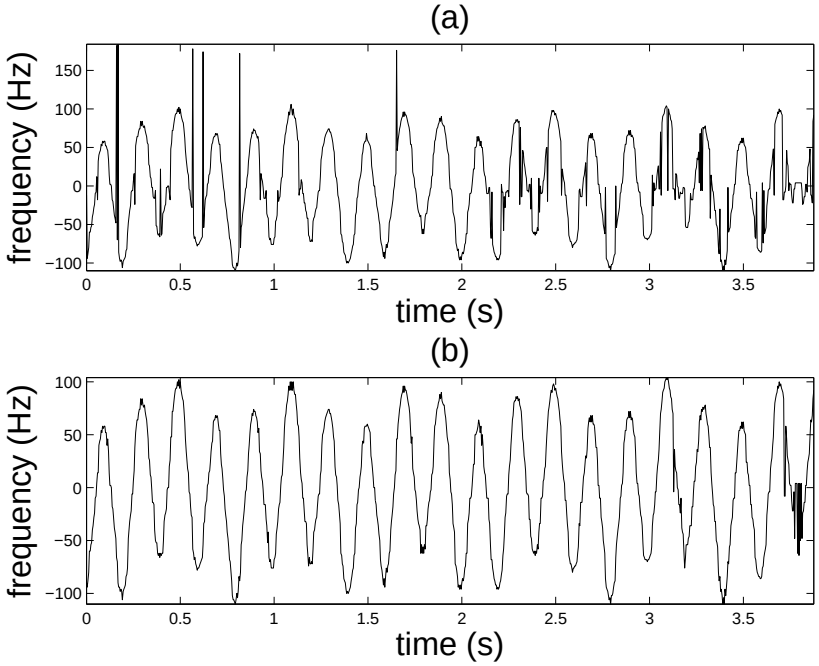

Figure 2.8: (a) represents the IFL estimation obtained with classical method. We can see a lot of artifacts which disappear with the new method (b).

Figure 2.8 shows the improvements obtained with the new procedure compared to those obtained with the traditional technique. It is quite obvious that the number of false detections has been reduced.

Next Section is dedicated to the study of an example.

2.1.5 Numerical example

2.1.5.1 Presentation of the example

In order to evaluate the performances of the proposed approach, we choose to work with the following signal and to represent its first phase derivative (Figure 2.9 (a)):

$$s(t) = e^{j(18\cos(\pi t)+4\cos(10\pi t)+4\cos(15\pi t))} \tag{2.30}$$

As we can see in Figure 2.9(c), the classical GCD fails to represent the first phase derivative of the signal due to its large bandwidth and the analytic continuation.

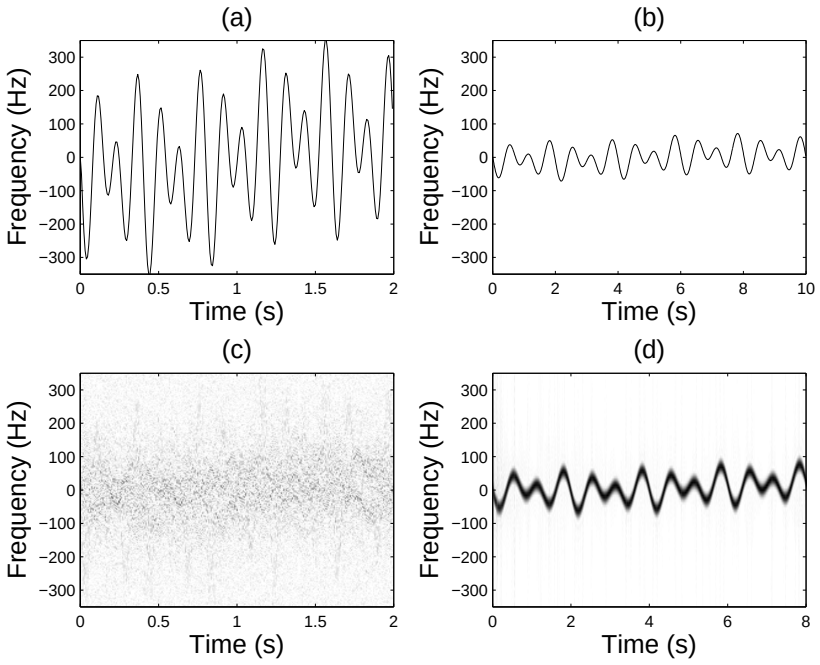

Figure 2.9: (a) and (b) represent the theoretical instantaneous frequency laws of $s(t)$ and its dilated version. (c) and (d) are their respective GCD.

In order to test our method, we choose to dilate $s(t)$ with $\alpha = 5$ and to apply the GCD algorithm using 6 complex lags (i.e. $N = 6$ and $K = 1$). We then study the new signal $s_\alpha(t) = s(\alpha t)$. The dilatation leads to a contraction of the bandwidth with a factor equal to α which reduces considerably the bandwidth. Figures 2.9 (b) and (d) respectively show the theoretical instantaneous frequency law and the result of the GCD algorithm applied on s_α. We can notice that the GCD provides really good results.

The frequency law obtained for $s_\alpha(t)$ is as stated by Equation 2.27 a contraction of the one of $s(t)$, to obtain the last one, it is then necessary to dilate the frequency law obtained with the dilation coefficient α. Figure 2.10 shows the comparison between the theoretical intantaneous frequency law of $s(t)$ and the dilated frequency law of $s_\alpha(t)$. We can notice that they match almost perfectly. Figure 2.11 shows the DGTC of $s_\alpha(t)$ after dilation.

We have seen that it was possible to overcome one of the limitation of the analytic continuation for the GCD method using a dilation coefficient.

2.1.5.2 Comparison with other techniques

As we already know, the first phase derivative of a signal represents its instantaneous frequency, a subject that has already been well covered by the literature. Many algorithms have been developed such as: the spectrogram and Wigner-Ville representations [Coh95].

In this section, we propose to compare the performance of two methods: the spectrogram

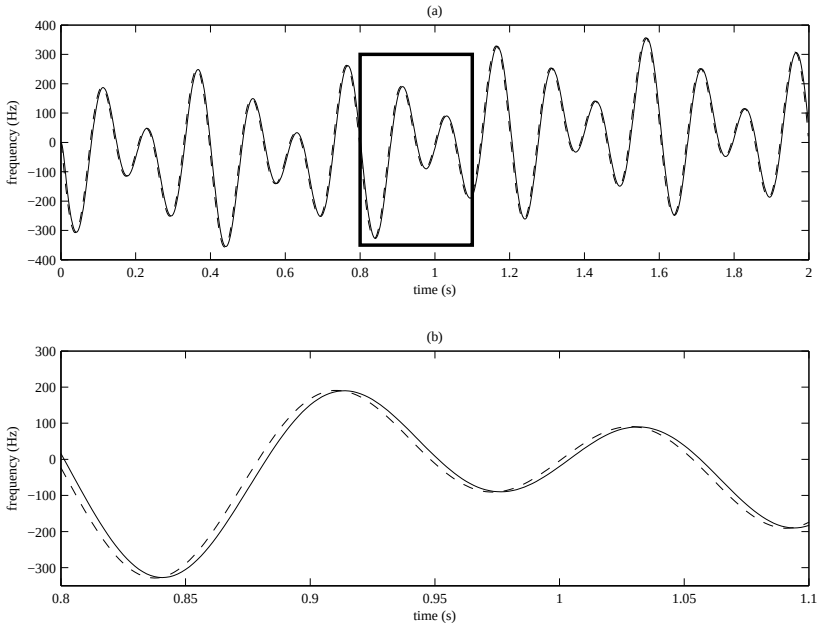

Figure 2.10: (a) The continuous curve represents the theoretical instantaneous frequency law of $s(t)$ meanwhile the dash line represents the instantaneous frequency law of $s_\alpha(t)$ obtained with the GCD algorithm after dilatation. (b) is a zoom of (a)

and classical GCD with the study of an example. Because time-scaled GCD is similar to classical GCD in the sense that we perform a GCD on a modified signal, we do not compare this technique. We consider the signal $s(t)$ defined in Equation 2.30. The spectrogram is performed using a 32-samples Hanning window sliding every sample and the classical GCD uses 6 complex lags.

In order to compare the results given by the different techniques, we calculate the Mean Square Error (MSE) for each representations. Given $PDL(n)$ the theoretical PDL, $\widehat{PDL}(n)$ the estimated IFL, and N the number of samples, the MSE is calculated as follows:

$$MSE = \frac{1}{N}\sum_{n=1}^{N}\sqrt{\left\|PDL(n) - \widehat{PDL}(n)\right\|^2} \tag{2.31}$$

This measure has been performed for the two techniques and actually provides the precision of the estimations. Results are shown in Table 2.1.

At every instant t, the $-3dB$ bandwidths of the distributions are evaluated. Figure 2.12 presents the histograms of these values. It can be noticed that the concentrations are almost constant varying around 16-18 Hz. While the concentration obtained with the GCD algorithm is quite dispersed compared to the one obtained with the spectrogram, the mean value of the distribution is smaller than the spectrogram's and varies around 12 Hz. This particularity enables the GCD to have a smaller MSE which guarantees a smaller error estimation. As a way of conclusion, we can say that the GCD offers a better estimation in the sense of the MSE.

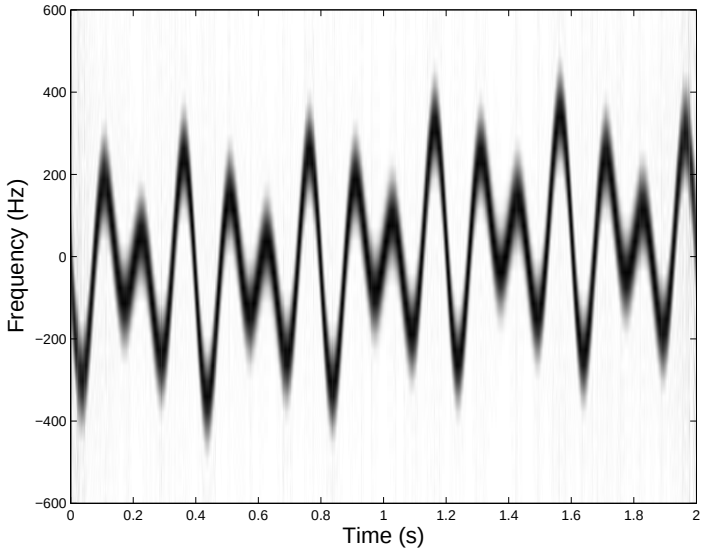

Figure 2.11: (a) This Figure represents the GCD of $s_\alpha(t)$ after dilation. It also represents $s(t)$'s GCD without artefacts

Techniques	Classical GCD	Spectrogram
MSE	0.4902 Hz	1.2694 Hz

Table 2.1: Performances achieved by classical GCD and the spectrogram

2.1.6 Summary

This section proposed a new analytical continuation technique that allows the generalized complex time distribution to deal with time-frequency structures having larger frequency variation. This technique is based on the compression of the signal's bandwidth and, then, the application of the generalized complex distribution. This transformation allows accurate estimation of the IFL. This works has been published at the EUSIPCO conference in 2013 and a journal paper is also under review:

C. Bernard and C. Ioana. Generalized complex time distribution using modified analytical continuation. In *21st European Signal Processing Conference EUSIPCO-2013*, September 2013.

C. Bernard, A. Digulescu and C. Ioana. Generalized complex time distribution using time-scale concept and modified analytical continuation. In *IEEE Transactions on Signal Processing*, under review.

As we have seen, the choice of the integration path is of great importance for a successful analysis, and this is why future works should focus on proposing an adaptive approach for the selection of the optimal scale parameter with respect of the bandwidth variation of the analyzed signal. Data-driven approaches (presented in Chapter 1) seem to offer a natural solution to this matter and this is why we orient the work toward the analysis of signals in

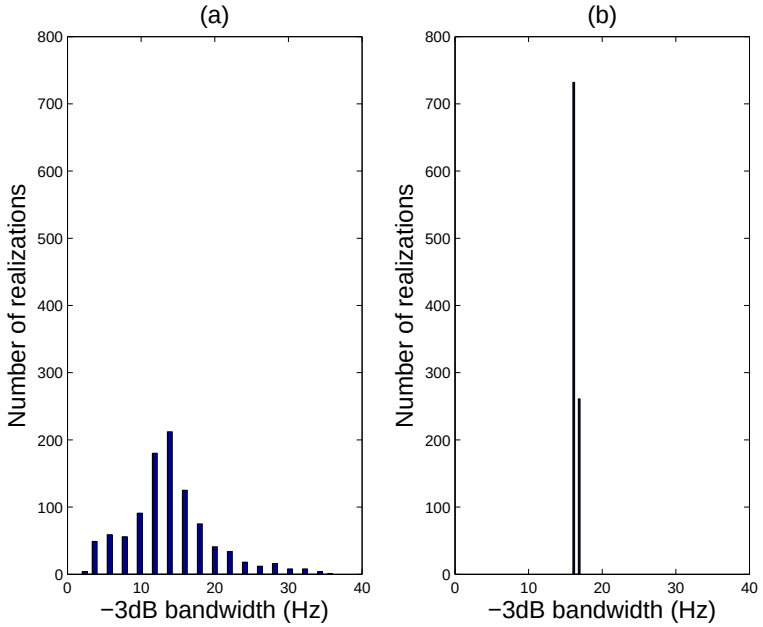

Figure 2.12: At every instant t of the GCD and spectrogram distributions, the $-3dB$ bandwidth is evaluated. This Figure represents the histograms of the $-3dB$ bandwidth values obtained for the GCD (a) and the spectrogram (b). We can observe that the spreading function of the GCD is more dispersed than the spectrogram's, but that the mean value is also smaller which guarantees a smaller error estimation.

phase diagram domain.

2.2 Warping-based analysis of transients with non-linear time-frequency components

2.2.1 Introduction

This section focuses on the recovery of signals having nonstationary time-frequency content defined as follows:

$$s(t) = \sum_{i=1}^{N} s_i(t) = \sum_{i=1}^{N} A_i e^{j\psi_i(t)} \tag{2.32}$$

where N is the number of components, A_i their amplitudes and $\psi_i(t)$ their instantaneous frequency laws that are nonlinear. The study focuses on two particular class of nonlinear modulation phase signals (NMPS):

- the logarithm phase law [PHBB93]

$$\psi_i(t) = 2\pi f_{0i} t + c_i \ln t;\ t \in [t_{0i}, t_{0i} + D_i] \tag{2.33}$$

with f_{0i} the central frequency of the modulation, c_i the logarithm modulation rate, t_{0i} the time instant when the modulation happens and D_i its duration.

- the monomial phase law [HPSBB99]

$$\psi_i(t) = 2\pi f_{0i} t + c_i t^k;\ t \in [t_{0i}, t_{0i} + D_i] \tag{2.34}$$

with f_{0i} the central frequency of the modulation, c_i the modulation rate, t_{0i} the time instant when the modulation happens, D_i its duration and k the monomial modulation order.

Such signals are of great interest as they are usually met in real world applications: they are commonly used by animals to communicate in nature due to their robustness to Doppler effect [IQS06] and are encountered in many real-life application areas such as radar and sonar. As the signals are recorded in the real world, they are often disturbed by different stationary and nonstationary interferences that could lead to misinterpretation. We introduce in this Chapter a method to extract components from highly disturbed observations. The main difficulty is that the desired and nondesired parts of signal may overlap in both time and frequency. This is why tracking methods usually do not provide good results.

It is well known that compressive sensing methods allow the reconstruction of signals having sparse basis representations even when dealing with an incomplete set of samples [Bar07, CRT06, Don06, FB10, JAS13]. This is the property that will be used in this chapter. However, as nonlinear modulation phase signals cannot be considered as sparse in the classical Fourier domain, the signals need to be expressed into another basis. This process is achieved by the class of unitary transformations developed by Baraniuk et al. at the beginning of the 90's [BJ93a, BJ93b, BJ95] and permits to turn nonlinear signals into sparse signals using the appropriate basis.

As the warped signal will be still corrupted by interferences, it should be filtered out from the noise. To do so, the L-statistics are used to identify and select time-frequency regions of the spectrogram that should be removed from consideration [SOSA13, SSA14]. A CS recontruction algorithm is then applied to denoise the spectrogram in order to reconstruct the signal of interest. Similar work has been conducted on linear frequency modulated signals (LFM) by Orovic et al. [OSS14].

To summarize, this chapter proposes a method to select and extract nonlinear modulation phase signals disturbed by nonstationary and other coherent signals. For that purpose, a time axis transformation (warping transform) is first performed in order to turn nonlinear phase signals into sparse sinusoid components. Then, the time-frequency regions corresponding to nonstationary and non sparse signals are identified and removed from consideration using the L-statistics approach. A CS reconstruction method is then applied on the set of remaining time-frequency (TF) points allowing a perfect recovery of sparse signal. The last operation is to perform a second time axis transformation in order to return to the original time domain.

We first introduce time axis transformation and a process that enables to stationnarize any non-linear component. Then compressive sensing is presented and finally we provide a

numerical example.

2.2.2 Time axis transformation

2.2.2.1 General formulation of time axis transformation

Generally, a warping operation enables to express a given signal $s(t)$ into another time domain (the warped domain) that simplifies the processing of the data.

Let consider a signal $s(t) \in \mathcal{L}(\mathbb{R})$ and $\mathcal{W}$ the warping operator defined as follows:

$$\{\mathcal{W}, \quad w(t) \in \mathcal{C}^1, \quad w'(t) > 0 : s(t) \rightarrow \mathcal{W}s(t)\} \tag{2.35}$$

where $\mathcal{C}^1$ corresponds to the class of differentiable functions. The modifications created on the studied signal are expressed through this formulation:

$$\mathcal{W}s(t) = \left|\frac{dw(t)}{dt}\right|^{1/2} s(w(t)) \tag{2.36}$$

where $w(t)$ is a smooth one-to-one function called the warping function. The first term $\left|\frac{dw(t)}{dt}\right|^{1/2}$ corresponds to the envelop of the warped signal that enables to conserve the energy of the original signal. It is also possible to define a non-unitary version of the warping operator if we do not want to deal with the envelop term. It is defined as follows:

$$\mathcal{W}s(t) = s(w(t)) \tag{2.37}$$

In most cases, warping functions are chosen in order to stationnarize the studied signals. Most popular warping operators used in the literature are the functions $w(x) = \exp^x$ [PS95] and $w(x) = |x|^{1/k} sgn(x)$ that have shown themselves really usefull for respectively analyzing logarithm and monomial phase signals (Equations C.22 and C.23). They turn the signals into stationary pure sinusoids.

If the warping function is analytical and bijective, then it is possible to unwarp the warped signal and come back in the original basis. However, they are most of the time not inversive as signals often met in real world applications are usually nonstationary and having time-frequency contents that cannot be described by analytical functions. Jarrot et al. [JIQ06] proposed a technique that extends the class of warping operators to discrete-time sequences and respects invertibility conditions.

2.2.2.2 Discrete formulation

The proposed concept starts from the straighforward definition for the sampled discrete-time warping operator:

$$\begin{aligned} (\mathcal{W}s[n])[m] &= s_w[m] \\ &= s\left(w_d\left(\tfrac{m}{M-1}\right)(N-1)T\right) \end{aligned} \tag{2.38}$$

where $w_d(u)$ is the normalized function of $w(t)$ defined by:

$$\begin{cases} w_d : [0,1] \rightarrow [0,1] \in \mathcal{C}^1 \\ w_d(0) = 0 \\ w_d(1) = 1 \\ dw_d(u)/du \geq 0 \\ w_d(u) = \frac{w((N-1)Tu)}{w((N-1)T)} \end{cases} \tag{2.39}$$

The main difficulty is now to estimate the missing values of the signal by using the general class of interpolators. The first step is to express the signal into a linear shift-invariant space V_ϕ [Mei02] defined by the kernel ϕ with $V_\phi = Span(\{\phi(t-kT), k \in \mathbb{Z}\})$ [TBU00], as follows:

$$s(t) = \sum_n c[n]\,\phi(t-nT) \tag{2.40}$$

We restrict ourselves to the case of exact interpolation where $s(nT) = s[n]$. Then, signal $s(t)$ can be expressed as:

$$s(t) = \sum_{n=0}^{N-1} s(n)\,\phi_{int}(t-nT) \tag{2.41}$$

where the kernel ϕ_{int} is:

$$\phi_{int}(t) = \sum_k p[k]\,\phi(t-kT) \tag{2.42}$$

Exact interpolation is possible if and only if the following condition is met:

$$\phi_{int}(nT) = \begin{cases} 1, & if \quad n = 0 \\ 0, & if \quad n \neq 0 \end{cases} \tag{2.43}$$

Note that any interpolation kernel can be used. Jarrot et al. [JIQ06] has found that the cardinal B-spline is the optimal choice. Then, the warped discrete sequence is defined as:

$$s_w[m] = \sum_{n=0}^{N-1} s[n]\,\phi_{int}(w_d(m) - nT) \tag{2.44}$$

More details on the algorithm is provided in [JIQ06]. This shows that any discrete time warping operator could be implemented thanks to a finite set of values of the warping function. This extends time axis transformations to non analytical warping functions which means that any kind of signals can be stationnarized.

Let consider an arbitrary instantaneous frequency law $\psi(t)$ and a finite set of values $\{\psi(t_k)\}_{k=1,\ldots,L}$. The discrete warping function $w_d(t)$ that stationnarizes the signal is defined such as:

$$\begin{aligned} \psi(w_d(t_k)) &= w_d(\psi(t_k)) \\ &= t_k;\ k = 1,\ldots,L \end{aligned} \tag{2.45}$$

To solve this equation, the signal is divided into L segments in which a local estimation of the warping function is computed iteratively. Thus, the segmentation ensures $\psi(t)$ monotony

on each interval. Each interval $[I_k, I_{k+1}]$ is centered around t_k and we note $w_k = w(t_k)$. The algorithm starts by initializing $w_k^{(0)}$ such as:

$$w_k^{(0)} = \frac{1}{2}(I_k + I_{k+1}) \tag{2.46}$$

Then, at each iteration p, the local solution is calculated as follows:

$$w_k^{(p)} = w_k^{(p-1)} - sgn\left(\psi\left(w_k^{(p-1)}\right) - t_k\right)\frac{I_{k+1} - I_k}{2^{p+1}} \tag{2.47}$$

where sgn is the sign function. The process stops when the differential value between two successive iterations becomes insignificant:

$$\left|w_k^{(p+1)} - w_k^{(p)}\right| < \epsilon \tag{2.48}$$

This process enables the stationnarization of any kind of instantaneous frequency laws even when non analytical.

In order to illustrate the time axis transformation concept, let consider the example of a third degree monomial phase signal $s(n)$ for $n \in \{0, \ldots, N-1\}$ with $N = 1024$, defined as follows:

$$s(n) = e^{j\left(403.1(n/N)^3 + 2\pi 128.3(n/N)\right)} \tag{2.49}$$

A first approach would be to use the following warping function:

$$w(n/N) = (n/N)^{1/3} \tag{2.50}$$

However, due to the central frequency term of the signal $2\pi 128.3\,(n/N)$, this function is not appropriate for the stationnarization. The Short Time Fourier Transforms (STFT) of the signals obtained before and after the warping transformation are respectively shown in Figure 2.13 (a) and (b). It is obvious that the given warping function does not turn the signal into a pure sinusoid.

Another approach would be to estimate the instantaneous frequency law of the signal in order to evaluate the associated warping function (Figure 2.14) that stationnarizes the signal as presented in the previous subsection. As presented in Figure 2.13 (c), the third degree monomial phase signal has been linearized within the process. Even if the warped signal is still corrupted by some artifacts at the beginning of the sequence, it still can be considered sparse in the Fourier domain.

Due to unitary equivalence, it has been shown that it was possible to express a signal into another basis that simplify the interpretation of the observation. This is the concept used to extract the signals of interest. Furthermore, it is possible to unwarp the signal, i.e. to turn the basis of the warped signal into the original representation domain.

At this point of the chapter, we have presented how to linearize any nonlinear frequency component, but a question remains regarding its extraction. A natural approach would consider a band-pass filtering to extract it. However, when there are too many components at

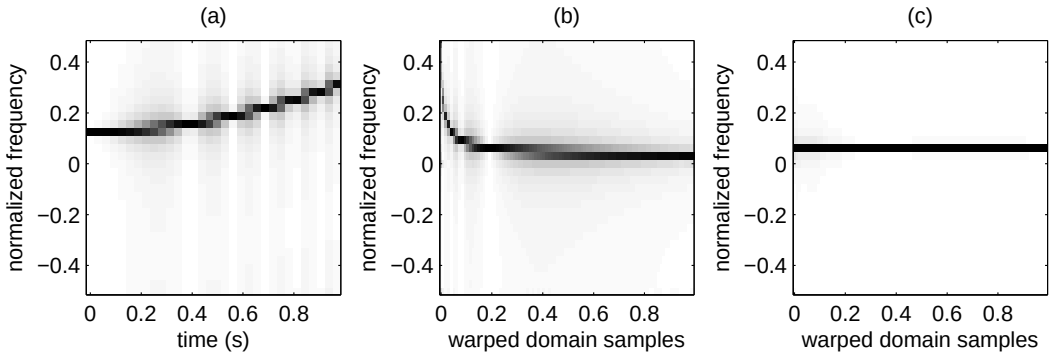

Figure 2.13: (a) STFT of the third degree monomial phase signal $s(n)$. Results of time axis transformations are then shown in (b) and (c) using respectively two warping functions: the first one is given by (2.50) and the second one is computed according to the method presented in this section.

stakes or if the component of interest is not complete, then the filtering can be compromised. This is the reason why we would like to combine compressive sensing to warping operators to perform the extraction.

2.2.3 Warping based Compressive sensing algorithm

2.2.3.1 Problem formulation

Let consider the case of a composite discrete signal $s(n)$ defined as follows:

$$s(n) = s_d(n) + s_{nd}(n) \tag{2.51}$$

where $s_d(n)$ stands for the desired signal that should be extracted and $s_{nd}(n)$ the undesired part to remove.

The desired signal is a nonlinear modulation phase signal defined as in (C.22) and (C.23). The undesired part can be composed of another nonlinear modulation phase signals, as well as nonstationary or more complex signals. The goal of this section is to extract the desired signal from the entire observation $s(n)$.

The first step is to change the underlying basis of $s(n)$ in order to turn $s_d(n)$ into a single frequency component using time axis transformation.

Because the unitary equivalence is commutative, (2.51) in the warped domain becomes:

$$\mathcal{W}s(n) = \mathcal{W}s_d(n) + \mathcal{W}s_{nd}(n) \tag{2.52}$$

where $\mathcal{W}s_d(n)$ is a single frequency component:

$$\mathcal{W}s_d(n) = \eta e^{j\lambda n} \tag{2.53}$$

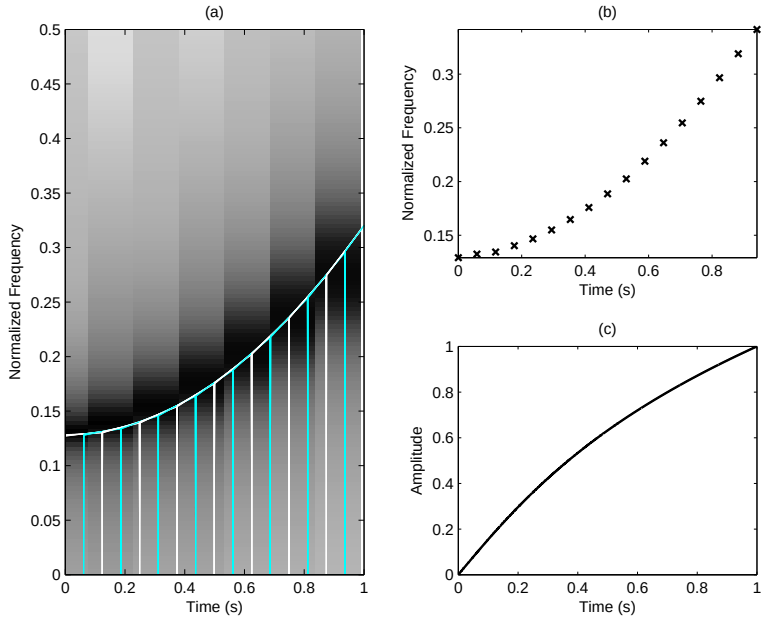

Figure 2.14: (a) Spectrogram of the studied signal and its IFL estimation. (b) IFL estimate coordinates used to compute the warping function (c) that stationnarizes the signal.

with η the amplitude of the sinusoid of frequency λ.

According to (2.53), $\mathcal{W}s_d(n)$ is assumed to be sparse in the frequency domain. The discrete Fourier transform (DFT) of $\mathcal{W}s(n)$ is:

$$\mathcal{W}S(k) = \mathcal{W}S_d(k) + \mathcal{W}S_{nd}(k) \tag{2.54}$$

where $\mathcal{W}S_d(\lambda) \neq 0$ due to the sparsity in the frequency domain of $\mathcal{W}s_d(n)$. Moreover, it is possible to consider that some frequency components in $\mathcal{W}S_{nd}(k)$ can be stronger than $\mathcal{W}S_d(\lambda)$ [SOSA13]:

$$|\mathcal{W}S_{nd}(\lambda)| >> |\mathcal{W}S_d(\lambda)| \tag{2.55}$$

For illustration purposes, Figure 2.15 presents the Fourier transform of a third degree monomial phase signal. In the case of additional noise ($-15dB$ in this example), it may be no longer possible to distinguish the frequency properties of a signal, and thus it is necessary to employ the time-frequency analysis.

2.2.3.2 L-statistics and TF analysis in warped domain

STFT of $\mathcal{W}s(n)$ using a rectangular window of width M at instant n is:

$$STFT(n,k) = \sum_{p=0}^{M-1} \mathcal{W}s(n+p)\, e^{-j2\pi kp/M} \tag{2.56}$$

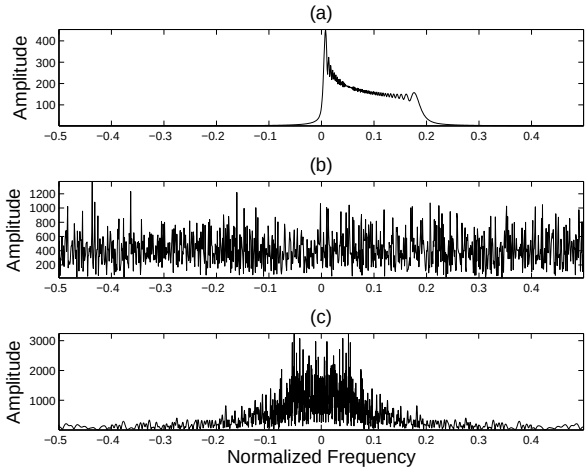

Figure 2.15: (a) Frequency content of a monomial phase signal. (b) Frequency content of the signal with additional Gaussian noise. (c) Remaining part after the warping transformation.

Because the undesired and desired frequency components can overlap in time and frequency, it is necessary to separate them. To do so, one possibility is to use the L-statistics approach [SOSA13, SSA14] to select time-frequency regions of interest.

Indeed, the desired signal is sparse in the Fourier domain, so along a given frequency line, it is possible to have only undesired components or a mix of desired and undesired components. In both cases, the highest values of the spectrogram would correspond to interference contributions or unwanted components. Another scenario can be considered when $\mathcal{W}S_{nd}(k)$ and $\mathcal{W}S_{d}(k)$ are of the same order of amplitude, it is known that opposite phases produce low values at the intersection points. All these informations lead to the assessment that we need to remove those values from consideration. To do so, data samples are first sorted out for each frequency. Then, the highest and the smallest values are discarded (i.e. replaced by a zero value). The procedure is described below.

The L-statistics is applied to $STFT(n,k)$. For each frequency k, the samples are sorted out:

$$L_k(p) = sort\{STFT(p,k), \quad p = 0,1,...,M-1\} \tag{2.57}$$

such that $|L_k(0)| \leq |L_k(1)| \leq ... \leq |L_k(M-1)|$. The removal operation is then done by discarding Q highest values and P smallest values of each L_k. The remaining STFT values consequently belong to the desired signal and a compressive sensing (CS) reconstruction algorithm can be used to reconstruct $\mathcal{W}s_d(n)$.

2.2.3.3 CS reconstruction algorithm

At instant n, the STFT of signal $\mathcal{W}s(n)$ can also be expressed as follows:

$$\mathbf{STFT}_M(n) = \mathbf{D}_M \mathbf{W}_\mathbf{s}(n) \tag{2.58}$$

where $\mathbf{STFT}_M(n)$ and $\mathbf{Ws}(n)$ are vectors in the form:

$$\mathbf{STFT}_M(n) = [STFT(n,0), ..., STFT(n,M-1)]^T \tag{2.59}$$

$$\mathbf{W_s}(n) = [\mathcal{W}s(n), \mathcal{W}s(n+1), ..., \mathcal{W}s(n+M)]^T \tag{2.60}$$

while $\mathbf{D}_M$ is the MxM DFT matrix with coefficients:

$$\mathbf{D}_M(m,k) = e^{-j2\pi mk/M}$$

As the case of non-overlapping windows is considered, the complete formulation yields to:

$$\mathbf{STFT} = \mathbf{DW_s} \tag{2.61}$$

such that vector $\mathbf{STFT}$ is composed of vectors: $\mathbf{STFT}_M(0)$, $\mathbf{STFT}_M(M)$, ..., $\mathbf{STFT}_M(N-M)$. The matrix $\mathbf{D}$ is obtained as a Kronecker product:

$$\mathbf{D} = \mathbf{I}_{N/M} \otimes \mathbf{D}_M$$

where $\mathbf{I}_{N/M}$ is the (N/M)x(N/M) identity matrix. The vector $\mathbf{W_s}$ can then be expressed as the inverse Fourier transform of the DFT vector $\mathbf{WS}$ (stands for $\mathcal{W}S$):

$$\mathbf{W_s} = \mathbf{D}_N^{-1}\mathbf{WS} \tag{2.62}$$

By combining (2.61) and (2.62), a general expression can be obtained:

$$\mathbf{STFT} = \mathbf{A}_{FULL}\mathbf{WS} \tag{2.63}$$

with $\mathbf{A}_{FULL} = \mathbf{DD}_N^{-1}$.

At this point of the study, matrix $\mathbf{A}_{FULL}$ maps the integrality of the TF representation. By using the L-statitics method [SOSA13], it is possible to create a CS mask $\mathbf{A}_{CS}$ that will remove the TF values that do not belong to the desired signal from the spectrogram. We then dispose of a spectrogram $\mathbf{STFT}_{CS}$ that has been cleansed of all undesired signals frequency components. The next step is to reconstruct the desired signal by minimizing the following problem:

$$min\,\|X\|_1 = min\sum_{k=0}^{N-1}|X(k)| \quad subject\ to \tag{2.64}$$

$$STFT_{CS} = A_{CS}X$$

The reconstructed DFT $\mathbf{X}$ is used to obtain $\mathcal{W}s(n)$ which corresponds to $\mathcal{W}s_d(n)$ due to the elimination of all the non desired components. An unwarping process is then applied to the estimated signal in order to express it in the original temporal domain.

The Warping Based Compressive Sensing algorithm (WBCS) is the result of two contributions: the warping described in the previous section and a compressive sensing method

introduced by Stankovic et al. [SOSA13]. It permits the detection and extraction of nonlinear modulation phase signals even when they overlap in time and frequency, and also when parts of them are missing. First, the warping operation enables to express the desired signal into a pure sinusoid that is sparse in the Fourier domain, then, the CS algorithm removes all the undesired components. It seems that the desired component could be estimated as the most important peak in the Fourier transform of the warped signal, but also it can be of lower energy and hidden among other information. Thus, it is the point where the combined L-estimation and CS reconstruction provide main contribution.

The complete procedure is finally summarized in Figure 2.16. Next Section is dedicated to the study of an example.

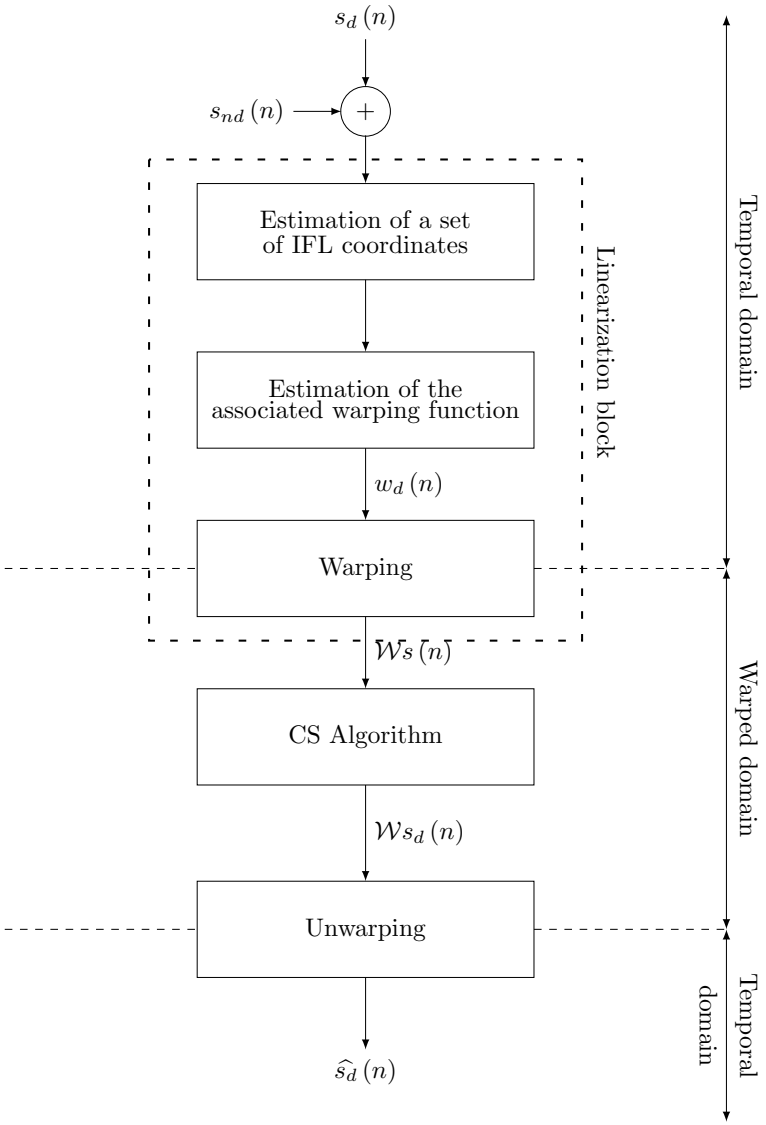

Figure 2.16: The steps of the algorithm that performs the nonlinear modulation phase signal extraction.

2.2.4 Numerical example

2.2.4.1 Presentation of the example

Let consider a desired signal $s_d(n)$ defined for $n \in \{1, \ldots, N\}$, composed of two nonlinear modulation phase signals $s_1(n)$ and $s_2(n)$:

$$s_d(n) = s_1(n) + s_2(n) \tag{2.65}$$

with:

$$s_1(n) = 2.5e^{j(708ln(n/N+1)+2*\pi 50n/N)} \tag{2.66}$$

$$s_2(n) = 1.9e^{j\left(90(n/N)^2+2\pi 90n/N\right)} \tag{2.67}$$

disturbed by nonstationary disturbances composed of short duration modulated signal $b(n)$:

$$b(n) = \sum_{i=1}^{p} A_i e^{jw_i n} e^{-(n-n_i)^2/d_i^2} \tag{2.68}$$

with p the number of corrupting noise components, A_i their amplitude, w_i their frequency, and n_i and d_i their center and variance distributions respectively. A sine modulated component is also introduced in the desired signal in order to add coherent signal difficult to separate.

Signal-to-noise ratio (SNR) is defined as follows:

$$\mathbf{SNR}_{dB} = 10\log_{10}\frac{\sum_{n=1}^{N} s_d^2(n)}{\sum_{n=1}^{N} s_{nd}^2(n)} \tag{2.69}$$

with $s_{nd}(n)$ refering to unwanted signals such as nonstationary disturbances $b(n)$ and coherent signals that are not nonlinear modulation phase signals.

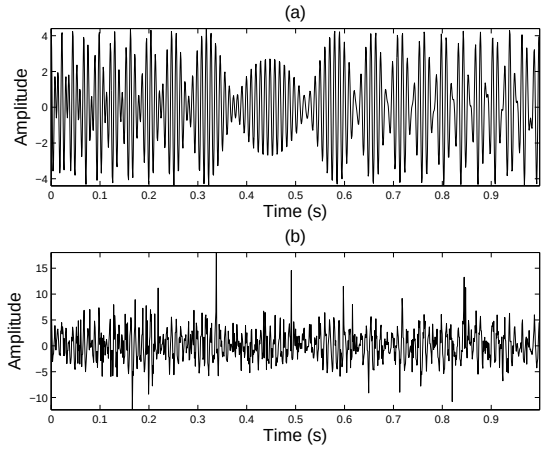

Figure 2.17: Temporal data of noise free signal (a) and with additional nonstationary noise (b).

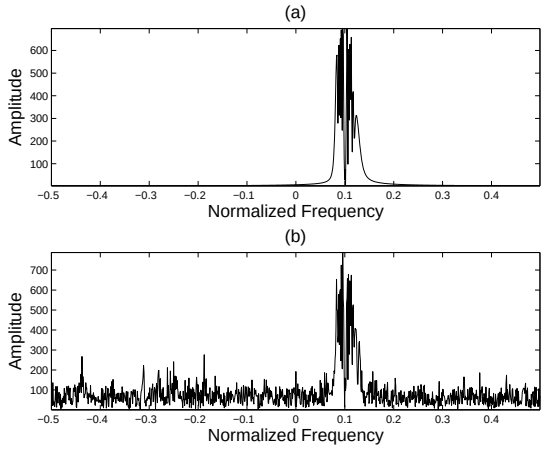

Figure 2.18: Fourier transform of the noise-free signal (a) and with additional nonstationary noise (b). The SNR is 1.97 dB.

Time and frequency domain signals are presented in Figures 2.17 and 2.18. Figure 2.19 presents the spectrogram of the studied signal using a 128 samples length Hamming window and 127 samples of overlapping. According to Equation 2.69, the signal-to-noise ratio is 1.97 dB. As we can see, the 2 nonlinear modulation phase signals overlap in time and frequency which makes really difficult the extraction of each component. The goal of this example is to estimate the 2 signals $s_1(n)$ and $s_2(n)$'s IFL.

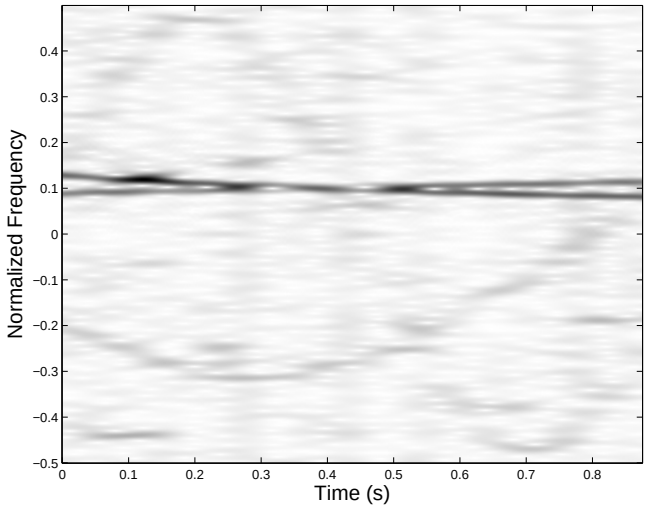

Figure 2.19: Spectrogram of the studied signal. The two non-linear modulation phase signals are mixed with coherent signals and many disturbances.

In this subsection, we propose to compare two techniques to extract the 2 IFLs of interest: the first one is based on the association of warping operators and band-pass filtering, while the second approach focuses on the WBCS algorithm.

2.2.4.2 Separation processing based on warping operators and band-pass filtering

One possible and natural approach to perform this task is to estimate the first component, then remove it from consideration, and again estimate the second component. To estimate each component, we can stationnarize each components of interest one by one with warping operators and then extract them with a band-pass filtering.

As it has been stated in Section 2.2.2, to stationnarize a signal, we first need to estimate correctly some of its IFL's coordinates. This is performed by an algorithm of phase tracking developed by [IGSM10] which manages to track the time-frequency component based on their local continuity. To do so, the signal is divided into intervals in which an estimation of the local-best matched IFLs is performed. In this example, the algorithm provides a set of 32 coordinates for the IFL which is enough to estimate a warping function that stationnarizes the component.

Figure 2.20(a) shows the results of the tracking algorithm and the set of IFL coordinates

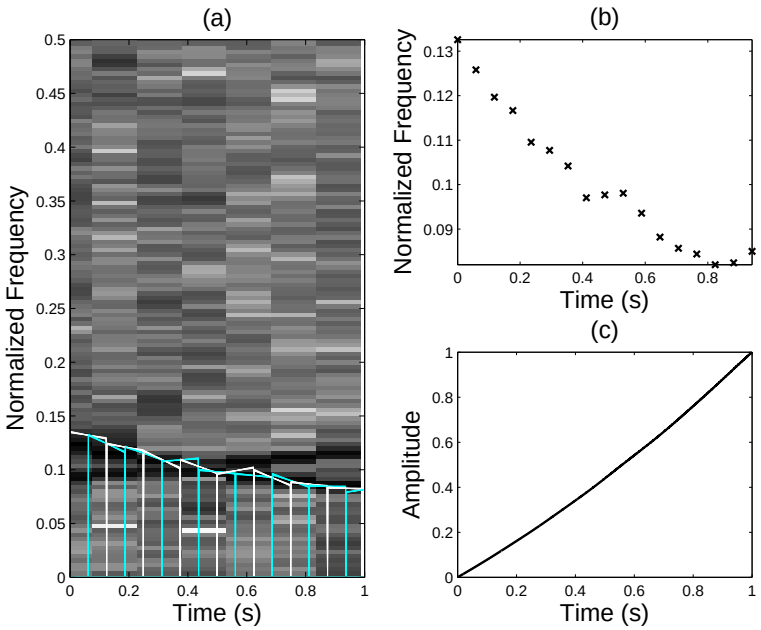

Figure 2.20: (a) Spectrogram of the signal and result of the tracking method for the estimation of the IFL coordinates of the most powerfull signal (b). The associated warping function that stationnarizes the corresponding component is then estimated in (c).

estimated (b) used to calculate the associated warping function (c). After the warping operation, the most powerfull component of the signal is expressed as a pure sinusoid mixed with perturbations in the warped domain. We notice here that even if the IFL traking is subject to error, it enables to stationarize the component of interest.

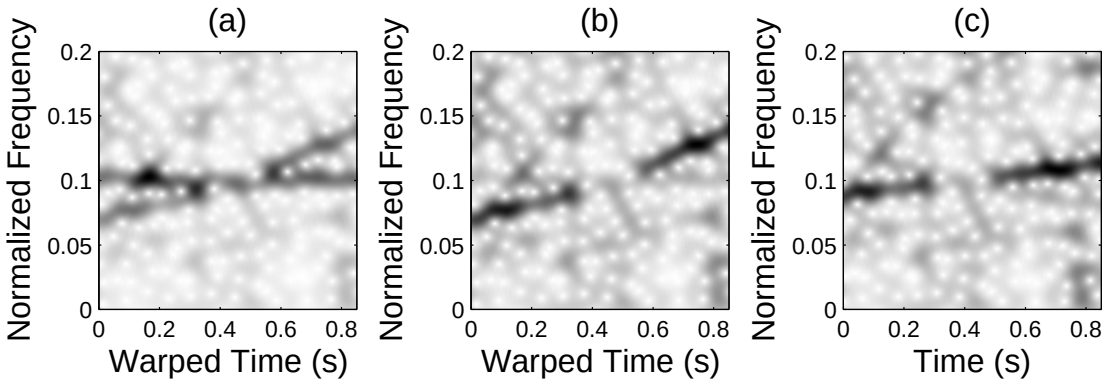

Figure 2.21: (a) Spectrogram of the warped signal. (b) Spectrogram of the filtered warped signal: the most powerfull component has been removed. (c) Spectrogram of the filtered signal in the original time domain.

The next step is then to use a band-pass filter to extract the component that has been stationnarized, perform an inverse time-axis transformation to express the selected component in the original time domain as $\widehat{s_1}(n)$ and finally calculate its IFL. The band-pass filter is a

300-th order filter that has a bandpass of $\frac{0.003}{N}$ centered around the central frequency given by the maximal peak of frequency of the warped signal's spectrum. Figure 2.21(a) shows the spectrogram of the warped signal where the most powerful component is represented by a sinusoid.

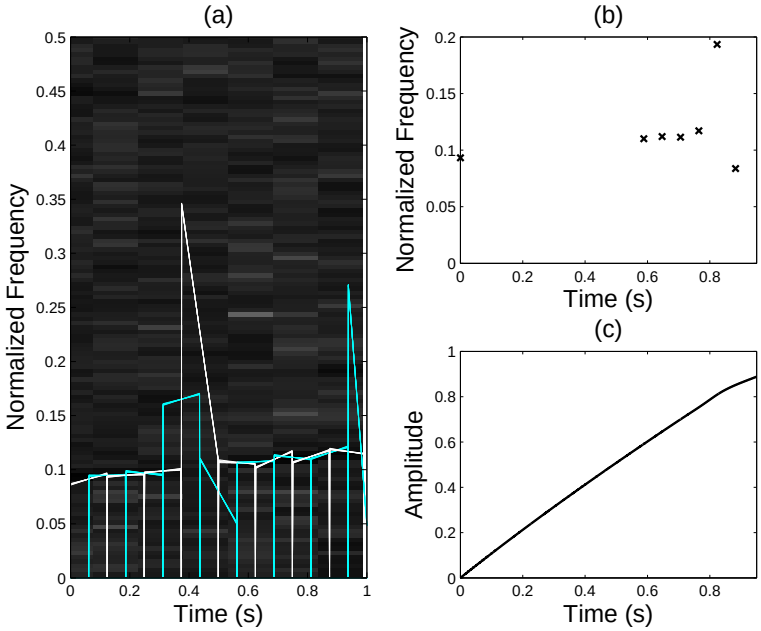

Figure 2.22: (a) Spetrogram of the filtered signal and result of the tracking method for the estimation of the IFL coordinates of the second component (b). The associated warping function that stationnarizes the corresponding component is then estimated in (c).

Afterwards, we still need to estimate the second component. To do so, we perform a notch filter (with the same parameters used for the band-pass filter) to remove the first component from the warped signal (Figure 2.21(b)). We can see that the second component is no longer trackable as the middle part of the time-frequency component is missing from the spectrogram. At this point of the study, it becomes complicated to estimate the second component of the signal as a part of it has been removed with the notch filter. The filtered signal is then expressed in the original time domain with an inverse time-axis transformation: we obtain the original signal reduced with the first component (Figure 2.21(c)). We then estimate a set of the second component IFL's coordinates in order to estimate a warping function that stationnarize it and perform the associated warping operation (Figure 2.22). The second component is turned into a single sinusoid with missing values in time-frequency (Figure 2.23). The natural approach is then to perform a second band-pass filtering to extract the second component, followed by an inverse time-axis transformation. This is usually where the method becomes limited. Due to the missing values of the second component, the algorithm fails to extract properly the signal of interest $\widehat{s_2}(n)$. This is shown in Figure 2.25 where we can see that the estimated IFL of $\widehat{s_2}(n)$ is not the same as the theoretical one.

We have seen in this subsection that the association of warping operators and band-pass filters was not efficient to separate nonlinear modulation phase signals that overlap in time

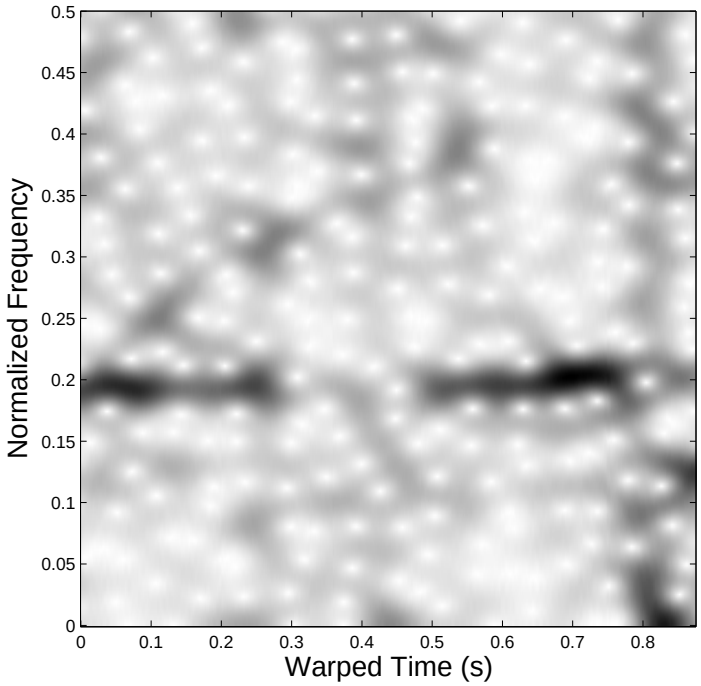

Figure 2.23: Spectrogram of the second component after the warping process.

and frequency. This is the reason why we need to use a compressive sensing approach to reconstruct the two signals of interest.

2.2.4.3 Separation processing using the WBCS algorithm

In this subsection, we focus on the recovery of the second component after the first component filtering performed in the previous subsection. Due to its missing values, the signal is a good candidate to the warped-based compressive sensing algorithm.

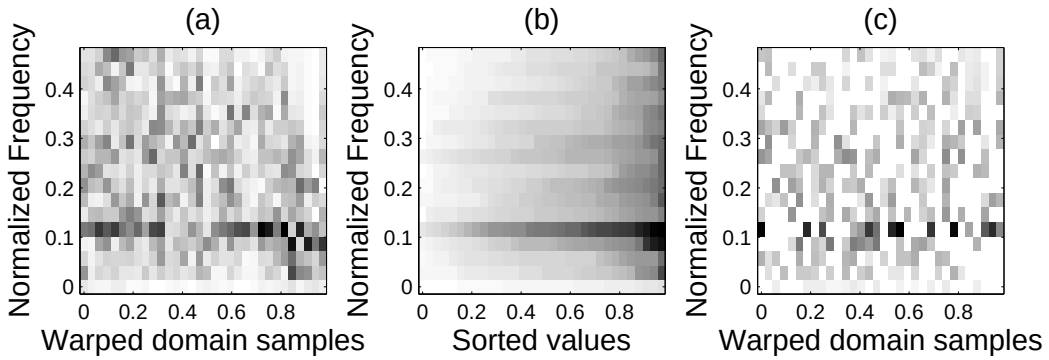

Figure 2.24: (a) STFT of the warped signal, the sorted values for each frequency of the STFT (b) and the CS STFT remaining after the L-statistics process (c).

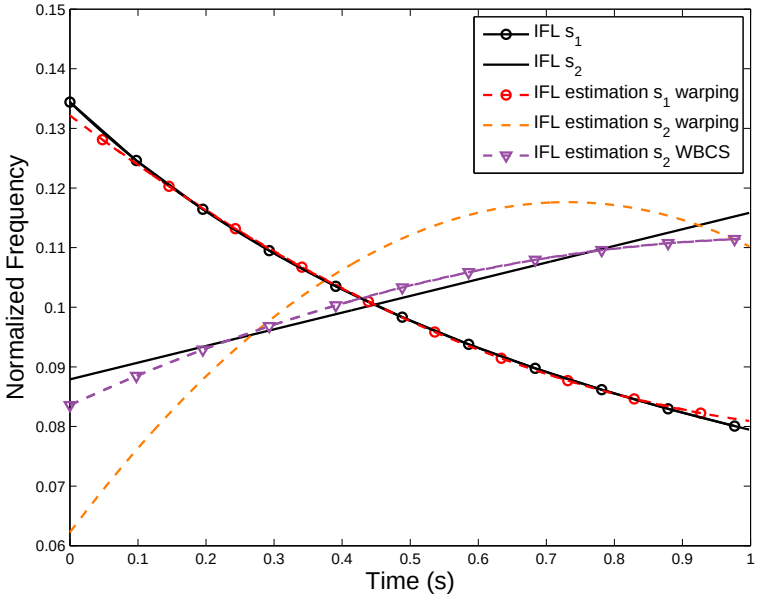

Figure 2.25: IFL estimates of $s_1(n)$ and $s_2(n)$ calculated from the original signals, and the extracted signals obtained with the warping and WBCS algorithms.

We first start from the linearization of the second component presented in the previous subsection (Figure 2.22). The STFT of the warped signal is then performed using a 32 samples rectangular window with no overlapping (Figure 2.24(a)). For each frequency, the STFT values are sorted out (Figure 2.24(b)) and according to the L-statistics process, 50% of the largest values are removed along with 8% of the smallest values. The CS spectrogram values that remain after the L-statistics removal are shown in Figure 2.24(c). A reconstruction algorithm is then applied to the CS STFT which permits to reconstruct the sinusoid of interest. Subsequently, an inverse time-axis transformation is performed to recontruct the nonlinear modulation phase signal $\widehat{s_2}(n)$ in the original time domain.

Figure 2.25 shows the IFL of $\widehat{s_2}(n)$ obtained with the WBCS algorithm. As we can see, the result is better than the one obtained with the traditional band-pass filtering and enables to reconstruct the signal of interest even if a part is missing.

2.2.4.4 Comparative results

Next step is then to compare the results obtained with the two described techniques. We evaluate the mean square error (MSE) between the estimated IFLs and the theoretical ones. But first, we define the MSE as follows:

$$\mathbf{MSE} = \frac{1}{N}\sum_{k=1}^{N}(y_k - \widehat{y_k})^2 \tag{2.70}$$

where y_k stands for the known IFL and $\widehat{y_k}$ for its estimate.

	$s_1(n)$ with warping	$s_2(n)$ with warping	$s_2(n)$ with WBCS
MSE (Hz)	0.3529	100.2504	3.5276

Table 2.2: MSE results of the IFL estimates obtained with the WBCS algorithm.

Table 2.2 presents the MSE of the 3 reconstructed signals: $\widehat{s_1}(n)$ and $\widehat{s_2}(n)$ obtained with the warping and the band-pass filtering, and $\widehat{s_2}(n)$ obtained with the WBCS algorithm. We can see that this last algorithm perfoms much better than the traditional one when it comes to estimate the second component as it enables to overcome the limitation introduced by the missing values of the signal.

2.2.5 Summary

This section proposed a new approach for nonlinear frequency extraction that enables to overcome the limitation when parts of the signals are missing. It takes advantages of a warping transformation that turns the desired signal into a sinusoid and the L-statistics that permits to select time-frequency regions of interest. Then, a CS reconstruction algorithm is used to regenerate the signal in the warped domain. Finally, a second time axis transformation is performed to express the reconstructed warped signal in the original time domain.

This work has been realised in contribution with University of Montenegro and supported by the Montenegrin Ministry of Science, project grant "New ICT Compressive sensing based trends applied to: multimedia, biomedicine and communications" (ACRONYM: CS-ICT). During this project, I visited the University of Montenegro in November 2013 for a period of ten days. Our collaboration led to the publication of a journal paper and a conference paper:

C. Bernard, I. Orovic, C. Ioana. and S. Stanković. Compressive sensing based separation of nonlinear modulation phase signals. *IEEE Transactions on Signal Processing*, under review.

C. Bernard, C. Ioana., I. Orovic and S. Stanković. Analysis of underwater signals with nonlinear time-frequency structures using warping-based compressive sensing algorithm. *IEEE Oceans Conference*, October 2015.

Chapter 3

Phase diagram-based transient signal analysis

Contents

In Chapter 1, we introduced some general topics where the transient signal characterization is a challenging task. The phase diagram analysis is a potential class of techniques that can offer interesting information regarding the signal shapes. However, we have seen that the parameter setting (i.e. m and τ chosing) in the RPA is not an easy task. The choice of this parameter set is actually a current interesting field in RPA domain, this is the reason why we decided to develop the concept of multi-lag phase diagram analysis (MLPDA) to take into account all the information that could be extracted from each representation. This new concept is then successfuly applied to solve the general problem of exploring transient signals. We mention here that we concentrate on phase diagram that is a more general representation domain than the RPA.

3.1 Mathematical properties of lag diversity in phase diagram

In this chapter, in order to illustrate the concept of multi-lag PDA, we consider a signal modeled as a modulated cosine $s(n)$ defined for $n \in \{1, \ldots, N\}$ such as:

$$s(n) = \begin{cases} \cos(2\pi f_0 n)\, w(n) & \text{if} \quad n \in [n_0, n_0 + \Delta] \\ 0 & \text{otherwise} \end{cases} \tag{3.1}$$

with $w(n)$ a modulating window (such as a Hanning window), f_0 the central frequency of the modulation (we consider $f_0 = 3$ in our examples), n_0 the beginning of the transient and Δ the transient duration.

Phase space diagram analysis of signal $s(n)$, using the embedding dimension m and lag τ, corresponds to a representation T that is defined as follows:

$$\begin{array}{rccc} T: & \mathbb{R}^N \mathtt{x} \mathbb{N} \mathtt{x} \mathbb{N} & \longrightarrow & \mathcal{M}_{N-(m-1)\tau,m}(\mathbb{R}) \\ & (s,\tau,m) & \longmapsto & T_{m,\tau}(s) \end{array} \tag{3.2}$$

where:

$$T_{m,\tau}(s) = \begin{pmatrix} s(1) & \dots & s(1+(j-1)\tau) & \dots & s(1+(m-1)\tau) \\ s(2) & \dots & s(2+(j-1)\tau) & \dots & s(2+(m-1)\tau) \\ \vdots & & & & \\ s(i) & \dots & s(i+(j-1)\tau) & \dots & s(i+(m-1)\tau) \\ \vdots & & & & \\ s(N-(m-1)\tau) & \dots & s(N-(m-1)\tau+(j-1)\tau) & \dots & s(N) \end{pmatrix} \tag{3.3}$$

which can be summarized by:

$$T_{m,\tau}(s) = \{t_{i,j}\}_{i=\{1,2\dots,N-(m-1)\tau\},j=\{1,2,\dots,m\}} \tag{3.4}$$

with:

$$t_{i,j} = s(i+(j-1)\tau) \tag{3.5}$$

Each row of the T matrix corresponds to a phase space vector defined as in Equation 1.16. Each column corresponds to the coordinates of one axis of the phase space.

Let us now investigate the properties of this representation to the time-shift operator, the scale operator and amplitudes changes. We define three signals $s_1(n)$, $s_2(n)$ and $s_3(n)$ such as:

$$s_1(n) = s(n+\delta) \tag{3.6}$$
$$s_2(n) = s(\alpha n) \tag{3.7}$$
$$s_3(n) = \beta s(n) \tag{3.8}$$

with δ the time-shift delay, $\alpha \in \mathbb{R}^+$ the dilation coefficient and β an amplitude modification coefficient. We propose to illustrate the different properties with equations and numerical examples that are shown in Figure 3.1. The numerical examples are computed with the following parameters: $\delta = 55$, $\alpha = 2$ and $\beta = 1.5$.

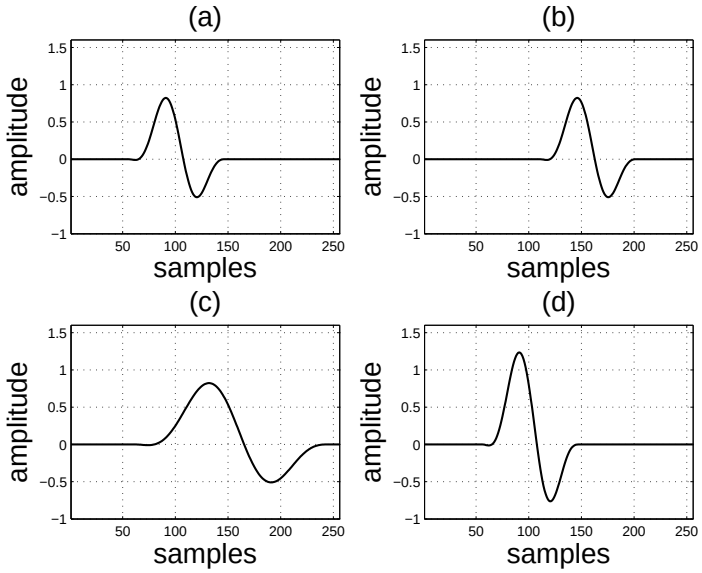

Figure 3.1: Temporal data of: (a) $s(n)$, (b) $s_1(n)$, (c) $s_2(n)$ and (d) $s_3(n)$

Investigation of the time-shift invariance property

We can start by considering the phase space vector of $s_1(n)$ at instant n and the relation given by 3.6. We have:

$$\begin{aligned}[s_1(n), s_1(n+\tau), \ldots, s_1(n+(m-1)\tau)] &= [s(n+\delta), s(n+\delta+\tau), \ldots, s(n+\delta+(m-1)\tau)] \\ &= [s(n_0)\, s(n_0+\tau), \ldots, s(n_0+(m-1)\tau)]\end{aligned} \tag{3.9}$$

This result states that even **if two identical signals are time-shifted, their phase space diagrams are invariant**. Mathematically speaking, it means that the rows of $T_{m,\tau}(s_1)$ are the same as $T_{m,\tau}(s)$'s but they suffered the circular permutation and are shifted compared to $T_{m,\tau}(s)$. This property is illustrated by Figure 3.2 where we can see that for $m = 2$ and $\tau = 8$ the phase space diagrams of the two signals are exactly the same despite the time-shift between the signals.

Investigation of the time-scaling property

We now consider $s_1(n)$'s phase space vector at instant n and the relation given by 3.7. We have:

$$\begin{aligned}[s_2(n), s_2(n+\tau), \ldots, s_2(n+(m-1)\tau)] &= [s(\alpha n+n_0), \ldots, s(\alpha(n+(m-1)\tau)+n_0)] \\ &= [s(n_1), s(n_1+\alpha\tau), \ldots, s(n_1+(m-1)\alpha\tau)] \\ &= [s(n_1), s(n_1+\tau_0), \ldots, s(n_1+(m-1)\tau_0)]\end{aligned} \tag{3.10}$$

This result states that **for a given m there exists many sets of lags $[\tau, \alpha\tau]$ that enable an invariance of phase space diagrams.** It means that it is possible to identify two signals

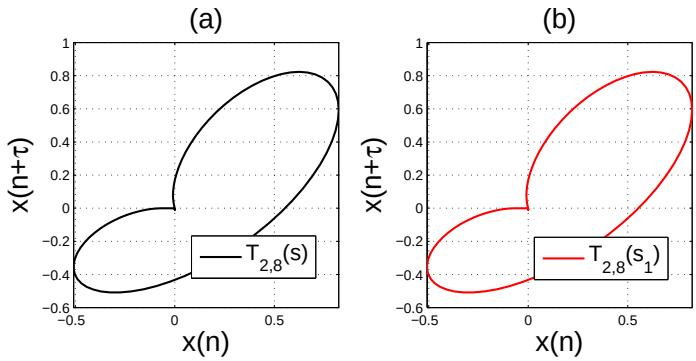

Figure 3.2: (a) $T_{2,4}(s)$ and (b) $T_{2,4}(s_1)$ phase space diagrams. The trajectories are the same despite the time-shift.

that are related by a dilation. Figure 3.3 presents the phase space diagrams of $s(n)$ and $s_1(n)$ for two differents sets of lags: $[4,4]$ and $[4,8]$. For the first set, the two diagrams do not overlap, whereas the second set enables a perfect superposition of the two diagrams.

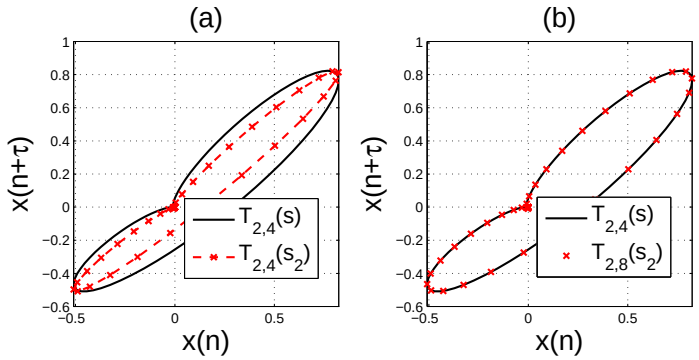

Figure 3.3: Phase space diagrams of $s(n)$ and $s_2(n)$ for $m=2$ and different sets of lags: (a) $[4,4]$ and (b) $[4,8]$. The dilation connection between the two signals can be enlightened by using the appropriate set of lags.

Investigation of the amplitude coefficient modification

Finally, we consider $s_3(n)$'s phase space vector at instant n and the relation given by 3.8. We have:

$$\begin{aligned}[s_3(n), s_3(n+\tau), \ldots, s_3(n+(m-1)\tau)] &= [\beta s(n), \beta s(n+\tau), \ldots, \beta s(n+(m-1)\tau)] \\ &= \beta[s(n), s(n+\tau), \ldots, s(n+(m-1)\tau)]\end{aligned} \tag{3.11}$$

which can be summarized by:

$$T_{m,\tau}(s_3) = \beta T_{m,\tau}(s) \tag{3.12}$$

This result shows that **the amplitude change is equivalent, in the phase space diagram representation, with a shape-invariant scale transformation.** This is illustrated by

Figure 3.4.

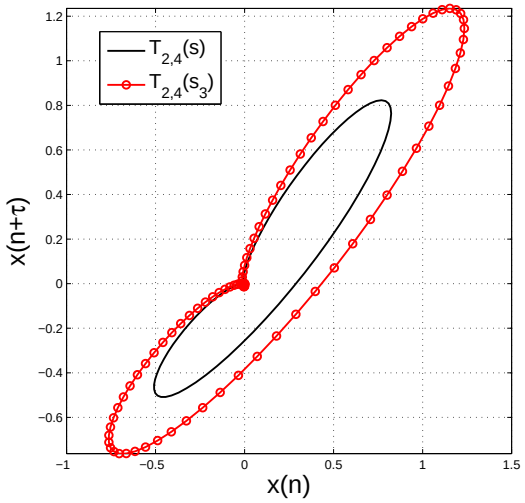

Figure 3.4: $T_{2,4}(s_3)$ and $T_{2,4}(s)$ phase space diagrams. They are related by a shape-invariant scale transformation.

3.2 Multi-lag phase diagram analysis

The previous section has shown that phase diagram representations can potentially be invariant to the main transforms of signals such as: time-shift, time-scale changes, amplitude modification, etc... The key point of the multi-lag based representation is that the invariance can be controlled by the lag choice, which makes possible a better exploration of the anayzed signals.

In this section, we propose different methods to extract parsimonious parameters from each diagram acquired for a given lag. The evolution of these parameters with respect to the lags is then explored conducting to new representation tools for transients.

In this section, we restrained ourselves to $m = 2$ in order to visualize the results but the work can be extended to higher embedding dimension. We also note $y(n)$ for $x(n+\tau)$ in order to simplify the notations.

3.2.1 Ellipse modeling

Generally, signals can have various trajectories with different shapes, but in this subsection, we propose a general model for **approximation of trajectories based on ellipse shape** (Figure 3.5). This choice is quite natural since the ellipse model is specific to harmonic signals. Therefore, the model is simple and enables to extract three parameters per phase space diagrams:

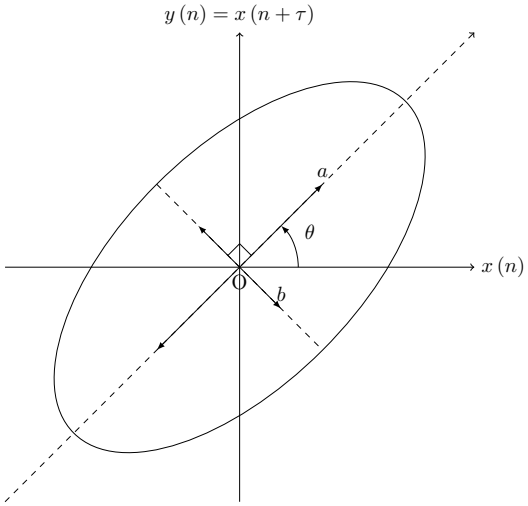

Figure 3.5: Ellipse modeling: major and minor axis are determined by an SVD on phase space diagram, and a least square fitting method is used to calculate a and b.

- the polar angle θ of the ellipse assuming that θ is the angle between the first axis and the major semi-axis
- the major semi-axis a
- the minor semi-axis b

We assume the center of the ellipse being the center of phase space diagrams as transients can be considered as zero-mean signals.

The first step consists in performing a singular value decomposition (SVD) of the phase space diagram to calculate its eigenvectors. Those are of great interest as they define a new basis that reflects the distribution of the data and also correspond to the major and minor axis of the ellipse model. Then, a least squares fitting method is performed to determine the ellipse that satisfy the following equation in the new basis defined by the eigenvectors:

$$Ax^2 + By^2 = 1 \tag{3.13}$$

where the semi-major and semi-minor axis are given by:

$$\begin{cases} a &= 1/\sqrt{A} \\ b &= 1/\sqrt{B} \end{cases} \tag{3.14}$$

Details on the method are provided in Appendix A.

At this point of the study, each diagram is modeled by an ellipse with these three parameters $[a, b, \theta]$. The evolution of θ enables to estimate an apparent periodicity of the transient, while the evolution of a and b enables to know how the data is distributed in the phase space. If they are scattered over a large area, it means that the lag used to construct the representation is not representative of the transient contruction. On the other hand, if they are rather

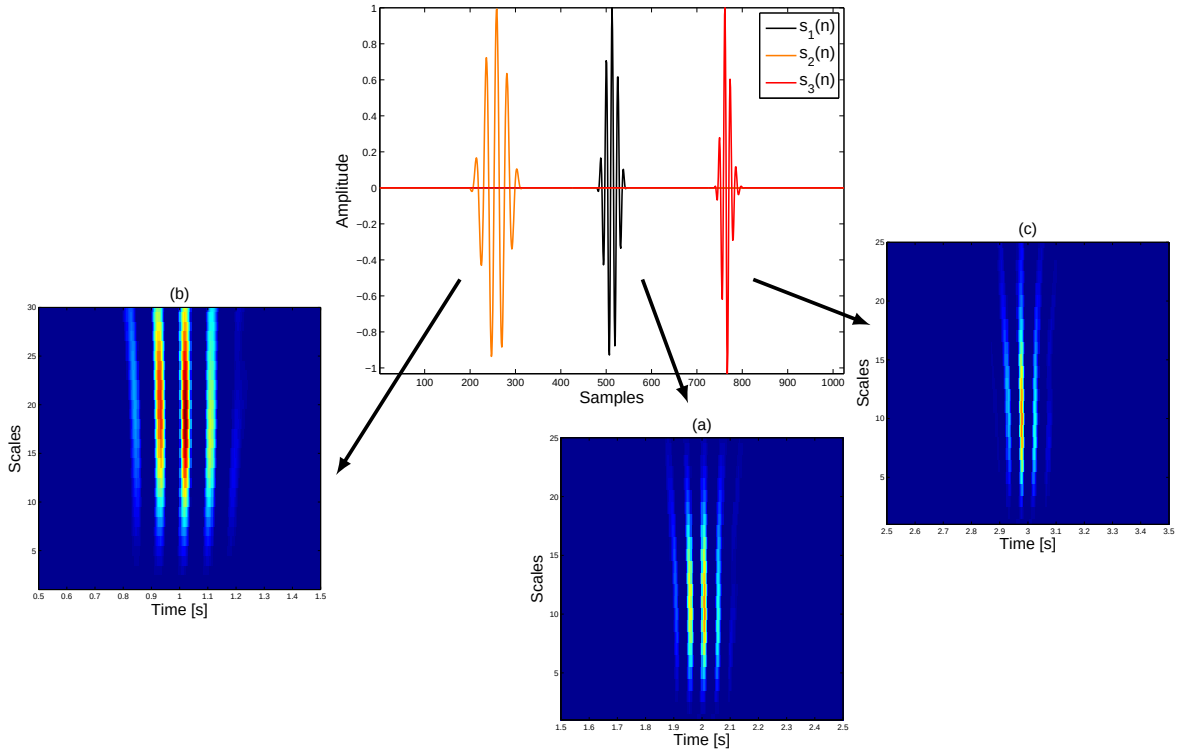

Figure 3.6: Temporal signals studied in this section and its wavelet transforms using the Daubechies mother wavelet.

confined into a smaller area, it means that the lag is representative and is well adapted to the study of this transient.

In order to illustrate the method, let consider three signals $s_1(n)$, $s_2(n)$ and $s_3(n)$ that are modulated cosines. $s_1(n)$ and $s_2(n)$ are related by a time-scale transformation while $s_3(n)$ is the result of a 10-th low-pass FIR digital filtering applied on $s_1(n)$ with the normalized cutoff frequency of 0.1. Temporal signals are shown in Figure 3.6. At first look, it is quite difficult to tell appart $s_1(n)$ from $s_3(n)$ and a time-scale analysis would not do better as their frequency content are really close (Figure 3.6).

For the three signals and $\tau \in \{1, \ldots, 30\}$, we model each phase diagram by an ellipse and record the variation of a, b and θ with respect to the lags. As we can see in Figures 3.7 and 3.8, the 3 parameters present an apparent periodicity that are related to the apparent periodicities of the signals. We call *apparent periodicity the number of samples between two successive zero-crossing*. As an example, the number of lags between two successive maxima of θ is equal to 13 for $s_1(n)$, 23 for $s_2(n)$ and 12 for $s_3(n)$, while the apparent periodicity is of 12.5 samples for $s_1(n)$, 22.25 for $s_2(n)$ and 11.75 for $s_3(n)$ which is coherent with the previous values.

The periodicity of a and b corresponds to the half period of the signals (Figure 3.8). Their maximal values correspond to phase diagrams that can be modeled by circles (same value for

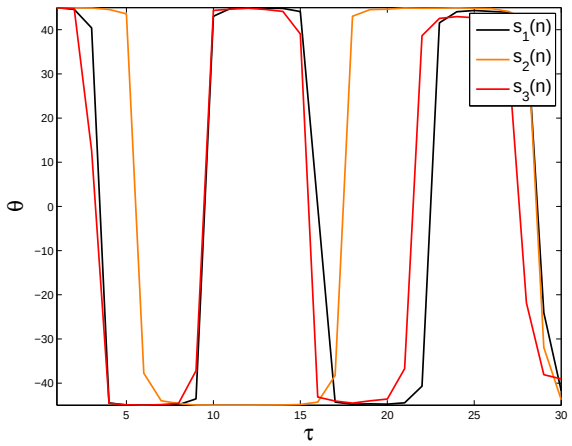

Figure 3.7: Evolution of θ with respect of τ for the three studied signals.

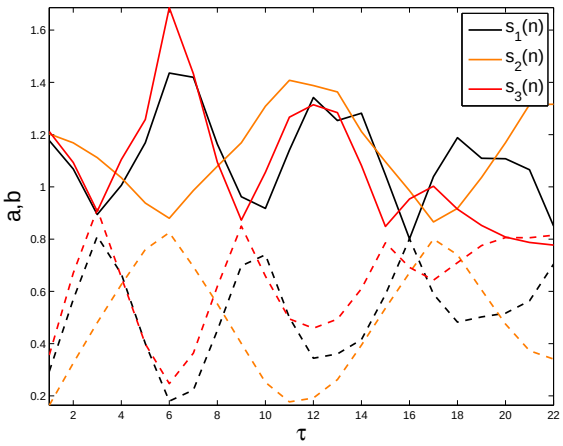

Figure 3.8: Evolution of a (continuous line) and b (dashed line) with respect of τ for the 3 studied signals.

both parameters), meaning that the phase diagrams are more scattered in the phase space. This can be seen in Figure 3.9 where we plotted $s_1(n)$'s phase diagrams for $m = 2$ and $\tau = \{3, 6\}$. For $\tau = 3$ that enables to obtain a maximal value for b, the phase diagram can be modeled by a circle and is well distributed in the space, while for $\tau = 6$, the phase diagram is concentrated into a smaller area.

We have seen that with the ellipse modeling it was posssible to summarize each representation by only three parameters and estimate the apparent frequency of a transient. We can also explore the distribution of the diagram in the phase space which is of great interest as it enables to highlight the lags that provide a great concentration of the data or on the contrary a dispersal.

3.2.2 Trend modeling

In the previous subsection, we have seen that phase diagrams were more or less concentrated around a line that tends to rotate around the origin of the phase space (due to the zero-mean of the modeled signals). This is why, we want to model this line as a third degree polynomial (Figure 3.10) in order to quantify the rotation and the natural trend of the diagram. The model is defined as follows:

$$y = \widehat{a}x^3 + \widehat{b}x^2 + \widehat{c}x + \widehat{d} \tag{3.15}$$

To do so, we consider the diagram as a scatterplot and perform a least square fitting estimation by minimizing the following sum:

$$\underset{\widehat{a},\widehat{b},\widehat{c},\widehat{d}}{Argmin} \sum_{i=1}^{N} \left(s(i+\tau) - \left(\widehat{a}s^3(i) + \widehat{b}s^2(i) + \widehat{c}s(i) + \widehat{d} \right) \right) \tag{3.16}$$

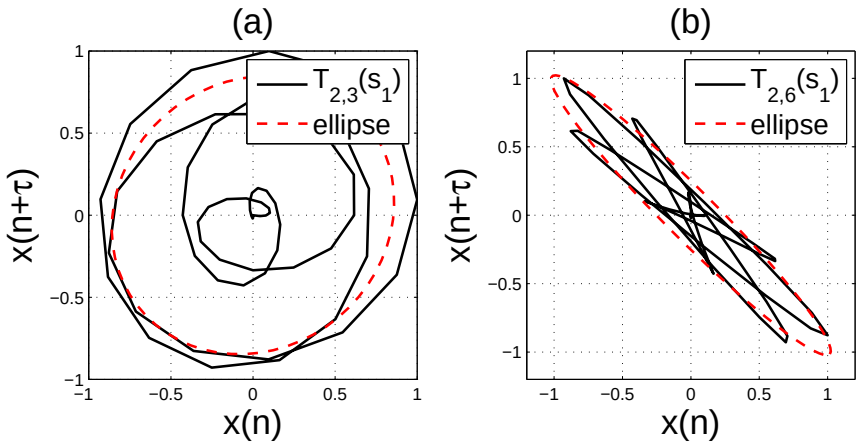

Figure 3.9: (a) $T_{2,3}(s_1)$ phase space diagram and its associated ellipse model. (b) $T_{2,6}(s_1)$ phase space diagram and its associated ellipse model.

where $s(i)$ corresponds to the analyzed signal for $i \in \{1, \ldots, N\}$; N being the number of samples.

Therefore, for each representation, phase diagrams are summarized by four parameters $\left\{\widehat{a}_\tau, \widehat{b}_\tau, \widehat{c}_\tau, \widehat{d}_\tau\right\}$ that vary with respect to τ. As studied signals can always be considered as zeros mean, we can remove from consideration $\widehat{d}$: this parameter will always be equal to zero. Thus, three parameters remain: $\widehat{a}$, $\widehat{b}$ and $\widehat{c}$. They enable to discriminate transients by looking at their evolutions with respect to τ and they also permit to highlight similitudes by looking at one parameter with respect to another. This last representation allows to get rid of the evolution of τ and investigate if whether or not the diagrams have similar trends for different lags: this can reflect a time-scaling operation.

To illustrate the concept of trend modeling, we consider the three signals that were introduced in the previous subsection. For all of them and $\tau = \{1, \ldots, 30\}$, we model each phase diagram's trend by a third degree polynomial and record the variations of the four parameters with respect to the lag. As we can see in Figure 3.11, it is quite easy to discriminate between $s_1(n)$ and $s_3(n)$ by looking at the evolution of the parameters of interest. The apparent periodicity of the parameters corresponds to the apparent periodicity of the signals. As an example, the number of lags between two successive maxima of $\widehat{c}$ is equal to 12 for $s_1(n)$, 22 for $s_2(n)$ and 11 for $s_3(n)$, while the apparent periodicity is of 12.5 samples for $s_1(n)$, 22.25 for $s_2(n)$ and 11.75 for $s_3(n)$ which is coherent with the theoretical values. We can also notice that the evolution of $\widehat{d}$'s is very small (below 0.0001), as well as for the evolution of parameter $\widehat{b}$. This is why we remove this last parameter from consideration as well.

Figure 3.12 presents the evolution of $\widehat{c}$ with respect to the evolution of $\widehat{a}$. This representation is interesting as we get rid of the evolution of τ. It enables to highlight signals that would have the same phase diagram's trends for different values of lags. This is the case for $s_1(n)$ and $s_2(n)$ where the evolution of $[\widehat{a}, \widehat{c}]$ for both signals overlap in the representation. This is coherent as the two signals are related by a time-scale operator. As $s_1(n)$ and $s_3(n)$

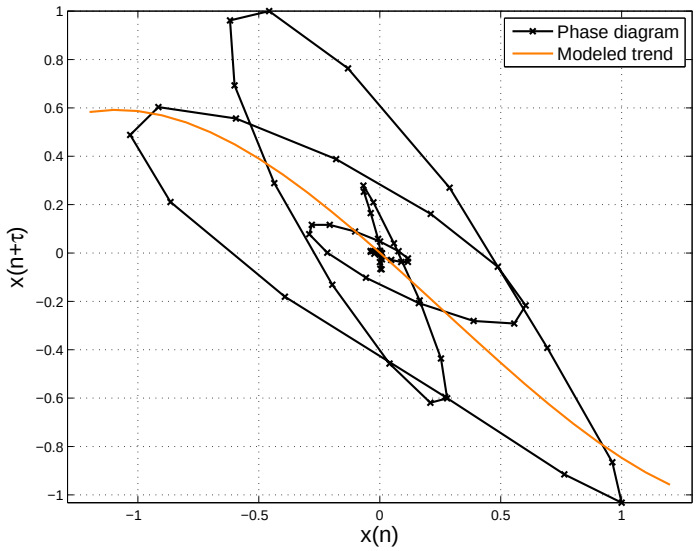

Figure 3.10: Phase diagram's trend is modeled by a third degree polynomial.

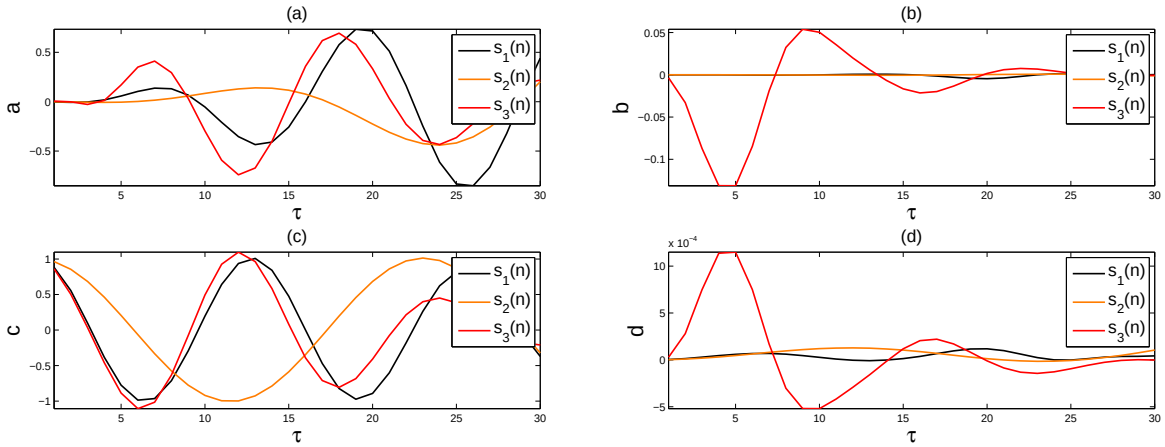

Figure 3.11: Evolution of (a) $\widehat{a}$,(b) $\widehat{b}$,(c) $\widehat{c}$ and (d) $\widehat{d}$ with respect of τ.

are related by a low-pass filtering, we can see that even if their representations are similar, they do not overlap. This shows the complexity introduced by the filtering.

The modeling of phase diagrams's trend by a third degree polynomial is of great interest as it enables to detect if transients are related by a time-scale transformation. However, at this point of the study, there is no method that tells us what couples of lags we should use to highlight this transformation. This is why we moved torward **a matching phase diagram technique** that is presented in the next subsection.

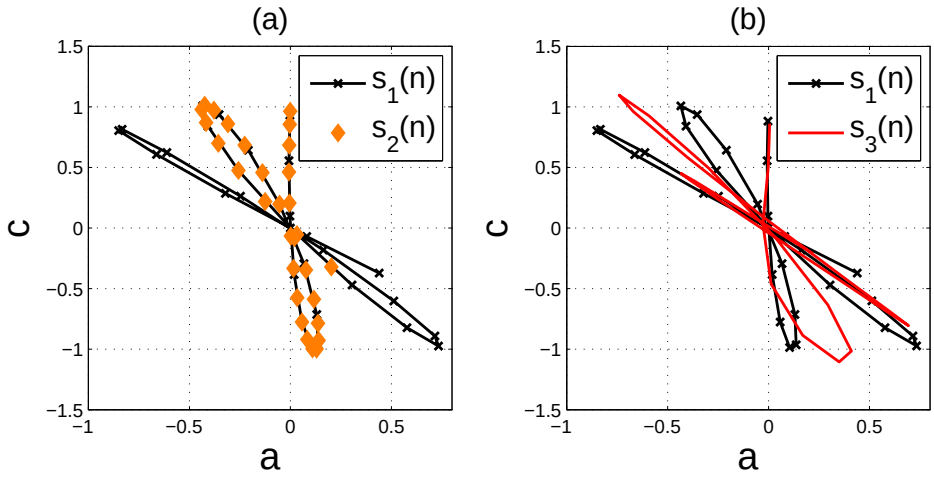

Figure 3.12: Evolution of $\widehat{c}$ with respect to $\widehat{a}$ for the 3 studied signals.

3.2.3 Extremum points / bounding box

Generally, when we talk about SNR for transient analysis, we only consider signal and noise over the duration of the transient. When it comes to noise in phase diagram, we can see in Figure 3.13 that the external contour remains more or less the same depending on the level of noise considered. This is the reason why we focus on the bounding box of the trajectory that is delimited by the maximal and minimal values of the studied signal.

We thus define 4 remarkables coordinates defined as follows and illustrated in Figure 3.14:

$$A: \begin{cases} \forall n, \quad x(n_1) = \underset{n}{max}(x(n)) \\ y(n_1) \end{cases} \tag{3.17}$$

$$B: \begin{cases} x(n_2) \\ \forall n, \quad y(n_2) = \underset{n}{max}(y(n)) \end{cases} \tag{3.18}$$

$$C: \begin{cases} \forall n, \quad x(n_3) = \underset{n}{min}(x(n)) \\ y(n_3) \end{cases} \tag{3.19}$$

$$D: \begin{cases} x(n_4) \\ \forall n, \quad y(n_4) = \underset{n}{min}(y(n)) \end{cases} \tag{3.20}$$

In order to compare two transient signals analysis, we consider the signals' phase space diagrams for different values of lag $[\tau_{1,i}, \tau_{2,i}]_{i\in[1,\ldots,\tau_{max}]}$ and we look for their extremum points $[A_{k,i}, B_{k,i}, C_{k,i}, D_{k,i}]_{k=1,2}$. Then, we compute 4 matrices H_A, H_B, H_C and H_D defined as follows:

$$H_X = \{h_{X,i,j}\}_{i,j\in[1,\ldots,\tau_{max}]} \tag{3.21}$$

$$= \{\mathcal{D}(X_{1,i}, X_{2,j})\} \tag{3.22}$$

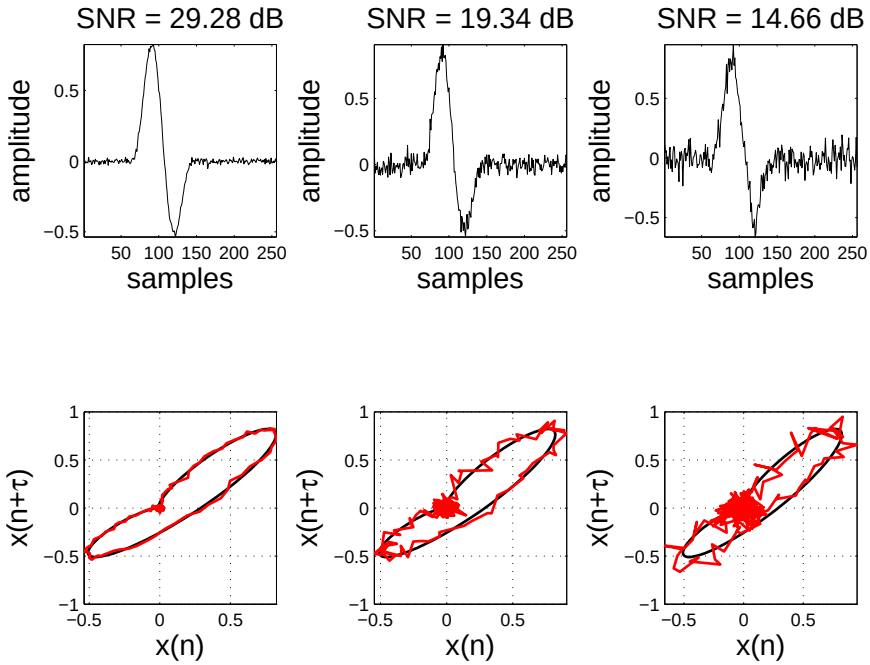

Figure 3.13: Noisy transients and their respective phase diagrams for different level of noise.

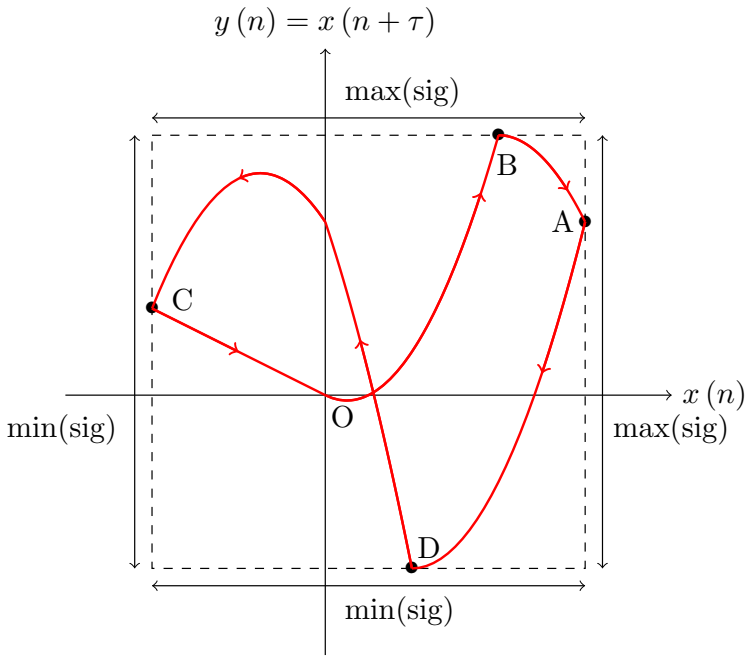

Figure 3.14: Bounding box that confines transient trajectories are delimited by the maximal and minimal values of transients.

where $\mathcal{D}$ describes a given metric and X the extremum point taken into consideration.

Each matrix provides a "map" of the distances between the extremum points of each phase

space diagrams calculated for different values of lags. Therefore, it enables to discover which couples of lags $[\tau_1, \tau_2]$ need to be used to provide a match between two extremum points.

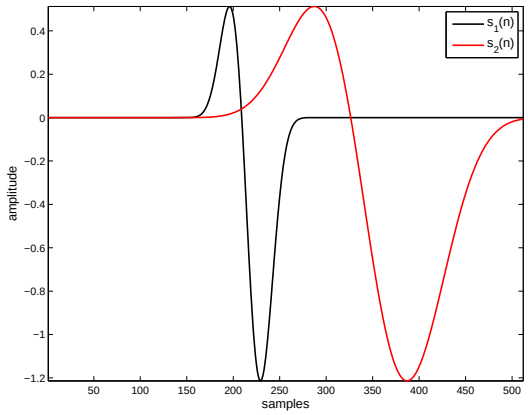

Figure 3.15: Temporal data of the studied signals

In order to illustrate this concept, let consider two transients related by a time-scale transformation with the dilation coefficient $\alpha = 3$. Temporal data presented in Figure 3.15 shows that $s_2(n)$ (in red) is only dilated compared to $s_1(n)$ (in black) and does not suffer amplitude changes. In this part, the purpose is to highlight the time-scale relation between these signals.

We first calculate the 4 matrices described previously using the Euclidean norm $\mathcal{D}_2$ defined as follows:

$$\mathcal{D}_2(x) = \|X_{1,i} - X_{2,j}\|_2 \tag{3.23}$$

Those 4 matrices are displayed in Figure 3.16 with the same colorbar. In this example, we can see that the error is always really small for the extremum point B contrary to the other points. Nevertheless, they all have in common a 'line' representing the set of lags where the error is minimum. Those 'lines' are shown in Figure 3.17 and we can notice that they overlap. They describe the sets of lags $[\tau_1, \tau_2]$ to use that would guaranty a match of the 4 extremum points for the two signals. Thus, we can deduce a relationship between the sets of lags by performing a linear regression. We obtain that:

$$\tau_2 = 3\tau_1 \tag{3.24}$$

which is consistent with the dilation coefficient.

To validate this result, we draw $s_1(n)$ and $s_2(n)$'s phase space diagrams by using the set of lags $[\tau_1 = 3, \tau_2 = 9]$ (Figure 3.18). As a matter of fact both phase space diagrams overlap perfectly.

This technique allows to highlight time-scale transformations. However, even if this technique enables to match extremum points having the same coordinates for certain couples of lags, we need to keep in mind that trajectories can still be different as the other coordinates are not considered. This is why it is interesting to monitor *the area covered by the trajectory in the phase space* which is the subject of the next subsection.

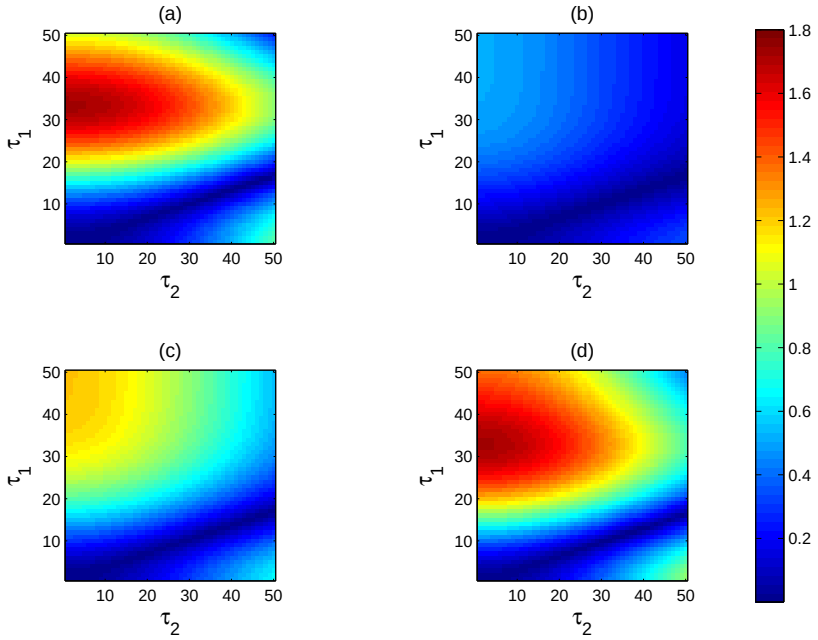

Figure 3.16: The four matrices displaying the distance between extremum points of $s_1(n)$ and $s_2(n)$'s phase space diagrams for different values of lags τ_1 and τ_2: (a) H_A, (b) H_B, (c) H_C and (d) H_D.

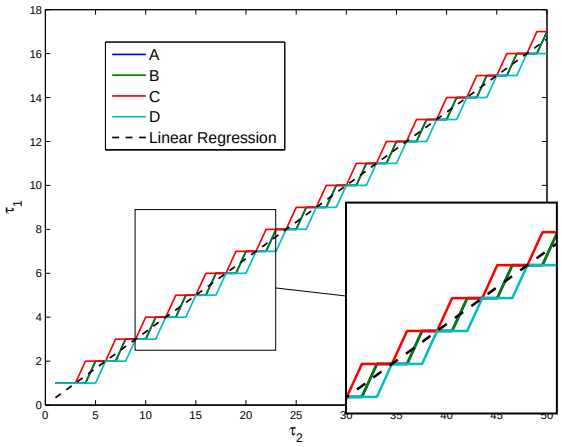

Figure 3.17: Sets of lags $[\tau_1, \tau_2]$ that provide matches for the extremum points.

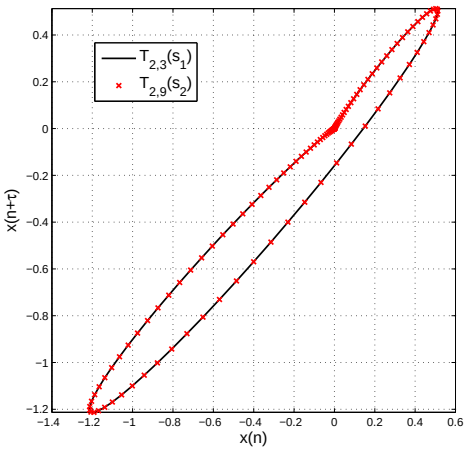

Figure 3.18: Phase space diagrams of $T_{2,2}(s)$ and $T_{2,4}(s_1)$ respectively in black and red.

3.2.4 Area calculation

Previous subsection has shown that it was possible to define four reference coordinates for each phase space diagrams that allow to find matching correspondances, however, it is not enough to guaranty the invariance. The next idea consists in calculating the area of the diagram to quantify the surface. To do so, the diagram is considered as a curve having at each instant n

polar coordinates $[\rho_{\tau_k}(n), \theta_{\tau_k}(n)]$. We then calculate the area $\mathcal{A}[s, \tau_k]$ covered by the phase space diagram calculated for $\tau = \tau_k$:

$$\mathcal{A}[s, \tau_k] = \int_{\theta_{\tau_k}(1)}^{\theta_{\tau_k}(N)} \rho_{\tau_k}^2(n) \left| d\theta_{\tau_k}(n) \right| \tag{3.25}$$

We also define the matrix $A[s_1, s_2]$ defined as follows that enables to calculate the distance bewteen two signals s_1 and s_2's phase space diagram areas computed for different sets of lags $[\tau_1, \tau_2]$:

$$A[s_1, s_2] = \{a_{i,j}\}_{i,j \in [1,\ldots,\tau_{max}]} \tag{3.26}$$

$$= \{|\mathcal{A}[s_1, \tau_i] - \mathcal{A}[s_2, \tau_j]|\} \tag{3.27}$$

It permits to find the sets of lags that offer similar areas for two phase space diagrams. This analysis can be complementary to the bounding box method to highlight time-scale transformation for instance.

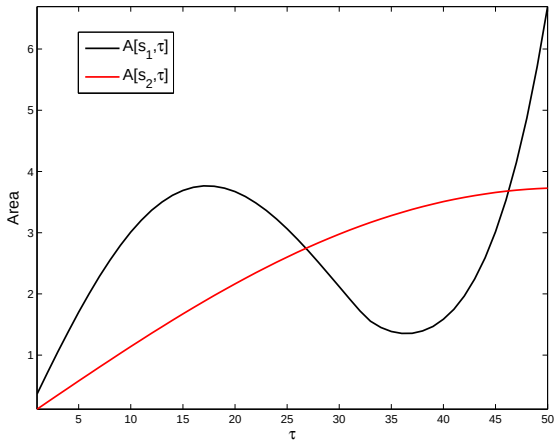

Figure 3.19: Evolution of the two signals 's area according to the lag used to compute their phase space trajectories.

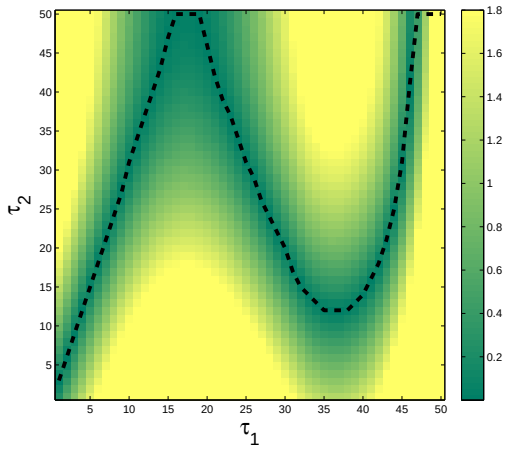

Figure 3.20: The matrix $A[s_1, s_2]$ denables to calculate the distance bewteen two signals s_1 and s_2's phase space diagram areas computed for different sets of lags $[\tau_1, \tau_2]$.

In order to illustrate this concept, let consider the example presented previously that only presents a time-scale transformation. We first compute the area for $s_1(n)$ and $s_2(n)$ using $\tau = 1, \ldots, 50$. The evolution of the area according to the lag is displayed for both signals in Figure 3.19. As we can see, $\mathcal{A}[s_1, \tau]$ presents a clear maxima for $\tau = 17$, while $\mathcal{A}[s_2, \tau]$ does not have one. A maxima notifies a change on phase space diagrams that can as an example change its first eigenvector.

The computation of matrix $A[s_1, s_2]$ provides the sets of lags that offer matching areas. They are highlighted by a black dashed line in Figure 3.20. For $\tau_1 = 1, \ldots, 17$, we can see that this line is also a straight line that verifies the following equation:

$$\tau_2 = 3\tau_1 \tag{3.28}$$

This relationship confirms the dilation coefficient that has been used for the signals simulation.

This method is really usefull when coupled with the bounding box method. They enables to highlight time-scale transformations between signals. This will be illustrated in more details in the Chapter devoted to the applications.

3.2.5 Polar coordinates analysis

General presentation

We have shown in Section 3.1 that amplitude changes can be enlightened from phase space diagrams. Indeed there exists a scale factor between two signals having an amplitude relationship. To highlight it, phase diagrams are turned into polar coordinates as shown in Figure 3.21. The assessment is that for a given polar angle, radius are directly connected by the amplitude coefficient.

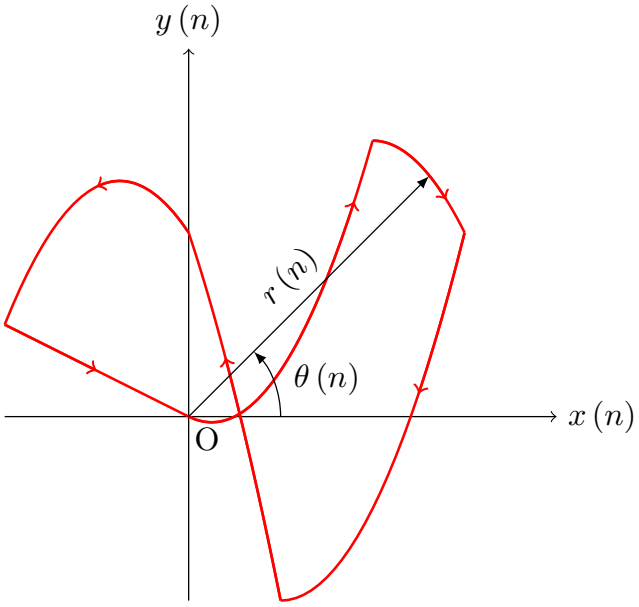

Figure 3.21: Trajectory expressed in polar coordinate system. Each coordinates is represented by a radius and a polar angle.

Let consider $s_1\,(n)$ defined as in Equation C.26 and $s_2\,(n)$ defined as follows:

$$s_2\,(n) = \frac{1}{\beta} s_1\,(\alpha n) \tag{3.29}$$

with $\alpha = 2$ and $\beta = 1.4$, as an example. That is, s_2 is derived from s_1 by a double scale and amplitude modification.

Figure 3.15 and Figure 3.22 present temporal data and phase diagrams obtained for $m = 2$ and respectively $\tau = 8$ and $\tau = 16$. Using this set of parameters, we know that the phase

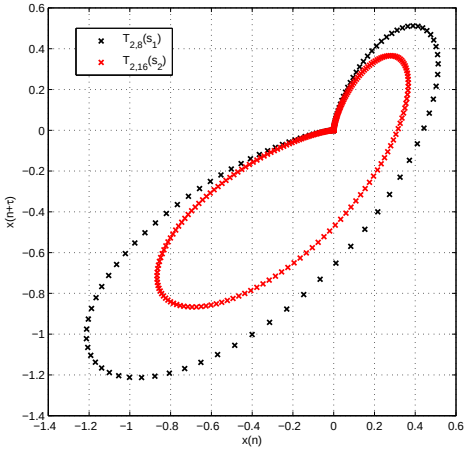

Figure 3.22: Phase space diagrams of $T_{2,2}(s)$ and $T_{2,4}(s_1)$ respectively in black and red

diagrams would be superposed if the signals's amplitudes were identical. However due to this difference they present a shape-invariant scale transformation.

We turn the cartesian coordinates into polar coordinates and draw the functions $\rho(n) = f(\theta(n))$ for the two signals that are shown in Figure 3.23. As we can see, both curves are similar and it is easy to imagine a linear relationship between them. However, for a given polar angle, there is not always a correspondance between the two curves (Figure 3.24). This is the reason why we propose an algorithm to match corresponding coordinates with respect to polar angles.

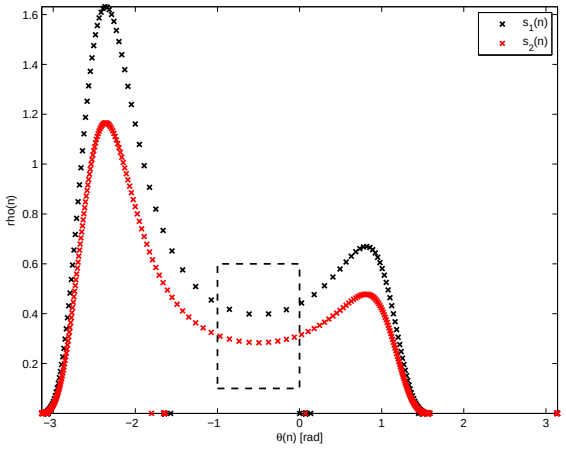

Figure 3.23: $\rho(n) = f(\theta(n))$ for $T_{2,2}(s)$ and $T_{2,4}(s_1)$ respectively in black and red

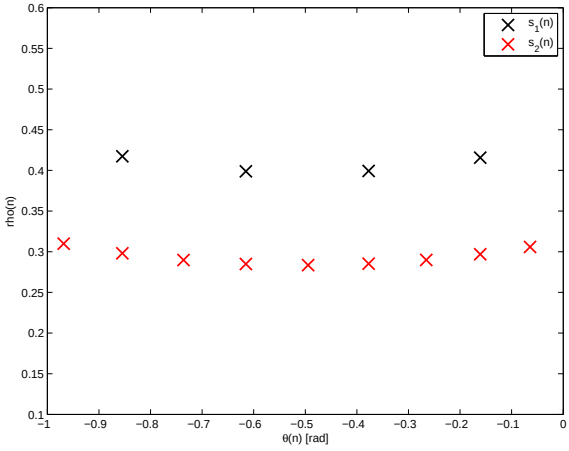

Figure 3.24: Zoom in of Figure 3.23

Algorithm description:

For each polar angle $\theta_1(n)$ of the first curve, the algorithm searches for the corresponding polar angle on the second curve $\theta_2(n)$. A match is enlightened if the two conditions are met:

$$\begin{cases} \theta_2(n_1) & = & argmin\,|\theta_1(n_0) - \theta_2(n)| \\ \theta_2(n_1) & < & \epsilon \end{cases} \tag{3.30}$$

where n_0 is the index of $\theta_1(n)$ we are looking for, n_1 is the corresponding index for $\theta_2(n)$ and ϵ a threshold error that enables to discard certain associations that are not consistent.

The algorithm selects M pairs of coordinates and calculates a ratio $r(i)$ defined for $i \in \{1, \ldots, M\}$ such as:

$$r(i) = \frac{\rho_1(n_{0_i})}{\rho_2(n_{1_i})} \tag{3.31}$$

Figure 3.25 presents the pairs of coordinates that have been selected by the algorithm and the associated ratio. In this example, we can see that the ratio is consistent along the entire polar angles interval which corroborates the idea of a shape-invariant scale transformation. Moreover, the ratio is here equal to 1.4 which is the value of β.

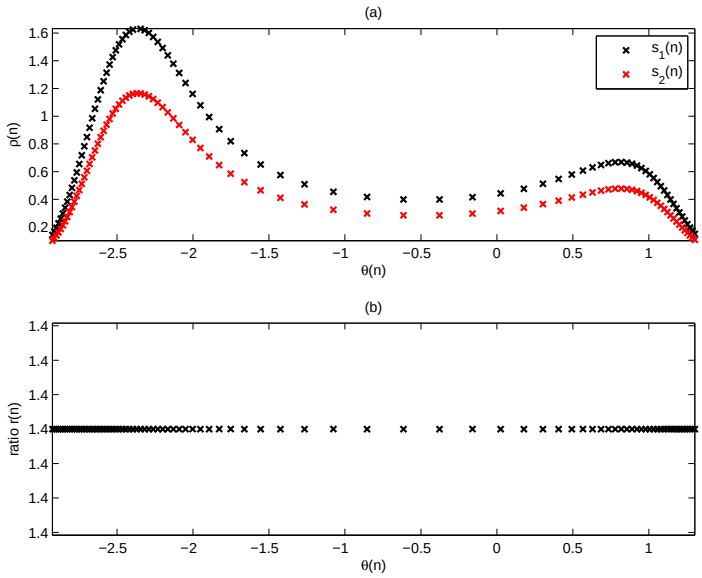

Figure 3.25: (a) Pairs of coordinates that have been selected by the algorithm to calculate the amplitude modification known as $r(n)$ (b)

We have seen in this example that it was possible to estimate a shape-invariant scale transformation. The same work can be done along an interval of polar angles that would highligh amplitudes changes on this interval.

Application to linear modification changes

However, amplitude changes are not uniform in real world and are most of the time more complex. We propose to analyze amplitude changes that can be modeled by a linear function $\alpha(n)$. To do so, we consider two signals $x(n)$ and $y(n)$ defined as follows:

$$y(n) = \alpha(n)\, x(n) \tag{3.32}$$

We then develop $y(n)$'s phase space vector at instant n:

$$[y(n), y(n+\tau)] = [\alpha(n)\, x(n), \alpha(n+\tau)\, x(n+\tau)] \tag{3.33}$$

At this point, no relationship can be extracted from this equation. We need to know more about the linear function $\alpha(n)$ to continue. This is why we focus on the following linear function:

$$\alpha(n) = \beta n + \gamma \tag{3.34}$$

with $\beta, \gamma \in \mathcal{R}^2$. Besides, we note:

$$\begin{cases} X(n) = [x(n), x(n+\tau)] \\ Y(n) = [y(n), y(n+\tau)] \end{cases} \tag{3.35}$$

We then continue to develop Equation 3.33:

$$Y(n) = \alpha(n)\, X(n) + [0, \beta\tau x(n+\tau)] \tag{3.36}$$

Typically, it means that the relationship is conserved but a linear error depending on the studied signal $x(n)$, τ and β appears on the second axis. This error evolves between $\beta\tau \min(x)$ and $\beta\tau \max(x)$, and is illustrated in Figure 3.26.

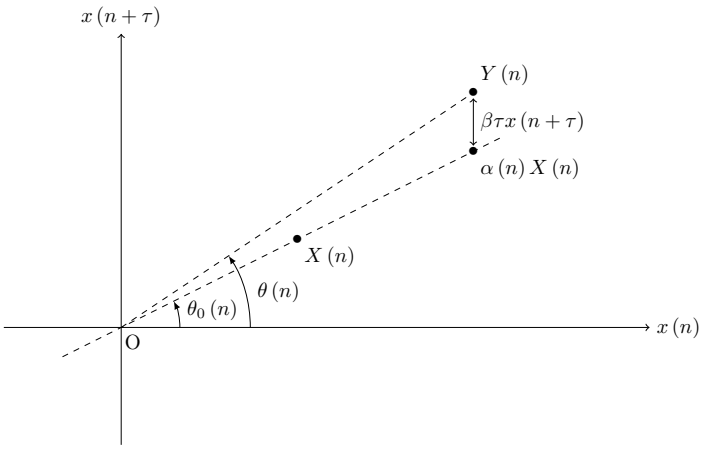

Figure 3.26: Linear error created by a linear amplitude change on 2 signals.

It is quite obvious that the last algorithm cannot be carried out for such signals which leads to the development of another approach. By using the polar coordinates system, the

relationship can be expressed as follows:

$$\begin{cases} X(n) &= \rho_0(n)\exp(\theta_0(n)) \\ Y(n) &= \rho(n)\exp(\theta(n)) \end{cases} \tag{3.37}$$

with $\theta_0(n)$ and $\theta(n)$ the two given polar angles, and the two radius: $\rho_0(n)$ and $\rho(n)$. As shown in Figure 3.26, the polar angles are different.

To illustrate the scenario with an example, we consider two signals presented in Figure 3.27 linked by the black dashed line shown in the same picture. As we can see, the two signals' amplitudes are different, but they do not present a time-scale transformation. We compute their phase diagrams for $m = 2$ and $\tau = 10$, and focus on a particular instant n_0. Figure 3.28 zooms in this particular instant for both signals and we can see that the polar angles are different as predicted by Equation 3.37.

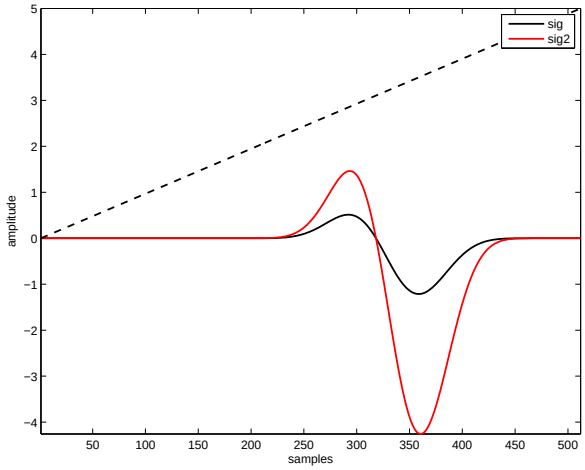

Figure 3.27: Temporal signals whose amplitudes are linked by the dashed black line.

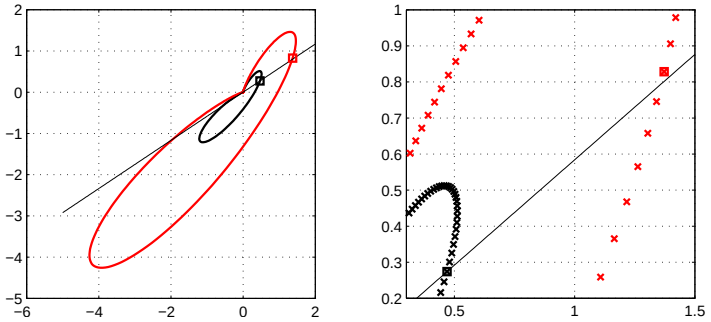

Figure 3.28: Trajectories obtained for $m = 2$ and $\tau = 10$ and zoom in on a particular phase diagram's coordinates that shows the error created by the linear amplitude modification that connects the two studied signals.

Conclusion

We have seen in this subsection that it was easy to highlight shape-invariant scale transformation by looking at the polar coordinates of phase space diagrams. This result can also be extended to reveal amplitude relationships between parts of signals, which is of great interest if the transformation is more complex. However, when dealing with linear amplitude changes, more work need to be done as phase space diagrams connection are more complicated.

Future work will investigate the effects of linear and nonlinear amplitude transformation in phase diagrams in order to detect more complicated relationships.

3.3 Summary

In this Chapter, we have shown in a first part that transients that were connected by time-shifted operator, time-scaling operator and amplitude modification, have invariant (or shape-scaling invariant) phase diagrams if the lags were chosen wisely. We then proposed different methods to extract parsimonious parameters from each representation and combine all of them to highlight the named properties. So far, the methods provided good results for numerical examples and more details are provided in Chapter 4 in the case of real-life data.

Future axis of research can propose to extend this work to higher embedding dimensions. One possible idea could be to apply the same methods to the projections of phase diagrams onto the different planes of the phase space. Extra work also need to be done to explore linear and nonlinear amplitude modifications.

This work has been published at the EUSIPCO conference in 2014, a report has been performed for EDF R& D and the writting of a regular paper is also planed before the end of the PhD.

C. Bernard, T. Petrut, G. Vasile, and C. Ioana. Multi-lag Phase Space Representations for Transient Signals Characterization. In *22nd European Signal Processing Conference EUSIPCO-2014*, September 2014.

C. Bernard, A. Digulescu, and C. Ioana, Multi-lag recurrence plot analysis for transient signal characterization. To appear in 6^{th} *RPA Symposium Proceedings*, Springer (Physics section), 2015, To be submitted.

Chapter 4

Results in applicative contexts

Contents

This chapter presents some applications that show the potential of the proposed approaches to some real-life contexts. We first consider the context of ECG segmentation based on PDA. Then, we propose to characterize electrical transient with multi-lag tools developed in Chapter 3. We also extract characteristics from pressure signals in a passive acoustic configuration and finally, in the last section, we propose to investigate the scenario of active acoustic in underwater configuration.

4.1 ECG segmentation

4.1.1 Introduction

Electrocardiography is the recording of the electrical activity of the heart over a period of time using electrodes placed on a patient chest. These electrodes detect the tiny electrical changes on the skin that arise from the heart muscle depolarizing during each heartbeat. A healthy heart has an orderly progression of depolarization that starts with pacemaker cells in the sinoatrial node, spreads out through the atrium, passes through the atrioventricular node and then spreads throughout the ventricles. This orderly pattern of depolarization gives rise to the characteristic electrocardiogram (ECG) tracing that reflects the cardiac cycle.

The cardiac cycle (Figure 4.1[1]) refers to a complete heartbeat from its generation to the beginning of the next beat, and so includes the diastole, the systole, and the intervening pause. Each beat of the heart involves five major stages. The first two stages, often considered together as the "ventricular filling" stage, involve the movement of blood from the atria into the ventricles. The next three stages involve the movement of blood from the ventricles to the pulmonary artery (in the case of the right ventricle) and the aorta (in the case of the left ventricle).

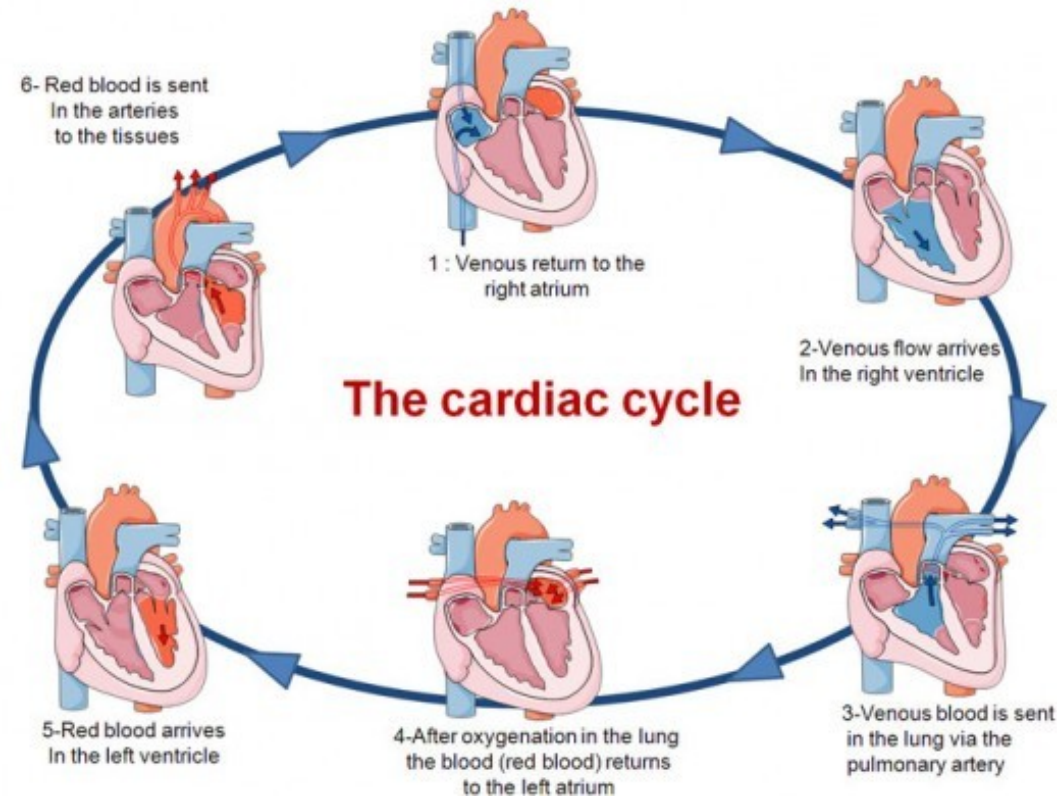

Figure 4.1: Description of the cardiac cycle

[1]The Cardiac Cycle. `www.glogster.com`

The frequency of the cardiac cycle is described by the heart rate, which is typically expressed as beats per minute. An ECG can be used to measure the rate and rhythm of heartbeats, the size and position of the heart chambers, the presence of any damage to the heart muscle cells or conduction system, the effects of cardiac drugs, and the function of implanted pacemakers.

From one patient to another, heartbeat rhythms and features can be different but are nevertheless always characterized by three well-known waves: a P-wave (atrial depolarization), a QRS-complex (ventricular depolarization) and a T-wave (ventricular repolarization) (Figure 4.2). As changes in time-series can reveal heart disease, it is important to identify the different features and extract time-domain characteristics.

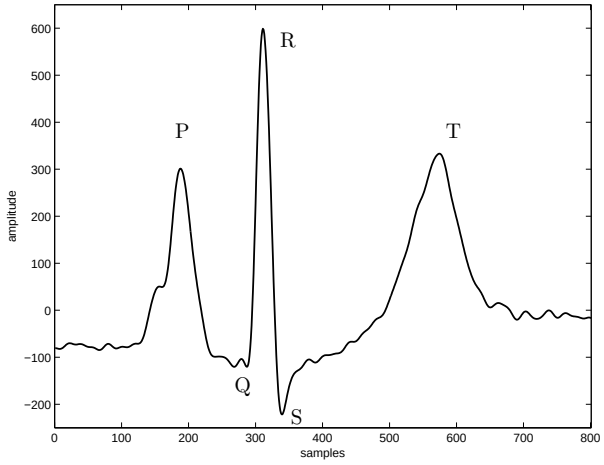

Figure 4.2: A classical heartbeat is composed of three main waves such as P, QRS-complex and T-waves. They are of great interest in cardiac diagnosis.

Many methods have been designed over the past two decades to provide an automatic segmentation of ECG time-series. To identify the different waves, some tried to perform a waveform analysis [dCR03, dCOR04], essentially based on wavelet transforms [MCOS07] and hidden Markov models [LBBC01, GB03, AaDB06, AaB07]. Some tried different approaches by using dynamic time warping [VVV98], the signal decomposition over Hermitian basis functions [AKSA07] or a Bayesian approach [SS09]. However, due to the methodological limitations and the characteristics of nonstationary and nonlinearity of ECG signals, there is no standardized approach for segmenting ECG signals, although, all those techniques mentioned above are practical.

In this Section, we propose a new framework to study ECG time-series that provides a good segmentation and is based on RPA. This work has been conducted during a four-month stay at Ryerson university (Toronto, Canada) under the supervision of Dr. Sridhar Krishnan and Dr. Muhammad Hasan.

4.1.2 Methodology

The proposed segmentation algorithm is divided into three major steps: the pre-processing, the detection algorithm and finally the post-processing. Those three parts are developed in the next subsections.

Pre-processing

The pre-processing step consists of a low-pass filtering followed by a median filtering. The first filtering is applied to remove the fast variations of the signal that are due to noise. The second filtering is used to estimate and then remove the continuous component of the signal that corresponds to a possible variation of the signal baseline. An important variation of the baseline can be a problem as the detection algorithm takes into consideration the extremum values of the time-series. Figure 4.3 shows an ECG time-series having an important variation of its baseline. This one is estimated with the median filtering and then removed from the original signal in order to obtain the filtered signal $s_{filt}(n)$.

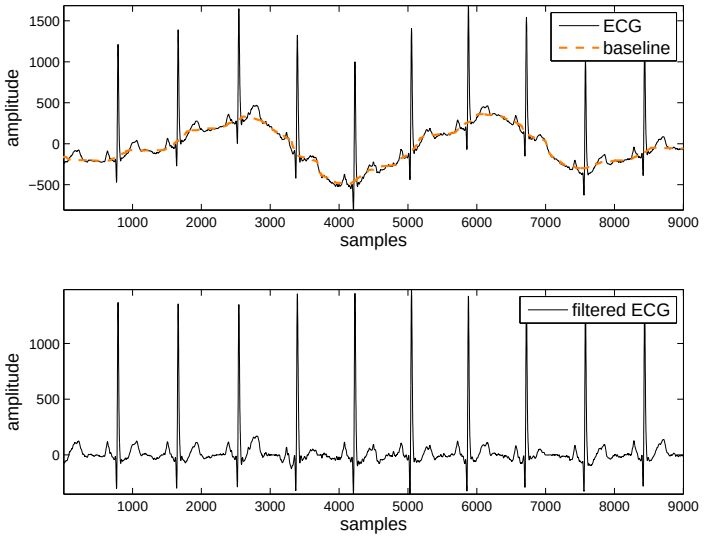

Figure 4.3: (a) Original ECG time-series having an important variation of its baseline (in orange). (b) Filtered ECG time-series.

Detection algorithm

The detection algorithm is based on the spatial-embedding process that enables us to express parts of the signal $s(n)$ defined for $n \in \{1, \ldots, N\}$ as vectors. At instant n, those are defined as follows:

$$\overrightarrow{v_n}[s, K, m] = [s(n), s(n+K), \ldots, s(n+(m-1)K)] \tag{4.1}$$

with m the embedding dimension (the vector dimension) and K the integer decimation factor.

As an example, at instant n_0, the algorithm only considers $s(n)$ samples for $n \in [n_0, n_0 + (m-1)K]$, and then keeps every K samples.

First, let define the following three parameters:

- A_{max} the maximum amplitude of the studied time-series.
- $a(n)$ the maximum amplitude between two successive vectors defined as:

$$a(n) = max\left(\overrightarrow{v_{n+1}}[s, K, m]\right) - min\left(\overrightarrow{v_n}[s, K, m]\right) \tag{4.2}$$

- $r \in [0, 1]$ a ratio

The method is designed to detect sudden changes in amplitude in the time-series. By sudden, we refer to a difference of amplitude between two successive vectors that is bigger than a data-related threshold rA_{max} that can be chosen by the user. Therefore, at each instant n, a detection is enlightened if the maximum amplitude between two successive vectors $a(n)$ is bigger than rA_{max}. The result of the detection is then stored in a binary vector D defined as:

$$D(n) = \begin{cases} 1 & if \quad a(n) > rA_{max} \\ 0 & otherwise \end{cases} \tag{4.3}$$

where, 1 stands for a detection and 0 for the opposite.

In the case of ECG time series, the method is not good enough to detect all the different waves of the heartbeat at once because their shapes and duration are quite different: QRS-complex are short and very sharp, while P and T-waves have a longer duration and their slope are more gentle. Thus, the algorithm is used twice, both using $K = 1$, because, undersampling is not necessary in this scenario. It is first applied to the filtered signal $s_{filt}(n)$ to detect the sharp and fast QRS-complex peaks by using a small value of m. Figure 4.4 presents the first results obtained for the QRS complex. As we can see in Figure 4.4(b) and (c), QRS-complex are not the only peaks that are detected; there are also over and under detections that need to be taken care of. Therefore, a closing procedure has been elaborated that first merges detections that are separated by less than N_{dil} samples, and then removes detections that are smaller than N_{ero}. Figure 4.4(d) shows the final detection obtained with the closing procedure. The binary detection result is stored in D_1.

Then, because QRS-complex amplitudes are more important than the other P and T-waves that need to be segmented, they need to be removed from the current time-series. Hence, D_1 is divided into segments corresponding to the continuous detections and for each of them, the corresponding time-series samples are replaced by a data-related constant value depending on the minimum and maximum signal values. The new time-serie obtained is $s_{mod}(n)$ and is represented in Figure 4.5.

Afterwards, the algorithm is used a second time on the new time-serie to obtain the binary vector D_2 that detects P and T-waves. Due to their longer durations, the paramater m need

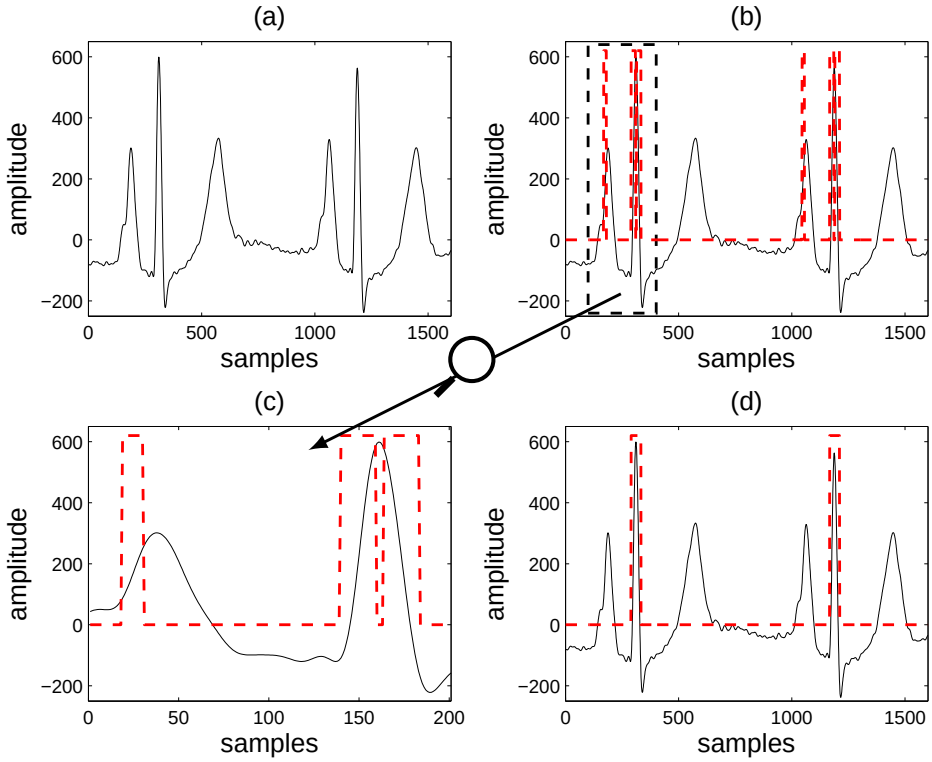

Figure 4.4: (a) ECG time series, (b) First detection obtained in red with the classical method, (c) zoom in a part of the time series, (d) Final detection after the closing procedure.

to be larger. Subsequently, a post-processing algorithm has been carried out to surpervise the final results which is elaborated in the following subsection.

Parameters m and K are chosen by trials and error. More work is needed to automatize the process, which is one of the perspectives in this domain.

Post-processing

As the first detection D_1 usually provides really good results, the binary vector is considered as a reference for the post-processing algorithm. Generally, between two QRS-complex, there are always a single P and T-waves. Therefore, between two successive D_1 positive detections, we should only have two intervals of D_2 detection corresponding to those waves. Thus, we then define windows of length $L(k)$ defined as the intervals between two succesive D_1 detections, that we divide into two equal parts: the left and right. For each half interval, two criteria are needed to validate the detection:

- only one interval of detection is allowed (corresponding to a P or a T-wave),
- the absolute maximum value has to be part of the detection segment.

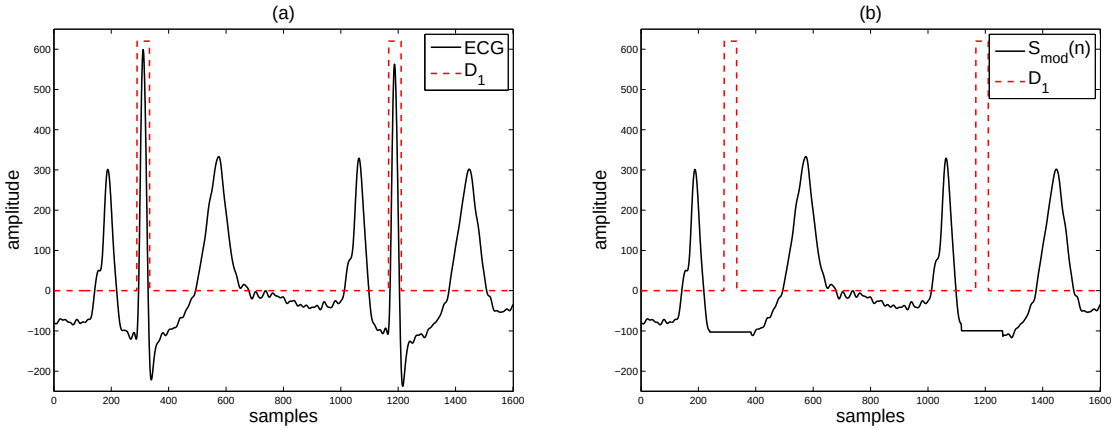

Figure 4.5: (a)Superposition of the ECG time series and the QRS detection D_1, (b) Superposition of $s_{mod}(n)$ and the QRS detection D_1.

This separation into two equal segments has been done in an empirical manner. Figure 4.6 shows the results of a good segmentation on two successive heartbeats and the intervals considered for the post-processing program.

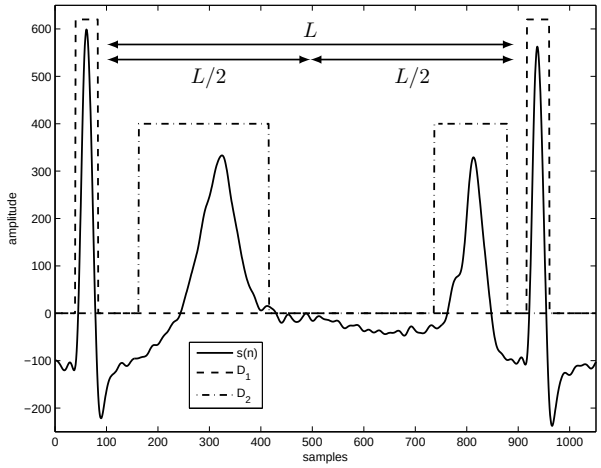

Figure 4.6: An interval between two successive QRS-complex. Two parts are identified and used independently by the post processing algorithm.

In the case of overdetection, meaning that there are more than one detection in one half interval, a closing morphological procedure has been elaborated. This procedure allows to unify two consecutive detections that are separated by a small number of samples and also to delete detections too small to be significant. However, because sometimes it is not enough, the algorithm only allows detections that verify the previous mentioned conditions.

In the case of underdetection (meaning that the algorithm only provides one or zero detections between two consecutives QRS-complex), the segmentation algorithm is used once again on the considered segment with another value of m (usually smaller).

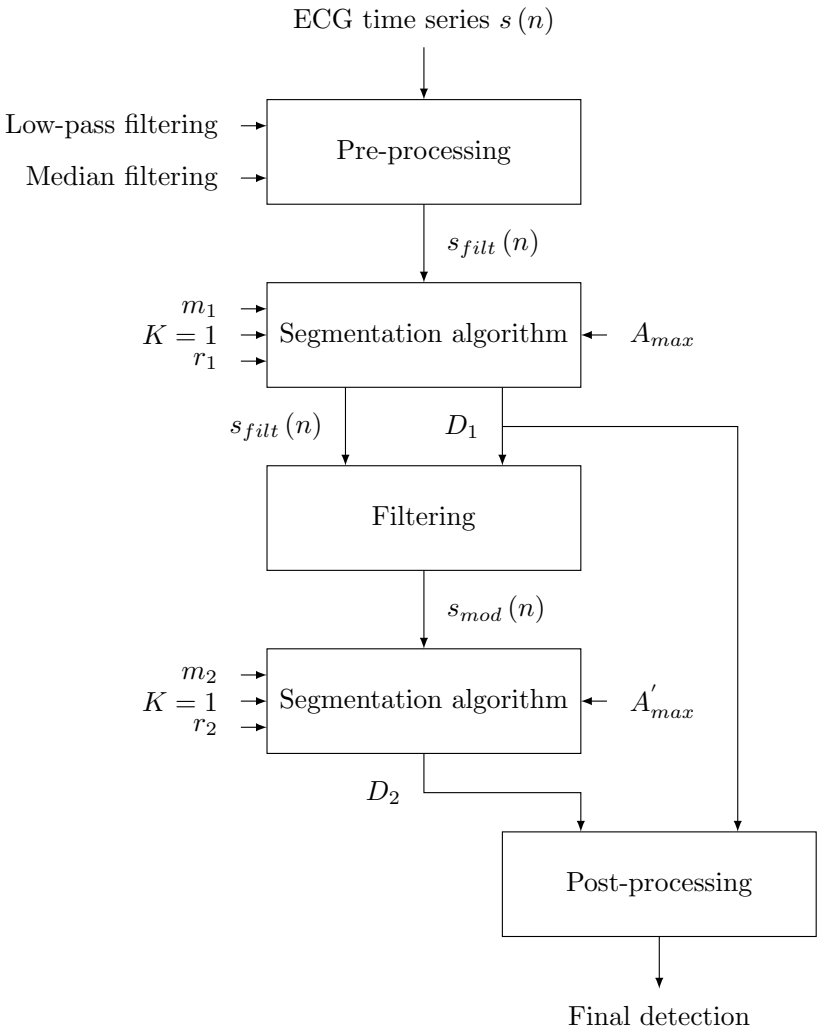

Figure 4.7: Proposed segmentation algorithm based on 2-steps segmentation in RPA domain.

The full process of proposed algorithm has been summarized in Figure 4.7.

4.1.3 Real data processing

4.1.3.1 Presentation of the database

The algorithm has been tested on a real database elaborated by Boston's Beth Israel Hospital and the MIT. The MIT-BIH Arrhythmia database is composed of 48 half-hour excerpts of two-channel ambulatory ECG recordings obtained from 47 subjects between 1975 and 1979.

The recordings were digitized at 360 samples per second per channel with 11-bit resolution over a 10mV range. Two or more cardiologists independently annotated each record. More details about the database can be found in [Phy] and [GAG+00].

This database is famous in ECG processing comunity and is used by many researchers to conduct their works. Nevertheless, there exists one big limitation: there is no ground truth available to confirm that the proposed segmentation is of good quality. During my stay in Toronto, we developed a reference document that provides the sample index of each QRS-complex for this database. It enables us to quantify our results for the QRS-complex segmentation.

4.1.3.2 Tools to quantify the results

To quantify the results of the 'X-wave' detection by the algorithm, four statistical parameters are evaluated [BGZF01]:

$$S_e = \frac{TP}{TP + FN} \tag{4.4}$$

$$+P = \frac{TP}{TP + FP} \tag{4.5}$$

$$F1 = \frac{2TP}{2TP + FP + FN} \tag{4.6}$$

$$DER = \frac{FP + FN}{Total\ number\ of\ X - waves} \tag{4.7}$$

where TP is the number of true positives (an actual X-wave is detected), FP is the number of false positives (a wave is detected but does not correspond to a X-wave) and FN is the number of false negatives (an actual X-wave is not detected by the algorithm). The notation is explained in Figure 4.8.

	$X = 0$	$X = 1$
$\widehat{X} = 0$		FN False Negative
$\widehat{X} = 1$	FP False Positive	TP True Positive

Figure 4.8: This Table summarizes the different statistical terms used in this Section. X refers to the presence of a X-wave, while $\widehat{X}$ refers to the estimation given by the segmentation algorithm

The sensitivity S_e provides the percentage of true X-waves detected over the total number of detections. The positive predictivity $+P$ refers to the confidence level of the results. The detection error rate (DER) enables to quantify the precision of the segmentation and the $F1$ score is the harmonic mean of precision and sensitivity [Pow11, Faw06].

4.1.3.3 Presentation of the results

Pre-processing

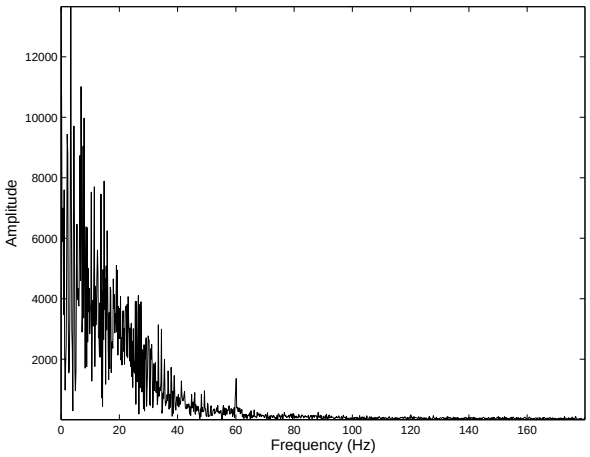

Figure 4.9: Spectrum of an ECG time-series.

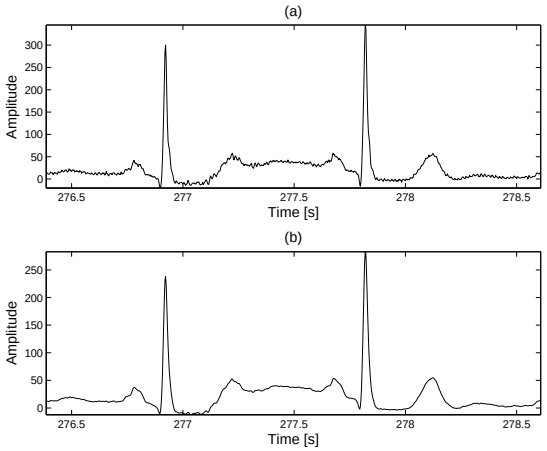

Figure 4.10: ECG time-series before (a) and after (b) the low-pass filtering. The signal has been smoothen.

Generally, the frequency content of an ECG time-series is comprised between 0 and 50 Hz (Figure 4.9). In order to remove all the tiny fluctuations that correspond to measurement noise, we choose to use a 6^{th} order low pass filter at the cutoff frequency of 18Hz. As the low-pass filter is not selective, it will only remove the noise and smooth the signal (Figure 4.10).

The median filtering is composed of 100 samples which is in order with the length of the P and T-waves duration. It needs to be of the same magnitude in order to estimate the general baseline and to not remove at the same time the waves of interest. Figure 4.11 shows the estimation of the baseline of an ECG time-series and its removal. The obtained baseline is smooth and the waves of interest are still in place.

QRS-complex detection

As mentionned in the previous subsection, the first step of the method is to detect all the QRS-complex that are in the studied time-series but the main issue is to choose what parameters are the best suited for this purpose. We know that they are usually composed of 20 samples in average in this database: this is why, we decide to run the algorithm for different values of embedding dimension: $m = \{5, 10, 20\}$ in order to choose which dimension provides the best results. If the detection intervals are composed of less than 10 samples, then they are too short to correspond to actual QRS-complex: we set $N_{ero} = 10$. The next criteria to set are the ratio r_1 and N_{dil}: the experiments are run for several values defined as $N_{dil} = \{10, 20, 30\}$ and $r_1 = \{5\%, 10\%, 20\%\}$.

The first experiment consists in running the detection algorithm with or without the closing

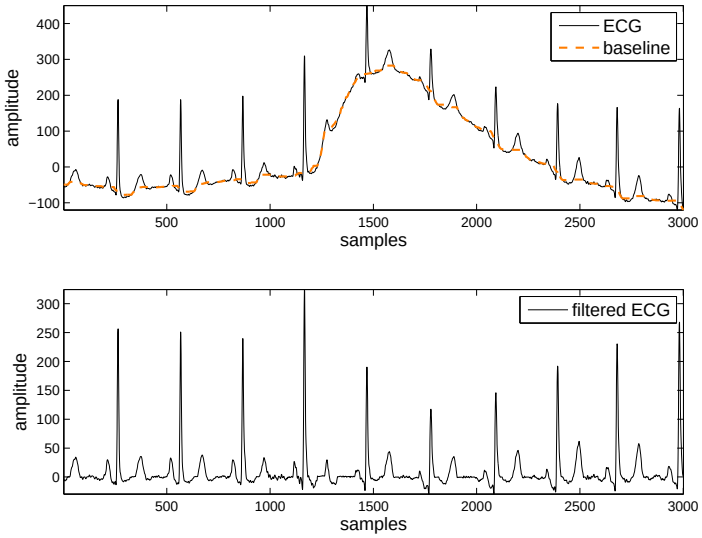

Figure 4.11: (a) Zoom in an original ECG time-series having an important variation of its baseline (in orange). (b) Filtered ECG time-series after the median filtering.

procedure, it provides binary vectors that gives a certain amount of detection intervals. Each of them is then compared with its corresponding ground truth vector. We here only check if the QRS-complex maxima samples indexes are included in detection intervals. We then tally up the total numbers of true detections (TP), false detections (FP) and false negatives (FN) and calculate the different statistical parameters presented in subsection 4.1.3.2. Appendix B presents an example of one of these experiments.

For each set of parameters, we then sum up the test results for the entire database, and compute the sensitivity, the specificity, the F1 score and the detection error rate. Results are presented in Tables 4.1, 4.2 and 4.3. The results entitled "raw data" correspond to the algorithm used without the closing procedure.

As we can see, the algorithm without the closing procedure leads to results having detection error rates over 100% and F1 scores below 50%. Those results reflect a huge number of errors and a very bad precision that justify the elaboration of the closing procedure. Generally, we can also notice that for $m = \{5, 10\}$, the ratio $r_1 = 0.20$ provides poor performances compared to the other two ratios. However, this result changes for $m = 20$. Apparently, there is a trade-off between the embedding dimension and the ratio: the bigger the embedding dimension, the bigger the ratio that need to be used. Nevertheless, for the three considered embedding dimensions, we identify three sets of parameters that offer the best performances (highlighted in the differents tables) and we choose the best of them that provides a $F1$ score of 95,98% and a DER of 7.84%. It is obtained for the following set of parameters:

$$\begin{cases} m &= 10 \\ r_1 &= 0.1 \\ N_{dil} &= 30 \end{cases} \tag{4.8}$$

	Case	Beats	TP	FN	FP	S_e (%)	$+P$ (%)	$F1$ (%)	DER (%)
Raw data	(a)	112647	59763	186072	52884	24.31	53.05	33.34	212.13
	(b)	112647	24827	167320	87820	12.92	22.04	16.29	226.50
	(c)	112647	2190	104782	110457	2.05	1.94	1.99	191.07
$N_{dil} = 30$	(a)	112647	103899	2994	8748	97.20	92.23	94.65	10.42
	(b)	112647	75611	558	35160	99.27	68.26	80.89	31.71
	(c)	112647	26489	167320	56384	99.85	31.96	48.43	50.09
$N_{dil} = 20$	(a)	112647	101039	4434	11608	95.80	89.70	92.65	14.24
	(b)	112647	74930	694	35841	99.08	67.64	80.40	32.43
	(c)	112647	26326	49	54012	99.81	32.77	49.34	47.99
$N_{dil} = 10$	(a)	112647	95289	7740	17358	92.49	84.59	88.36	22.28
	(b)	112647	71602	1481	39169	97.97	64.64	77.89	36.09
	(c)	112647	25024	43	49477	99.83	33.59	50.27	43.96

Table 4.1: Results obtained for the QRS-complex detection for $m = 5$, the different values of N_{dil} and r_1 equal to: (a) 5%, (b) 10% and (c) 20%

	Case	Beats	TP	FN	FP	S_e (%)	$+P$ (%)	$F1$ (%)	DER (%)
Raw data	(a)	112647	100621	132038	12026	43.25	89.32	58.28	127.89
	(b)	112647	77193	86854	35454	47.06	68.53	55.80	108.58
	(c)	112647	39224	97903	73423	28.60	34.82	31.41	152.09
$N_{dil} = 30$	(a)	112647	109533	12171	3114	90.00	97.24	93.48	13.57
	(b)	112647	105669	1154	6978	98.92	93.81	96.29	7.22
	(c)	112647	76008	86854	32630	99.18	69.96	82.05	29.52
$N_{dil} = 20$	(a)	112647	109435	14549	3212	88.27	97.15	92.49	15.77
	(b)	112647	104485	1835	8162	98.27	92.75	95.43	8.87
	(c)	112647	75755	646	32883	99.15	69.73	81.88	29.76
$N_{dil} = 10$	(a)	112647	108997	22196	3650	83.08	96.76	89.40	22.94
	(b)	112647	101581	4467	11066	95.79	90.18	92.90	13.79
	(c)	112647	71790	1318	36848	98.20	66.08	79.00	33.88

Table 4.2: Results obtained for the QRS-complex detection for $m = 10$, the different values of N_{dil} and r_1 equal to: (a) 5%, (b) 10% and (c) 20%

	Case	Beats	TP	FN	FP	S_e (%)	$+P$ (%)	$F1$ (%)	DER (%)
Raw data	(a)	112647	110021	177324	2626	38.29	97.67	55.01	159.75
	(b)	112647	107049	48020	5598	69.03	95.03	79.97	47.60
	(c)	112647	87074	36557	25573	70.43	77.30	73.70	55.15
$N_{dil} = 30$	(a)	112647	110362	35409	2285	75.71	97.97	85.41	33.46
	(b)	112647	108945	9268	3702	92.16	96.71	94.38	11.51
	(c)	112647	94549	48020	16222	96.95	85.36	90.78	17.04
$N_{dil} = 20$	(a)	112647	110279	46742	2368	70.23	97.90	81.79	43.60
	(b)	112647	108901	10039	3746	91.56	96.67	94.05	12.24
	(c)	112647	94208	3213	16563	96.70	85.05	90.50	17.56
$N_{dil} = 10$	(a)	112647	110120	77594	2527	58.66	97.76	73.33	71.13
	(b)	112647	108470	13995	4177	88.57	96.29	92.27	16.13
	(c)	112647	93004	4774	17767	95.12	83.96	89.19	20.01

Table 4.3: Results obtained for the QRS-complex detection for $m = 20$, the different values of N_{dil} and r_1 equal to: (a) 5%, (b) 10% and (c) 20%

Detailled results computed with this set of parameters is presented in Appendix B. We can notice that the sensitivity is really good for most of the signals (around 99 %) except for 4 of them (*108m*, *113m*, *114m* and *201m*) that have a sensitivity below 95%. False negative and false positive detections usually correspond to repeated errors that are due to the shape specifity of the heartbeat. As an example, for signal *113m*, the repeated false positive error corresponds to the detection of a portion of the T-wave (Figure 4.12). For signal *201m*, the modification of the QRS-complex's shape leads to a false negative detection as the corresponding QRS-complex sample index is not included in the detection interval and is localized 1 or 2 samples before it (Figure 4.13). What we can say about those errors is that they could easily be taken care of by adjusting the parameters of the algorithm and they correspond to repeated errors that explain their high numbers when they exist.

QRS detector	Beats	TP	FN	FP	S_e (%)	$+P$ (%)
Our work	112647	105669	1154	6978	98.92	93.81
Ghaffari et al.	110159	109837	120	322	99.91	99.72
Li et al.	104182	104070	112	65	99.89	99.94
Martínez et al.	109428	109208	153	220	99.8	99.86

Table 4.4: QRS-complex segmentation results and comparison with other techniques

We now compare our results with those obtained by [GGG08], [MAO+04] and [LZT95]. The detection methods used are based on adaptive wavelet transforms. Results are shown in Table 4.4. Generally, we can notice that their results seem to be better than ours. However, as we have pointed out previously the errors that were made can be fixed by adjusting the algorithm parameters and therefore the results could sensibly be improved. Moreover, their works rely on the choice of a mother wavelet that need to be close to the waves they want to detect, while our method do not need a reference shape. One possible approach to improve our results could be to design a data-driven threshold that could adapt itself to the section of

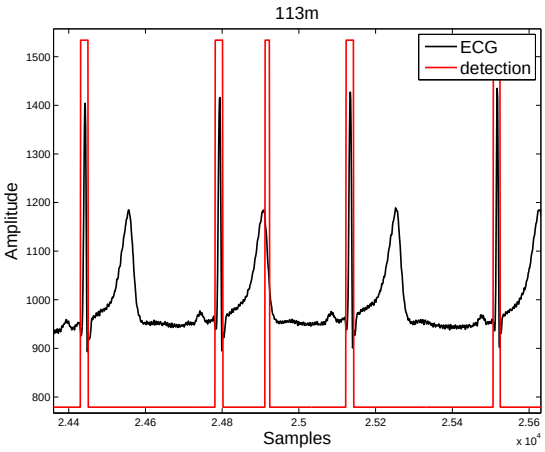

Figure 4.12: The algorithm detects a part of a T-wave: this is a false positive error that can be removed by adjusting the parameters of the algorithm.

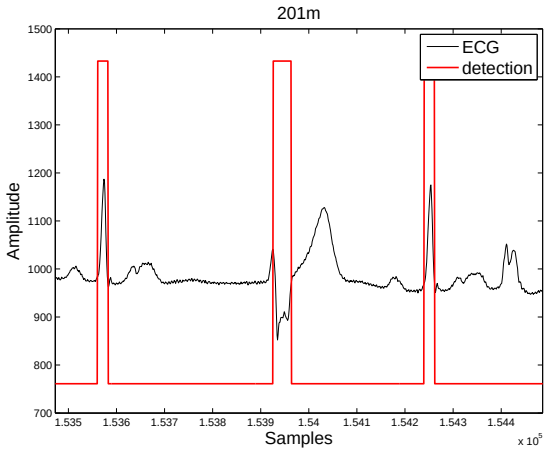

Figure 4.13: The modification of the QRS-complex's shape leads to a detection by the algorithm that does not include the corresponding QRS-complex sample index (localized 1 or 2 samples before it): it is detected as a false negative.

Beats	N_{init}	N_P	N_T	N_{PT}	% P-waves	% T-waves
112647	121573	61239	26572	87811	54.36	23.59

Table 4.5: Results obtained for P and T-waves detection for $m = 30$, $N_{dil} = 20$, $N_{ero} = 10$ and $r_2 = 5\%$.

the signal that is studied just like a window with the short time Fourier transform.

P and T-waves detections

It was difficult to conduct the same experiment for P and T-waves detections due to the lack of ground truth, nevertheless we ran the algorithm. To quantify the results, we tally up the number of P and T-waves detected if they verify the two conditions described in the previous subsection. Therefore, we need to keep in mind that those results do not guaranty that the proposed segmentation is truthworthy, only that they verify the conditions.

Results are obtained by using $m = 30$, $N_{ero} = 10$ (detection intervals that are smaller do not correspond to actual P or T-waves), $r_2 = 5\%$ and $N_{dil} = 30$ and displayed in Appendix B. Summarized results are presented in Table 4.5 and given as follows. After the QRS detection, the detection algorithm is used with the proposed parameters and we tally up the number of supposed P and T-waves detected N_{init}. Then, the post processing algorithm is run and provides the number of P-waves N_P and T-waves N_T. We note N_{PT} the sum of detected waves. Typically, we are supposed to obtain more or less as many P and T-waves as QRS complex.

As we can see in Table 4.5, results are not as good as those obtained for the QRS-complex

detection as the percentages of P and T-waves detected do not go up to 55%. However, we need to take a step back and look at the results diplayed in Appendix B.2 that contrast those results. As we can see, for 8 subjects there are almost no detections, for 50% only one of the wave is detected, and finally for 4 of them the detections go up to 98%. It only means that there are still more work to be done to design a data-driven algorithm that can detect P and T-waves with more accuracy.

4.1.4 Conclusion

In this Section, we have developed a new framework for segmenting ECG time-series using PDA. Although, it provides really good results for QRS-complex detections, it should be noted that P and T-waves detections highly depend on the performances of the first detection. The results were then compared to other works found in the literature and are encourageous. It then leads to the calculation of other physical parameters (such as QT intervals [HAB12] [HAB13] for example) that are of great interest to doctors that can then identify heart diseases and malformations. Nevertheless, more work need to be done to improve the results and design a data-driven algorithm.

This work led to the writting of a conference paper that will be submitted in September 2015:

C. Bernard, C. Ioana, M. A. Hasan, and S. Krishnan. Spatial-embedding signal processing for recurrent time series: a case study with ECG signal. In 15^{th} *IEEE Symposium on Signal Processing and Information Technology*, December 2015, to be submitted.

4.2 Electrical transient characterization

4.2.1 Introduction

Electrical transients that are produced in electrical equipments traduce different phenomena that require to be monitored, contributing to ensure the predictive surveillance of systems. Electrical transients can be normal, created by phenomena such as commuting, parameters charge changes; but also abnormal, created by the material problems such as dielectric problems or conductors defaults. The effects such as partial discharges (PD) or electrical arches generate transient signals that need to be continuously studied (detection and characterization) in order to ensure the system safe performing.

PD corresponds to a localised dielectric breakdown of a small portion of a solid or a fluid electrical insulation system under high voltage stress, which does not bridge the space between two conductors. They are usually not visible and can occur in gaseous, liquid or solid insulating medium. They represent one of the most common breakdown in electrical systems and 30% of them would be caused by insulation problems. Their appearance is unpredictable,

really sudden and covers a large bandwidth. All these features make them really difficult to predict, to localize and to characterize. [Got10] developed in his thesis localization methods based on RPA and GCD. Next step was to characterize them, knowing that at the receiving level transients do not only represent the transient at the origin but also the propagation effect. In this context, we propose to apply multi-lag phase diagrams approaches to signals recorded after propagation of a generated PD in lab conditions. Therefore, next subsection is dedicated to the description of the experiment.

4.2.2 Experimental presentation

In order to characterize transient modifications due to its propagation through a medium, we now conduct an experiment using the facilities existing in our lab. We generate a partial discharge (PD) on an electric cable whose ends T_1 and T_2 are connected to a data acquisition system. The PD source is respectively localized at L_1 and L_2 distances from the recording devices. The experimental outline is presented in Figure 4.14 and a photo of the experimental facility is also presented in Figure 4.15. L_1 is composed of two cable reels (152 m in length each) while L_2 is composed of five. At the intersection between the two cables, a PD is generated and we record the signals at both extremities after propagation.

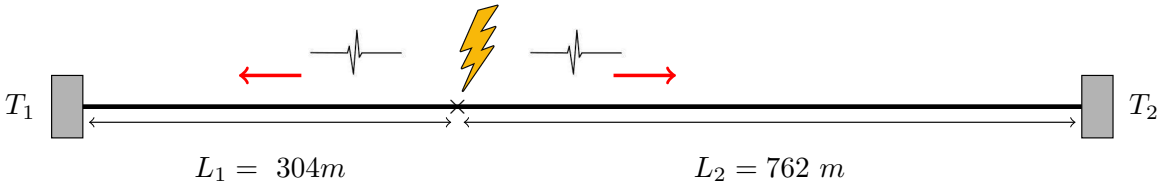

Figure 4.14: Experimental outline

We note $s_0(n)$ the generated PD, $s_1(n)$ the signal recorded at T_1 and $s_2(n)$ the signal recorded at T_2.

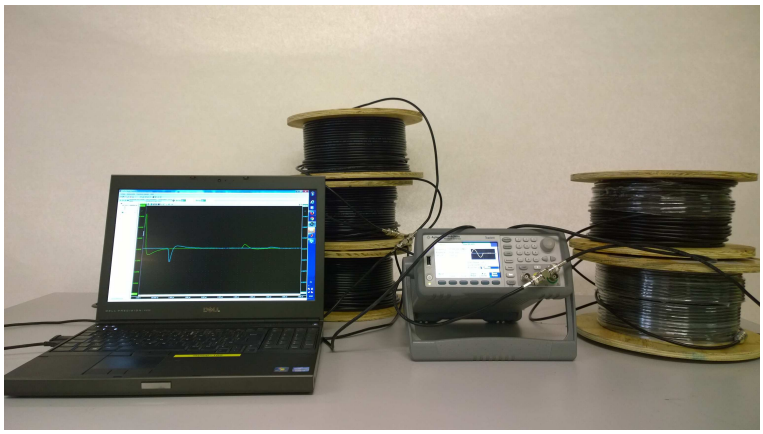

Figure 4.15: Experimental set up

Time representation of emmitted and recorded signals are presented in Figure 4.16. As we

can notice, signals recorded after propagation through the cable reels differ from the emitted one due to the propagation through the medium. They present nonlinear dilation and amplitude changes that are more or less stronger depending on the propagation range. Temporal changes are shown in Figure 4.17 where studied signals have been superposed and normalized.

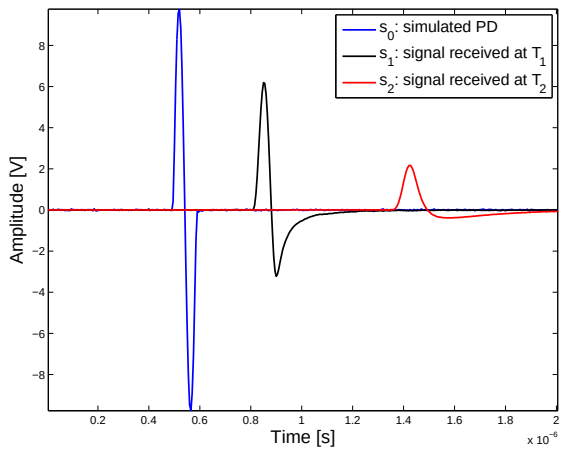

Figure 4.16: Time representation of emmitted signal and recorded signals after propagation through the cable reels.

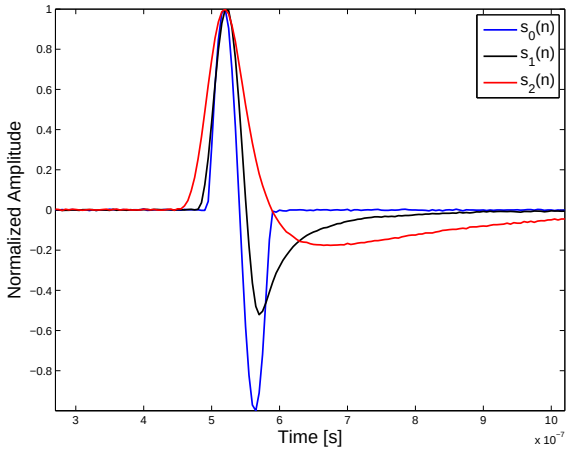

Figure 4.17: Time representation of the superporsition of normalized signals that highligths dilation and amplitude changes.

What is interesting with this kind of signals is that we can easily visualize that a time-scale analysis would not be enough to characterize the modifications caused by the propagation. There are dilation and also a modification of the envelop of the signal that would be difficult to analyze with a single type of mother wavelet function. This is shown by Figure 4.18 where a time-scale study is performed for the three signals using two different mother wavelets: Symlet and Coiflet. The results highly depend on the choice of mother wavelet used and for the three cases, even if it is easy to detect them, it is quite difficult to claim that they come from the same source.

In this subsection, we have presented the experiment and the acquired data. We have shown that time-scale analysis would not provide results that enables a good characterization as waveforms changes with the propagation. This is the reason why it is usefull to move forward MLPDA which is presented in the next subsection.

4.2.3 Data processing

In this subsection, we use the MLPDA tools to characterize the experiental data. We estimate a time-scale transformation with the bounding box, and then study the amplitude relationship that eventually exists between the two signals recording at both extremities.

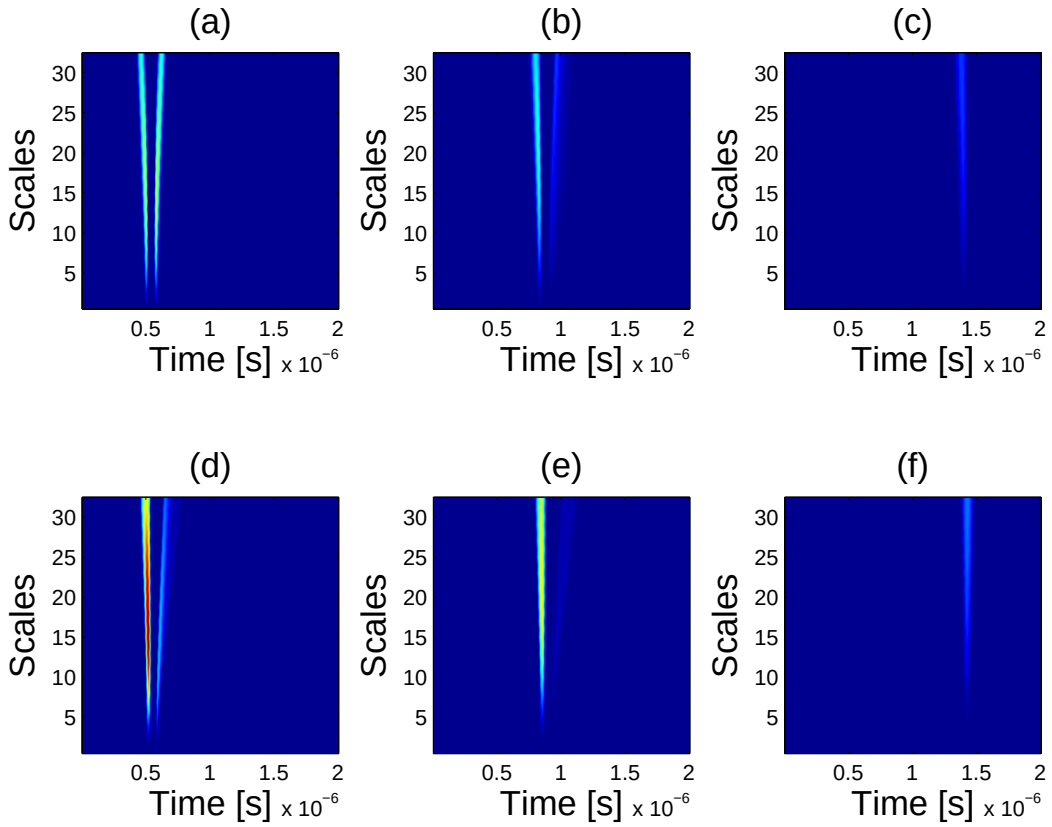

Figure 4.18: Time-scale study using the symlet mother wavelet for (a) $s_0(n)$, (b) $s_1(n)$ and (c) $s_2(n)$. Time scale study using the coiflet mother wavelet for (d) $s_0(n)$, (e) $s_1(n)$ and (f) $s_2(n)$.

Bounding box

In Chapter 3, we have designed the bounding box method that defines four special coordinates in phase space diagrams computed for $m = 2$ and different values of lags. It enables to highlight the existence of time-scale transformation between two signals by trying to superpose parts of their trajectories. However, when looking to $s_1(n)$ and $s_2(n)$, we can note that the task is more complicated than expected as the time-scale transformation seems to be more complex and the signal's amplitudes are different. This is why in this section, we propose to estimate two different time-scale transformations that affect the positive and negative parts of the signals. To do so, we first need to normalize the signals by the maximal and minimal values, then compute their phase diagrams for $\tau = 1, \ldots, 20$, search for the 4 extremum points A, B, C and D, and finally compute the distance matrices H_A, H_B, H_C and H_D for both cases.

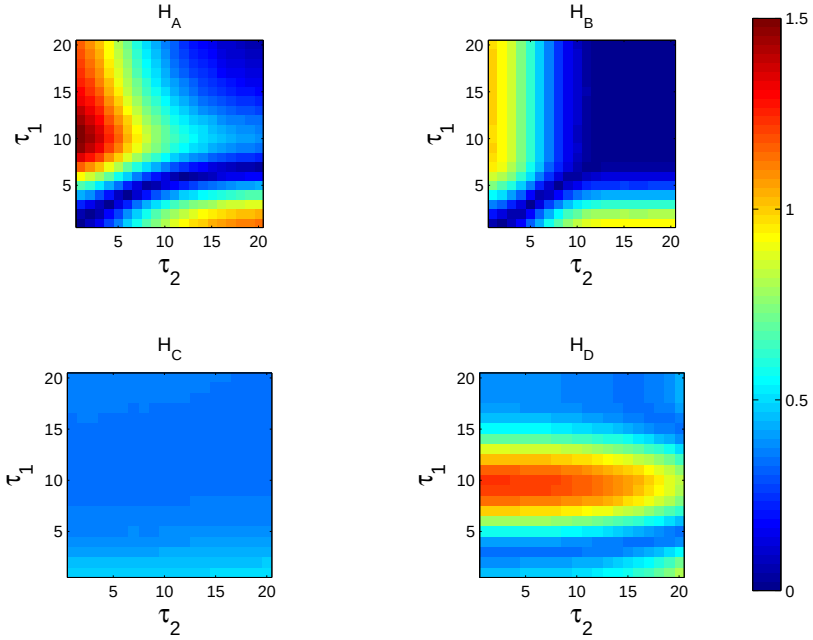

Figure 4.19: The four matrices displaying the distance between extremum points of $s_1(n)$ and $s_2(n)$ phase space diagrams for different values of lags τ_1 and τ_2. The studied signals have been normalized by their maximum values.

Figure 4.19 presents the four distance matrices H_A, H_B, H_C and H_D computed for $s_1(n)$ and $s_2(n)$ normalized by their maximum values. We can notice that H_C and H_D present values that are above or around 0.5 in average, therefore, we conclude that distances bewteen those points are constant and not worth being taken into consideration. This result is coherent with the fact that the signals have been normalized by their maximum values and C and D corresponding to the negative parts of phase space diagrams. However, we do have matches for A and B. Figure 4.20 displays the evolution of τ_1 with respect to τ_2 that provides the minimum distances bewteen A and B extremum points of phase space diagrams. Five special coordinates (highlighted by blue dots) point out the cases where we obtain the same sets of lags for minimizing the distances between the different A and B points, and are then used to

perform a linear regression. Thus, we deduce a dilation coefficient such as:

$$\tau_2 = 0.55\tau_1 \tag{4.9}$$

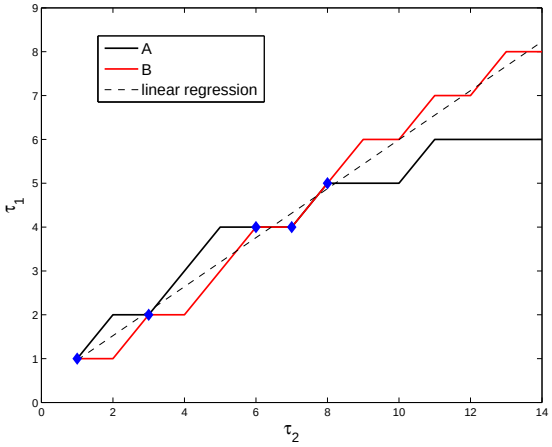

Figure 4.20: Sets of lags $[\tau_1, \tau_2]$ that provides the minimum distances between the extremum points A and B of $s_1(n)$ and $s_2(n)$'s phase space diagrams. The blue dots correspond to the sets of lags that provide minimal distances for the same sets of lags.

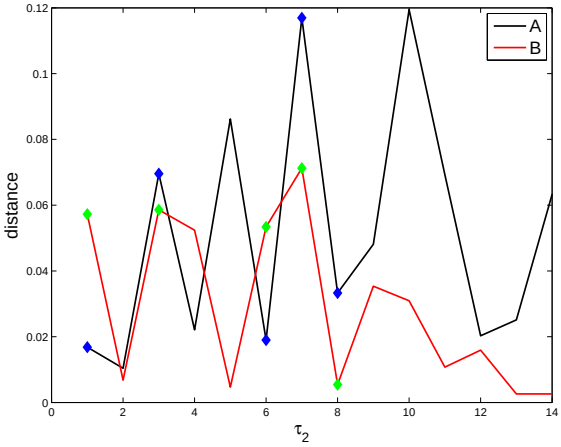

Figure 4.21: Distances between the extremum points A and B of $s_1(n)$ and $s_2(n)$'s phase space diagrams obtained for the sets of lags that provide minimal distances regarding to τ_1. The dots corresponds to the distances that are obtained for matched sets of lags.

Nevertheless, even if those couples guaranty smaller distances between the extremum coordinates compared to the other sets for a given τ_2, it does not mean that all of them are minimal. Figure 4.21 presents the evolution of the distance between extremum points A and B regarding to the evolution of τ_2. Some values have been highlighted by dots; they correspond to the distances obtained for the sets of lags that present matches. As we can see, the distances between the extremum points A and B of $s_1(n)$ and $s_2(n)$'s phase space diagrams are not constant and for certains sets of lags, the distances are not always the smaller. To illustrate this matter, we compute $T_{2,4}(s_1)$ and $T_{2,6}(s_2)$ shown in Figure 4.22, and $T_{2,5}(s_1)$ and $T_{2,8}(s_1)$ shown in Figure 4.23. The sets of lags used are the ones that were highlighted by the experiment. We can see that the top right parts of the two trajectories superpose well in the first case compared to the other one, even if the distances between A_1 and A_2, and B_1 and B_2 are smaller in the second case. This result confirms that the bounding box method cannot be used alone to determine dilation relationship. It needs to be coupled with a verification of the trajectories and/or other methods.

Nevertheless, according to Figure 4.22, we can conclude that there is a dilation coefficient equal to $\frac{\tau_2}{\tau_1} = 3/2$ between the positive parts of $s_1(n)$ and $s_2(n)$. We can then move forward the analysis of the negative parts of the signal's amplitudes.

Figure 4.24 presents the four distance matrices H_A, H_B, H_C and H_D computed for the signals normalized by their minimum values. We can notice that H_A and H_B present values that are above or around 2 in average, therefore, we conclude that distances bewteen those

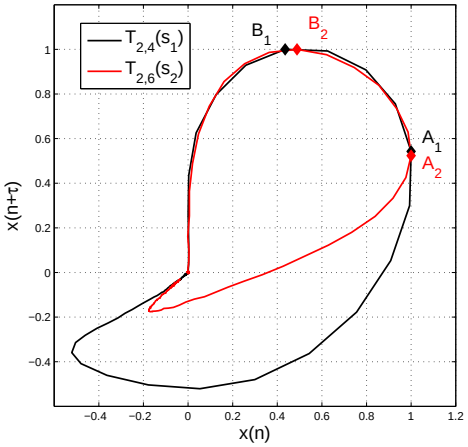

Figure 4.22: Superposition of $T_{2,4}(s_1)$ and $T_{2,6}(s_2)$ phase space diagrams. Even if the distances $d(A_1, A_2)$ and $d(B_1, B_2)$ are not minimal, the top right parts of the diagrams superpose well.

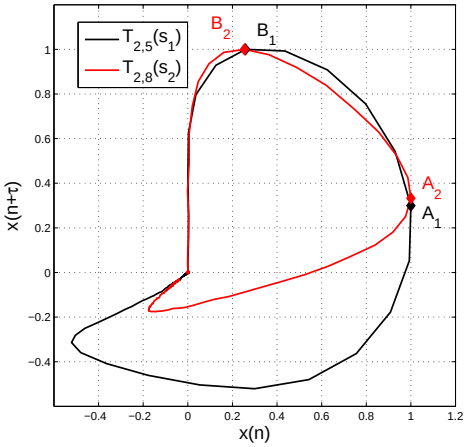

Figure 4.23: Superposition of $T_{2,5}(s_1)$ and $T_{2,8}(s_2)$ phase space diagrams. The distances $d(A_1, A_2)$ and $d(B_1, B_2)$ are smaller than in the first case but the diagrams do not superpose well.

points are not worth being taken into consideration. The distance between C_1 and C_2 is smaller and never goes above 0.8. The distance between D_1 and D_2 is more contrasted as it can goes up to 3.

We can procede to the same experiment previously presented, however due to the small portion of phase diagram that is of interest, it was not possible to determine with certitude a dilation coefficient for the negative parts of the signals. As we can see in Figure 4.25, the bottom left parts of the diagrams can be superposed for a very short curve that is not enough to conclude.

Comparison of the results with another method

In order to quantify the time-scale coefficients obtained with MLPDA tool, we propose to define an estimated dilation coefficient obtained as follows. For the normalized signal's parts of interest, we calculate the number of samples where the signal's amplitude is higher than half the maximal value, i.e. 0.5 and then compute the ratio between the two numbers to obtain the estimated dilation coefficient. For positive part, we obtain a ratio τ_1/τ_2 equal to 8/12, i.e. 2/3 which corresponds to the coefficient we previously estimated. For the negative part, we obtain 55/10, i.e. 5.5 which is a bit different. We can explain this result by the fact that a very small part of the phase diagrams are concerned by the dilation which makes it really difficult to estimate.

In this subsection, we have determined that there are two time-scale transformations between $s_1(n)$ and $s_2(n)$ corresponding to a dilation of their positive and negative parts. Even if the coefficient remains uncertain for the negative part due to its small representation in phase diagrams, we managed to define a clear coefficient for the positive part. The next step

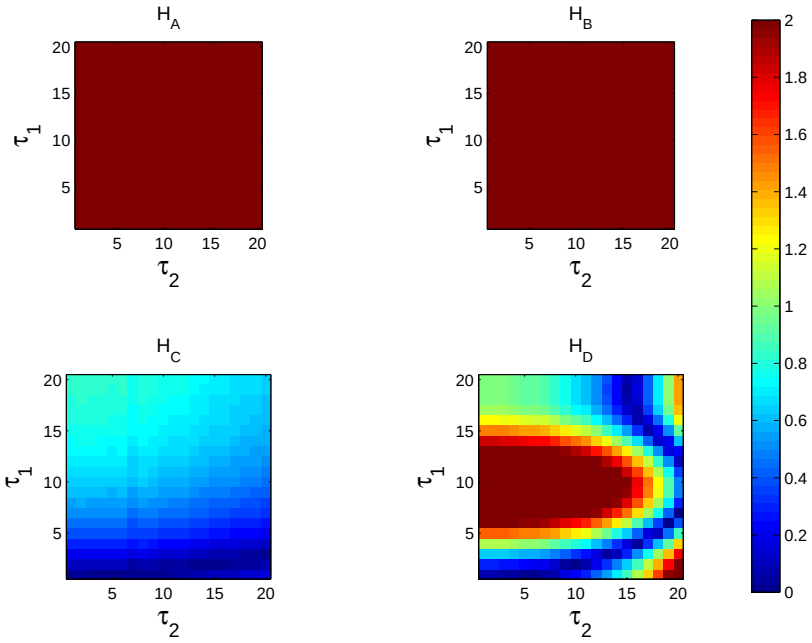

Figure 4.24: The four matrices displaying the distance between extremum points of $s_1(n)$ and $s_2(n)$'s phase space diagrams for different values of lags τ_1 and τ_2. The studied signals have been normalized by their minimum values.

is to search for an eventual amplitude relationship.

Amplitude changes:

In this part, we work with the original signals $s_1(n)$ and $s_2(n)$ and are only concerned by the amplitude relationship that eventually exists between the positive parts of the signals. To begin with, we compute the two phase diagrams shown in Figure 4.26 for the set of lags $[4, 6]$ highlighted in the previous part of the study. This set of lags enables to superpose the two phase diagrams and identify the time-scale transformation that links the positive parts of the signals.

The next step of the method is then to turn the cartesian coordinates $[x(n), y(n)]$ of phase diagrams into polar coordinates $[\rho(n), \theta(n)]$. We then look for the couples $[\rho_1(n_1), \rho_2(n_2)]$ such that $|\theta_1(n_1) - \theta_2(n_2)| < 0.05$ rad (Figure 4.27). Afterwards, we compute the ratio ρ_1/ρ_2 for each of them and display the results.

A linear relationship is highlighted if there exists an interval I where the ratio is constant along this segment. This is exactly what we have for $\theta \in [0.5, 1.4 radians]$ where the ratio is constant and equal to 2.88. If we consider the ratio between the maximum of the two signals, we have a ratio equal to 2.84 which is quite close to the experimental result.

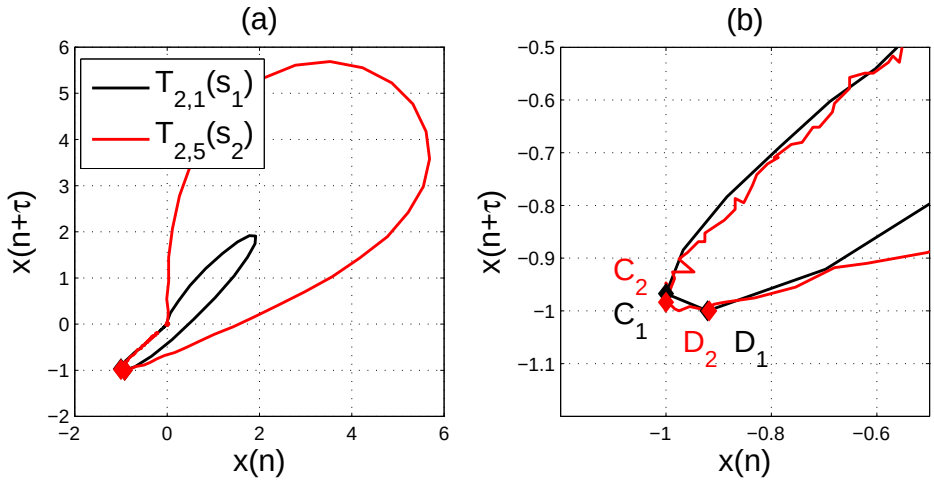

Figure 4.25: (a) Superposition of $T_{2,5}(s_1)$ and $T_{2,1}(s_2)$ phase space diagrams. (b) Zoom in the bottom left parts of the diagrams.

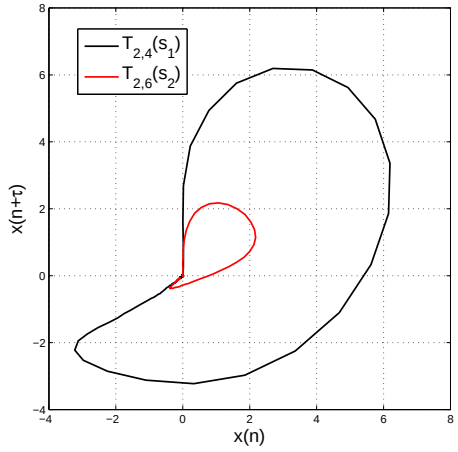

Figure 4.26: Superposition of $T_{2,4}(s_1)$ and $T_{2,6}(s_2)$ phase space diagrams.

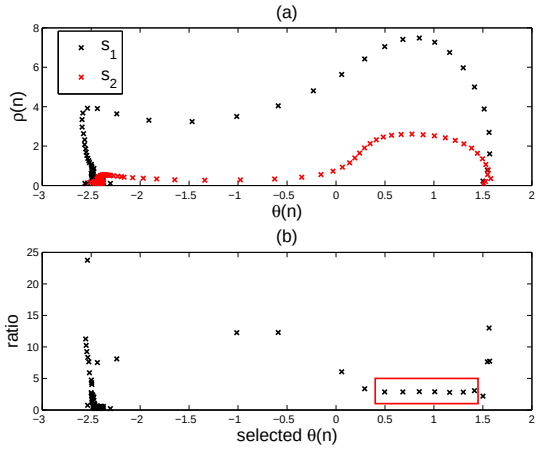

Figure 4.27: (a) $\rho = f(\theta(n))$. (b) amplitude relationship between selected coordinates.

4.2.4 Conclusion

As a conclusion, we can say that multi-lag tools have been used on partial discharge in order to characterize two signals received at two ends of cable reels. We have highlighted two distinct time-scale transformation of the positive and negative parts of the recorded data after propagation and we were able to estimate a dilation coefficient and an amplitude relationship for the positive parts of the signals. The negative parts of the signals present a bigger dilation, but it was difficult to extract an accurate coefficient. Nevertheless, MLPDA tools have shown that they are promising to extract information from signals that suffer nonlinear modification.

4.3 Passive acoustic application

4.3.1 Introduction

Another example of capital importance for power networks surveillance is the passive monitoring of hydraulic shocks in penstock pipes (Figure 2). Water hammer is a pressure surge caused when a fluid in motion is forced to stop or change direction suddenly. They commonly occur when a valve is closed at an end of a pipeline system, and a pressure wave propagates in the pipe. Although they are inevitable, they can be really dangerous if the wave does not propagate as wanted by the engineer and then cause a lot of damages in the system. Some characteristics of the transients are of great interest as they reflect the propagation of the shock wave and can reveal if the penstock has been damaged. In this section, we propose to extract one of them, namely the time rise, which provides an indication regarding the wave propagation.

4.3.2 Experimental presentation

To begin with, let recall some information regarding the pressure profil we can observe at the level of a valve in a penstock. The pressure at the bottom of a pipe is called hydrostatic pressure P_{stat} and is equal to:

$$P_{stat} = \rho g H + p_{atm} \tag{4.10}$$

where ρ is the fluid density, g is gravitational acceleration, p_{atm} is the atmospheric pressure and H is the total height of the liquid column between the altitude of the sensor and the surface of the water at the dam level. In static functionning, this pressure is supposed to remain constant over the time, and its variation is only due to the variation of the level of water in the reservoir.

When a valve closes, the system leave its stationnary functionning and starts a transient phase. A pressure surge arises that leads to an oscillation of the pressure in the pipe that is quickly attenuated. This oscillation is well known as it depends on the pipe's characteristics. The periodicity $T_{periodicity}$ is calculated as follows:

$$T_{periodicity} = \frac{4L}{a} \tag{4.11}$$

where L corresponds to the length of the pipe and a the velocity of the sound in water. During this phase a lot of things can happen that can damage the pipeline, this is why it is of great interest to monitor this kind of phenomena.

One of the most dangerous event happens when the wave's propagation is too fast. As expected the mechanical load is more important at the bottom of the pipe than at the top, this is why, a mechanical profil has been designed by engineers to take into account this information. If the water hammer propagates too fast in the pipe, then it is possible that a part of the pipe will have to endure a mechanical load that was not supposed to and then

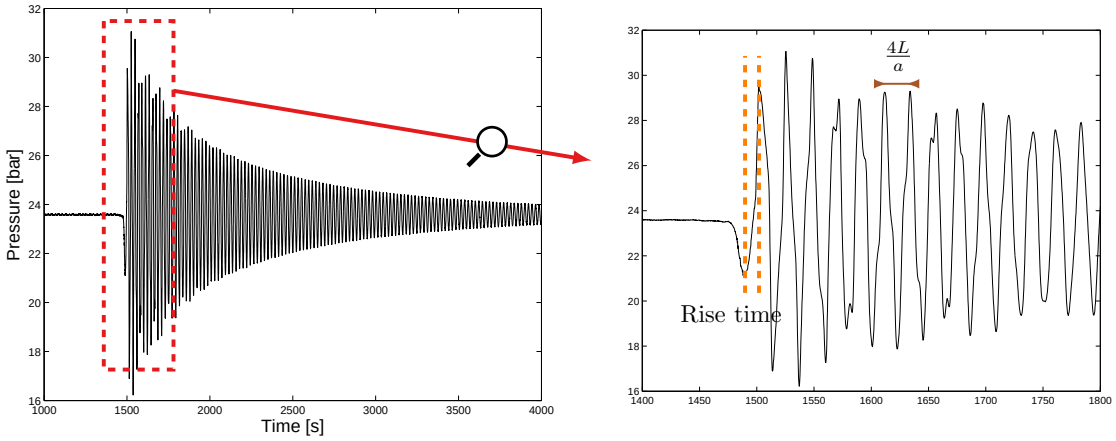

Figure 4.28: Illustration of a pressure signal and the corresponding rising time

suffers damages. This information is contained in the rising time T_{rise} (Figure 4.28): if its value is inferior to $\frac{2L}{a}$, then the wave has propagated too fast and may have caused trouble.

In this section, we propose a method based on PDA tools to calculate automatically this parameter and is presented in the next subsection.

4.3.3 Data processing

As for the ECG segmentation, the detection algorithm is based on the vector samples processing for which we define 4 parameters:

- A_{max} the maximum amplitude of the signal
- $a(n)$ the maximum amplitude between two successive phase space vectors defined as:

$$a(n) = max\left(\overrightarrow{v_{n+1}}[s, K, m]\right) - min\left(\overrightarrow{v_n}[s, K, m]\right) \tag{4.12}$$

- $r \in [0, 1]$ a ratio
- $b(n)$ the difference between the left and right parts of the phase space vector $\overrightarrow{v_n}[s, K, m]$:

$$b(n) = mean\left(\left(\overrightarrow{v_n}\left[s, K, \frac{m}{2}\right]\right)_{i=1,\ldots,\frac{m}{2}}\right) - mean\left(\left(\overrightarrow{v_n}[s, K, m]\right)_{i=\frac{m}{2},\ldots,m}\right) \tag{4.13}$$

At each instant n, the method detects a sudden amplitude rise if the maximal amplitude between the two successive phase space vectors $a(n)$ is superior to rA_{max} and if $b(n) > 0$ (denotes a rise and not a decrease). The algorithm then detects all the rising parts of the oscillations but the final result only provides the first detection interval.

In Figure 4.29, we can see the detection result for a given transient signal. The choice of parameters was set by trials and error: we choose $m = 11$ and $\tau = 1$. As we can see result is good.

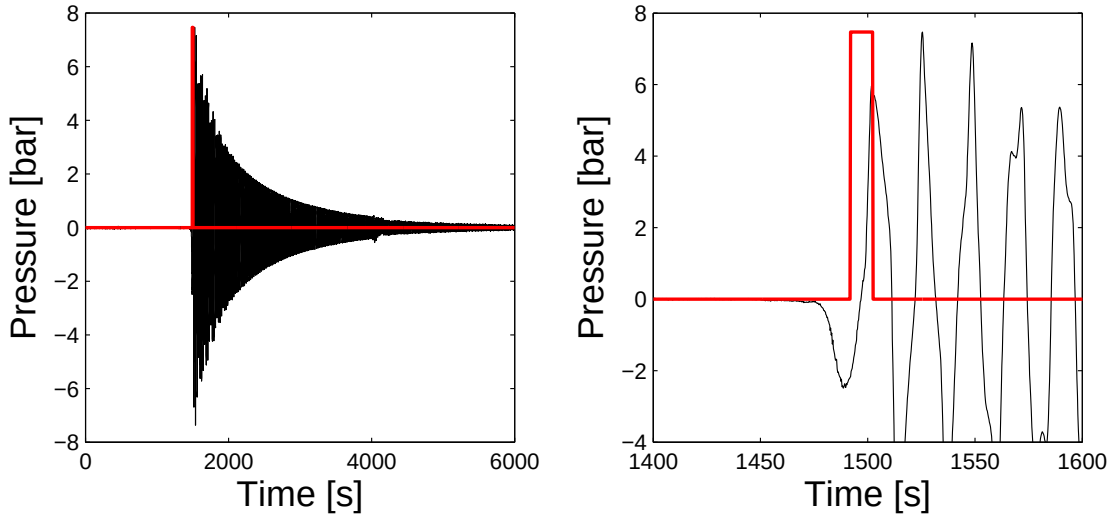

Figure 4.29: Rise time detection result for a given pressure signal

4.3.4 Conclusion

The algorithm has been tested on a large database provided by the EDF-DTG company that contained 1114 pressure signals coming from different powerplants with different configurations. A good estimation was obtained for 81.9% of them. This is why the algorihtm has also been integrated into their processing algorithm.

4.4 Application to transients propagated in an underwater environment

4.4.1 Introduction

Active acoustic sensing adresses the problem of environment characterization. When a wave $s(t)$ transmitted by a transducer T_x propagates through a dispersive medium such as a heterogeneous water environment, it suffers a lot of modifications that involve dilations and amplitude changes. Generally, a receiver R_x then records a signal $x(t)$ that is the convolution between the interrogating signal and the transfer function $h(t)$ of the medium:

$$x(t) = h(t) * s(t) \tag{4.14}$$

This transfer function not only characterizes the medium but also everything that is in the path of the interrogating wave. As a matter of consequence, if we consider two different receivers located at different loactions but sensing the same environment, the received signals will be different even if coming from the same origin.

The goal of this study is to compare two simulated signals that propagated through two different mediums whose transfer functions are related. The main idea is to estimate parameters

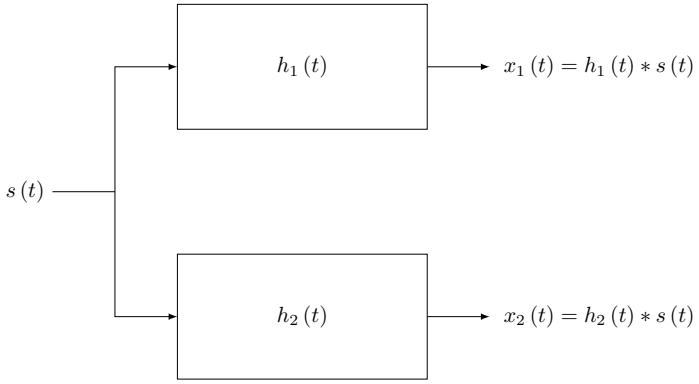

Figure 4.30: Simulation outline

that link the two of them.

4.4.2 Simulation presentation

Let consider the case of two simulated dispersive channels whose transfer functions $h_1(t)$ and $h_2(t)$ are modeled by two low-pass filtering respectively of order 128 and 512 and the normalized cut-off frequencies equal to 0.3 and 0.15. The simulated interrogating pulse corresponds to a period of sinusoid with a duration of 2 samples and an amplitude of 1. We also add gaussian noise to the signals ($SNR = 10dB$) to make the study more realistic. While Figure 4.30 presents the outline of the experiment, Figures 4.31 and 4.32 respectively show the simulated received signals and its normalized versions. As we can see, both signals obviously do not arrive at the same time instant and suffer dilation and amplitude attenuation that are due to the propagation.

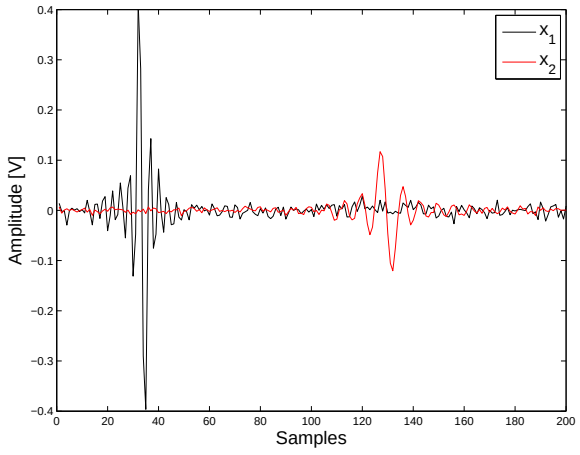

Figure 4.31: Simulated received signal

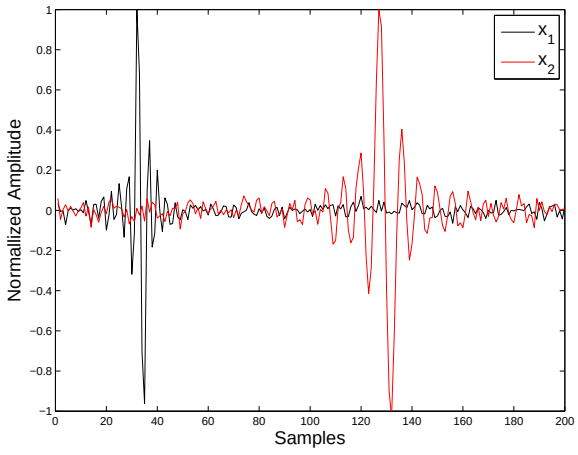

Figure 4.32: Normalized simulated received signal

We know that difference of times of arrival are of great importance to localize any obsta-

cle existing in an environment by taking into account all the echos. The time of arrival of the direct path also provides information regarding the filters' orders. The wave's filterings introduce delays that are directly proportionnal to the filter's orders. As $h_2(t)$'s order is four times greater than $h_1(t)$'s, we can then deduce that the time of arrival of $x_2(t)$ is also four times greater than $x_1(t)$'s. In our simulation, we can find out this result by considering the time of arrival of the signal's maximal values which are respectively of 32 and 127 samples. However, even if we were able to estimate this parameter, the time of arrival do not provide any information regarding the modification of amplitude and an eventual time-scale transformation. In order to investigate those parameters, we propose to use MLPDA tools on the normalized signals.

4.4.3 Data processing

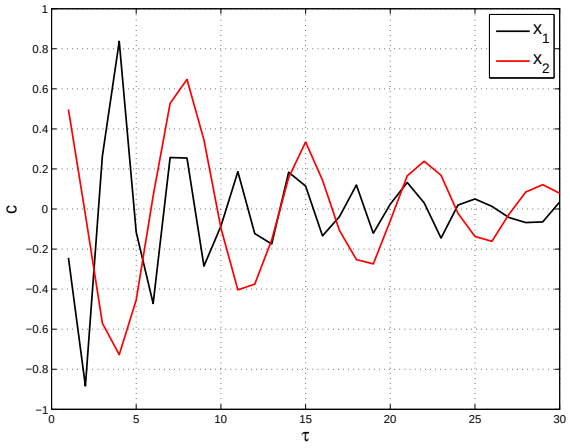

Figure 4.33: Evolution of $\widehat{a}$ with respect to τ

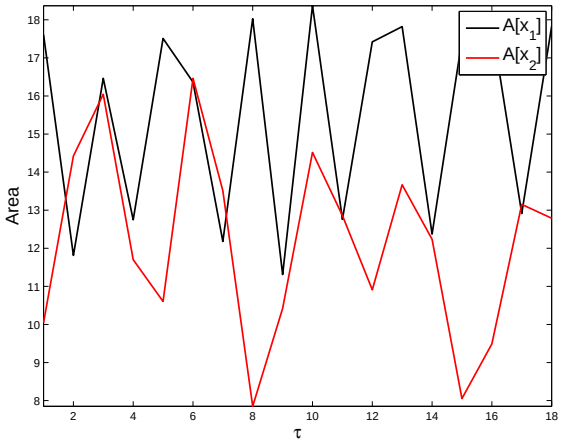

Figure 4.34: Evolution of the area with respect to the evolution of τ

To begin with, we first propose to estimate the apparent periodicity of each signals with the trend modeling method. To do so, we compute phase diagrams for $\tau = 1, \ldots, 30$, model each of them by a third degree polynomial and record the evolution of $\widehat{a}$ with respect to τ for $x_1(t)$ and $x_2(t)$. Figure 4.33 presents the associated evolution. We can then estimate the apparent periodicity $T_{periodicity}$ for both signals and we respectively obtain 3.5 and 7.33 samples for $x_1(t)$ and $x_2(t)$, which indicate a possible dilation coefficient equal to 2.09.

At this point of the study, we highlighted a possible time-scale transformation but we did not take into account proper phase diagrams as they maybe even not overlap in phase space. To complete this study, we propose to study the evolution of the area with respect to the lag. As we can see in Figure 4.34 the areas covered by the two signals are distinct as they do not evolves in the same order of magnitude. This is due to the length of $x_2(n)$ that is longer than $x_1(n)$ and also because it presents more oscillations.

In order to verify the coefficient found with the trend modeling, we propose to superpose phase diagrams for the two following sets of lags: $[2, 4]$ and $[4, 8]$. As we can see in Figures

4.35 and 4.36, both phase diagrams overlap but not perfectly. The difference is due to the amplitude modifications that are not constant (see Chapter 3). Nevertheless, these examples have shown that it was possible to estimate an accurate time-scale transformation that is conclusive with the ratio of the two cut-off frequencies.

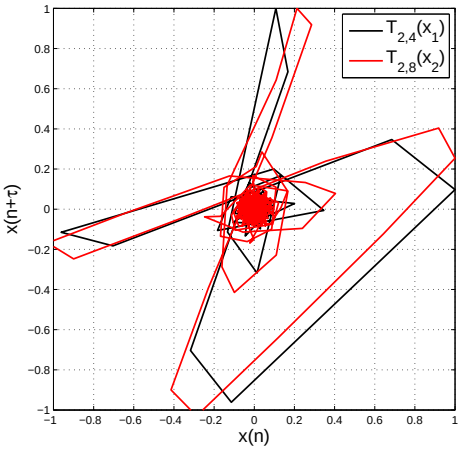

Figure 4.35: Superposition of the 2 following phase diagrams: $T_{2,4}(x_1)$ and $T_{2,8}(x_2)$

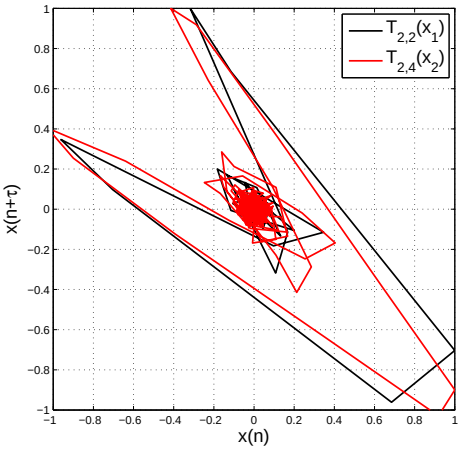

Figure 4.36: Superposition of the 2 following phase diagrams: $T_{2,2}(x_1)$ and $T_{2,4}(x_2)$

4.4.4 Conclusion

In this section, we have shown that it was possible to estimate a time-scale transformation even if the current MLPDA tools require improvements to deal with nonlinear amplitude modifications. The information extracted with MLPDA tools would not have been found with the classical technique of time of arrival.

4.5 Summary

In this Chapter, we proposed four contexts of real-life applications where RPA and MLRPA tools provided really good results. The main advantage of those methods is that they do not require any a priori information regarding the data to detect, and they can also be adapted to any other application.

Conclusion & Perspectives

This thesis addresses the problem of transient signal analysis. Due to their wide characteristics, we proposed to define three different classes of transients that are either characterized by sudden amplitude changes or by phase discontinuities of a particular order, or by nonlinear variation of the instantaneous phase. **The general aim is therefore to propose and investigate alternative analysis methods that will explore those characteristics**.

Chapter 1 presented a brief overview of the existing techniques to perform transient analysis. We determined three different classes of approaches that are the statistics, the linear projection-based approach and the data-driven analysis. All those methods enable a good detection of transient phenomena, however, when it comes to characterization for discrimination or classification purposes, we have seen that the statistical approach was very limited. The projection-based approaches permit a better characterization for signals having nonlinear variation of the instantaneous phase but remains also limited when it comes to analyze sudden amplitude changes. Moreover, all those methods usually need an a priori on the waveform to detect which is not always accessible. On the other hand, data-driven analysis techniques does not need any prior information regarding the studied data, and seem promising to investigate transients having sudden amplitude changes.

In **Chapter 2**, we decided to focus on **signals having fast-varying time-frequency representations** as their high nonlinearity is widely met in real world applications. We first focused on the generalized complex-time distribution that has the particularity to provide highly concentrated distributions around the different phase order derivatives of a signal. This technique is however limited to narrow band signals as its computation involves the calculation of signal's samples at complex coordinates. This is performed through the analytical continuation that is directly related to the signal's bandwidth. When the bandwidth is too important, the computation of the continuation usually leads to a divergence. **In order to extend the application to signals having larger frequency variations, we proposed to take advantage of time-scale operators** to compress the bandwidth of the signal and then compute the generalized complex-time distributions. This transformation allows accurate estimations of the different phase order derivatives. Moreover, the choice of the integration path is also a big deal that should be investigated more deeply. This is why future works should focus on proposing an adaptive approach for the selection of the optimal scale parameter with respect to the bandwidth variation of the analyzed signal. This could be performed through a data-driven approach like the multi-lag phase diagram analysis.

In a second part, we concentrate on **the recovery of nonlinear modulation phase signals when parts of the signals were missing** from the observation. **We proposed to combine warping operators with compressive sensing to reconstruct the signal of interest**. To do so, a time axis transformation is first performed to turn the desired signal into a sinusoid and the L-statistics enable to select the time-frequency regions of importance. Then a CS reconstruction algorithm is used to reconstruct the signal in the warped domain. Finally,

the reconstructed warped signal is expressed in the original time domain with an inverse time axis transformation. Generally, this technique performs better than a classical warping/band-pass filtering method that is hence disturbed by the missing values. Indeed, the sparsity in the warped domain enables to use compressive sensing reconstruction algorithm that only needs a few observations of the signal to reconstruct it. Nevertheless, we still need to note that this technique bets on the correct estimation of the warping function that stationnarize the desired component. If this task is not done properly, we will obtain poor results. This work has been performed in collaboration with the university of Montenegro and led to the writting of a regular paper for the *IEEE Transactions on Signal processing* and a conference paper at *IEEE Oceans Conference 2015* that are currently under review.

Chapter 3 then addresses **the problem of characterization of transients having sudden amplitude changes**. To do so, we focused on a well-known data-driven technique that is recurrence plot analysis. One of the major current research topic is the selection of the optimal set of parameters that are m the embedding dimension and τ the time delay. Generally, everyone agrees that there is no best choice as it highly depends on the application. Therefore, we decided **to explore the lag diversity in phase diagrams as some properties as time-shift and time-scale operators, and amplitude coefficient modifications can be enlighthened with invariant and shape-invariant phase diagrams** obtained with different lags. We proposed several modelings to extract parsimonious parameters from each phase diagram representations such as: ellipse modeling, third degree polynomial modeling, bounding box, area covered by the phase diagram, and a polar coordinates analysis. Their evolutions are then studied with respect to the lags or between each other to hightlight the previous properties. So far, those methods have proven themselves efficient on simulated data, and the results on applicative context are discussed in Chapter 4. Future works should therefore focus to extend this work performed for $m = 2$ to higher embedding dimensions. This could be done by applying the same methods to the projections of phase diagrams onto the different planes of the phase space. Another axis of research should also explore linear and nonlinear amplitude modifications.

Real-life context applications are then explored in **Chapter 4**. This Chapter is therefore divided into four applications that are then detailled. The first one has been developed in collaboration with Ryerson University, Toronto, Canada, where I stayed for four months. The idea was to **develop a data-driven segmentation method that provides an automatic segmentation of the three main waves of ECG time-series** known as: QRS-complex, P and T-waves. This was performed with the vector samples processing (VeSP) concept that is designed to detect sudden changes of amplitudes in time-series, and a post-processing algorithm was also proposed to enhance the results by taking care of under and over detections. However, the results of this work have been compared with annotation files that only provide the locations of every waves's maximum. More work should be carried out to find out if the proposed segmentation technique provides appropriate segmentations. Another axis of work would be to improve the obtained results with the P and T-waves segmentation by exploring for example the different parameters of the algorithm such as the lag).

Another application then focused on the **characterization of partial discharges** gener-

ated in cable reels at the lab of Grenoble-INP. Signals were recorded at both ends of the cables after different propagation ranges. They obviously suffered different nonlinear amplitude modifications that make them difficult to characterize. We took advantage of the MLPDA tools to explore some of their characteristics.

Next application is an example of **a passive acoustic configuration for water hammer monitoring**. Transients associated with water hammer are recorded and parameters are extracted from each time-series. The one we developed is **the time rise that provides an information regarding the speed of the wave**. If the duration is inferior to a certain value that depends on the facility, then the system can have suffered damages which is important to know. We proposed to use the vector samples processing concept to detect the first sudden amplitude change that corresponds to the time rise. So far, we obtained satisfying results even if the algorithm needs to be tested in more twisted configurations. The algorithm has been tested on a real database provided by EDF - DTG and it provided 82% of good detections. These satisfying results led to the algorithm's implementation in the data procesing algorithm of the company.

Finally, the fourth applicative context was the propagation of transients in an underwater environment. Due to experimental difficulties, we could not procede to a data acquisition in the lab so this experiment was replaced by a numerical simulation. To do so, we computed two dispersive channels modeled by two low-pass filtering whose parameters where connected. We simulated the propagation of an acoustic wave into these channels and studied the obtained signals. The different times of arrival provided information regarding the filters' orders, but we had to use MLPDA tools to find out a relationship between the filters's cut-off frequencies. It could be interesting to procede to an experimental acquisition in future work to verify the MLPDA tools efficiency.

Appendix A

Ellipse modeling

In analytic geometry, an ellipse is defined as the set of points (x, y) of the Cartesian plane that satisfy the following equation:

$$Ax^2 + Bxy + Cy^2 + Dx + Ey + F = 0 \tag{A.1}$$

provided $B^2 - 4AC < 0$.

If it is centered around the origine $(0, 0)$ and if its major and minor axes are respectively parallels to x and y axis, then Equation A.1 becomes:

$$Ax^2 + Cy^2 + F = 0 \tag{A.2}$$

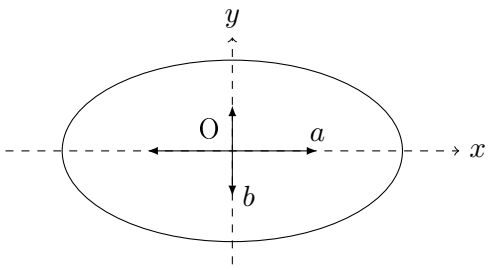

Figure A.1: Ellipse modeling

Let consider N cartesian coordinates $(x_i, y_i)_{i\in[1,\dots,N]}$ that belong to an ellipse that satisfy Equation A.2. In order to find the general equation from the coordinates, we need to minimize the following equation using the least square fitting:

$$S = \sum_{i=1}^{N} F\left(x_i, y_i\right)^2 \tag{A.3}$$

with:

$$F\left(x, y\right) = Ax^2 + Cy^2 + F \tag{A.4}$$

The development of S leads to:

$$S = \sum_{i=1}^{N} \left(Ax_i^2 + Cy_i^2 + F\right)^2 \tag{A.5}$$

$$= \sum_{i=1}^{N} \left(\left(Ax_i^2 + Cy_i^2\right)^2 + 2\left(Ax_i^2 + Cy_i^2\right)F + F^2\right) \tag{A.6}$$

$$= \sum_{i=1}^{N} \left(A^2x_i^4 + 2ACx_i^2y_i^2 + C^2y_i^4 + 2AFx_i^2 + 2CFy_i^2 + F^2\right) \tag{A.7}$$

$$\begin{aligned} S &= \sum_{i=1}^{N} \left(Ax_i^2 + Cy_i^2 + F\right)^2 \\ &= \sum_{i=1}^{N} \left(\left(Ax_i^2 + Cy_i^2\right)^2 + 2\left(Ax_i^2 + Cy_i^2\right)F + F^2\right) \\ &= \sum_{i=1}^{N} \left(A^2x_i^4 + 2ACx_i^2y_i^2 + C^2y_i^4 + 2AFx_i^2 + 2CFy_i^2 + F^2\right) \end{aligned} \tag{A.8}$$

We then look for $\{A, C, F\}$ that minimizes S. To do so, we have to solve the following system of equations:

$$\begin{cases} \frac{dS}{dA} &= 0 \\ \frac{dS}{dC} &= 0 \\ \frac{dS}{dF} &= 0 \end{cases} \tag{A.9}$$

which becomes:

$$\frac{dS}{dA} = 2A\sum_{i=1}^{N} x_i^4 + 2C\sum_{i=1}^{N} x_i^2y_i^2 + 2F\sum_{i=1}^{N} x_i^2 \tag{A.10}$$

$$\frac{dS}{dC} = 2A\sum_{i=1}^{N} x_i^2y_i^2 + 2C\sum_{i=1}^{N} y_i^4 + 2F\sum_{i=1}^{N} y_i^2 \tag{A.11}$$

$$\frac{dS}{dF} = 2A\sum_{i=1}^{N} x_i^2 + 2C\sum_{i=1}^{N} y_i^2 + 2F\sum_{i=1}^{N} 1 \tag{A.12}$$

To solve the system of equations A.9 we need to solve the following equation:

$$DX = 0 \tag{A.13}$$

such as:

$$\begin{pmatrix} \sum_{i=1}^{N} x_i^4 & \sum_{i=1}^{N} x_i^2y_i^2 & \sum_{i=1}^{N} x_i^2 \\ \sum_{i=1}^{N} x_i^2y_i^2 & \sum_{i=1}^{N} y_i^4 & \sum_{i=1}^{N} y_i^2 \\ \sum_{i=1}^{N} x_i^2 & \sum_{i=1}^{N} y_i^2 & N \end{pmatrix} \begin{pmatrix} A \\ C \\ F \end{pmatrix} = \begin{pmatrix} 0 \\ 0 \\ 0 \end{pmatrix} \tag{A.14}$$

Two things are then possible:

- $\det D = 0$ then D is not inversive and there exists an infinity of solutions to this system of equation.
- $\det D \neq 0$ then D is inversive and only one solution is possible : $X = 0$.

The second scenario is not be taken into consideration and we develop the first one that consider an infinity of equations. To solve it, it is necessary to fix one degree of liberty of the system, for example we can choose $F = -1$. The ellipse equation then becomes:

$$Ax^2 + Cy^2 = 1 \tag{A.15}$$

The system of equations then becomes:

$$\begin{pmatrix} \sum_{i=1}^{N} x_i^4 & \sum_{i=1}^{N} x_i^2 y_i^2 \\ \sum_{i=1}^{N} x_i^2 y_i^2 & \sum_{i=1}^{N} y_i^4 \end{pmatrix} \begin{pmatrix} A \\ C \end{pmatrix} = \begin{pmatrix} \sum_{i=1}^{N} x_i^2 \\ \sum_{i=1}^{N} y_i^2 \end{pmatrix} \tag{A.16}$$

i.e. :

$$DX = Q \tag{A.17}$$

The solution is finally obtained by solving:

$$X = D^{-1}Q \tag{A.18}$$

when $\det D \neq 0$.

The semi-major a and semi-minor b axis are then obtained as follows:

$$\begin{cases} a &= 1/\sqrt{A} \\ b &= 1/\sqrt{C} \end{cases} \tag{A.19}$$

Appendix B

ECG time-series results

This appendix presents the detailled results obtained for QRS-complex, P and T-waves segmentations that have been selected in Section 4.1.

Subject	Beats	TP	FN	FP	S_e	$+P$	$F1$	DER
100m	2274	2271	0	3	100.00	99.87	99.93	0.13
101m	1874	1866	2	8	99.89	99.57	99.73	0.53
102m	2192	2178	8	14	99.63	99.36	99.50	1.00
103m	2091	2083	1	8	99.95	99.62	99.78	0.43
104m	2311	2229	36	82	98.41	96.45	97.42	5.11
105m	2691	2561	53	130	97.97	95.17	96.55	6.80
106m	2098	1977	16	121	99.20	94.23	96.65	6.53
107m	2140	2132	2	8	99.91	99.63	99.77	0.47
108m	1824	781	85	1043	90.18	42.82	58.07	61.84
109m	2535	2514	10	21	99.60	99.17	99.39	1.22
111m	2133	2016	38	117	98.15	94.51	96.30	7.27
112m	2550	2538	5	12	99.80	99.53	99.67	0.67
113m	1796	1794	412	2	81.32	99.89	89.66	23.05
114m	1890	1705	57	185	96.77	90.21	93.37	12.80
115m	1962	1953	0	9	100.00	99.54	99.77	0.46
116m	2421	2384	4	37	99.83	98.47	99.15	1.69
117m	1539	1534	2	5	99.87	99.68	99.77	0.45
118m	2301	2276	12	25	99.48	98.91	99.19	1.61
119m	2094	1987	5	107	99.75	94.89	97.26	5.35
121m	1876	1251	0	625	100.00	66.68	80.01	33.32
122m	2479	2477	0	2	100.00	99.92	99.96	0.08
123m	1519	1517	1	2	99.93	99.87	99.90	0.20
124m	1634	1601	12	33	99.26	97.98	98.61	2.75
200m	2792	2591	35	201	98.67	92.80	95.64	8.45
201m	2039	1801	132	238	93.17	88.33	90.68	18.15
202m	2146	2111	1	35	99.95	98.37	99.15	1.68
203m	3108	2387	48	721	98.03	76.80	86.13	24.74
205m	2672	2652	0	20	100.00	99.25	99.62	0.75
207m	2385	1490	15	895	99.00	62.47	76.61	38.16
208m	3040	2750	5	290	99.82	90.46	94.91	9.70
209m	3052	3011	30	41	99.01	98.66	98.83	2.33

Subject	Beats	TP	FN	FP	S_e	$+P$	$F1$	DER
210m	2685	2501	11	184	99.56	93.15	96.25	7.26
212m	2763	2747	12	16	99.57	99.42	99.49	1.01
213m	3294	3249	4	45	99.88	98.63	99.25	1.49
214m	2297	2248	9	49	99.60	97.87	98.73	2.53
215m	3400	3362	4	38	99.88	98.88	99.38	1.24
217m	2280	2185	1	95	99.95	95.83	97.85	4.21
219m	2312	2152	1	160	99.95	93.08	96.39	6.96
220m	2069	2047	1	22	99.95	98.94	99.44	1.11
221m	2462	2421	3	41	99.88	98.33	99.10	1.79
222m	2634	2480	8	154	99.68	94.15	96.84	6.15
223m	2643	2534	2	109	99.92	95.88	97.86	4.20
228m	2141	1899	41	242	97.89	88.70	93.07	13.22
230m	2466	2256	2	210	99.91	91.48	95.51	8.60
231m	2011	1570	0	441	100.00	78.07	87.69	21.93
232m	1816	1779	21	37	98.83	97.96	98.40	3.19
233m	3152	3070	7	82	99.77	97.40	98.57	2.82
234m	2764	2751	0	13	100.00	99.53	99.76	0.47
Total	112647	105669	1154	6978	98.92	93.81	96.29	7.22

Table B.1: Results obtained for QRS-complex detection using $m = 10$, $N_{ero} = 10$, $N_{dil} = 30$ and $r_2 = 10\%$.

Subject	Beats	N_{init}	N_P	N_T	N_{PT}	% P-waves	% T-waves
100m	2274	4319	2027	2057	4084	89.14	90.46
101m	1874	1717	1665	20	1685	88.85	1.07
102m	2192	2904	1666	596	2262	76.00	27.19
103m	2091	2098	2067	18	2085	98.85	0.86
104m	2311	3361	831	765	1596	35.96	33.10
105m	2691	907	565	114	679	21.00	4.24
106m	2098	2110	1370	92	1462	65.30	4.39
107m	2140	3662	1418	1044	2462	66.26	48.79
108m	1824	1440	169	161	330	9.27	8.83
109m	2535	4962	2400	2377	4777	94.67	93.77
111m	2133	2168	1981	75	2056	92.87	3.52
112m	2550	4677	2325	2065	4390	91.18	80.98
113m	1796	2321	1721	511	2232	95.82	28.45
114m	1890	2073	1591	133	1724	84.18	7.04
115m	1962	2774	1773	795	2568	90.37	40.52
116m	2421	1300	1175	65	1240	48.53	2.68
117m	1539	1998	1528	461	1989	99.29	29.95
118m	2301	4190	2016	1938	3954	87.61	84.22
119m	2094	2299	1529	310	1839	73.02	14.80

Subject	Beats	N_{init}	N_P	N_T	N_{PT}	% P-waves	% T-waves
121m	1876	641	113	115	228	6.02	6.13
122m	2479	3383	1913	1398	3311	77.17	56.39
123m	1519	2791	1503	1265	2768	98.95	83.28
124m	1634	1851	1555	155	1710	95.17	9.49
200m	2792	2252	903	688	1591	32.34	24.64
201m	2039	1291	804	104	908	39.43	5.10
202m	2146	1298	1080	30	1110	50.33	1.40
203m	3108	1476	489	246	735	15.73	7.92
205m	2672	2200	807	22	829	30.20	0.82
207m	2385	946	328	78	406	13.75	3.27
208m	3040	2935	1108	240	1348	36.45	7.89
209m	3052	4115	1762	1247	3009	57.73	40.86
210m	2685	368	134	74	208	4.99	2.76
212m	2763	3956	1772	1151	2923	64.13	41.66
213m	3294	3247	69	0	69	2.09	0.00
214m	2297	2308	1960	54	2014	85.33	2.35
215m	3400	3407	65	62	127	1.91	1.82
217m	2280	3319	1555	917	2472	68.20	40.22
219m	2312	2879	1529	649	2178	66.13	28.07
220m	2069	2081	1906	9	1915	92.12	0.43
221m	2462	2364	1285	62	1347	52.19	2.52
222m	2634	2813	1043	323	1366	39.60	12.26
223m	2643	2834	2045	247	2292	77.37	9.35
228m	2141	3387	1119	839	1958	52.27	39.19
230m	2466	3413	1689	1502	3191	68.49	60.91
231m	2011	2658	1413	725	2138	70.26	36.05
232m	1816	2551	536	373	909	29.52	20.54
233m	3152	3456	897	383	1280	28.46	12.15
234m	2764	73	40	17	57	1.45	0.62
Total	112647	121573	61239	26572	87811	54.36	23.59

Table B.2: Results obtained for P and T-waves detection using $m = 30$, $N_{ero} = 10$, $N_{dil} = 30$ and $r_2 = 5\%$.

Appendix C

Résumé étendu

Caractérisation des phénomènes physiques par analyse parcimonieuse des signaux transitoires

Introduction

Les signaux transitoires de par leur nature non-stationnaire sont très difficiles à caractériser. Ils ont souvent des formes différentes qui se ressemblent plus ou moins, une durée d'observation très courte, ainsi qu'un contenu spectral très large, qui rend leur étude très compliquée. De manière générale, **le but de cette thèse est de proposer et d'étudier de nouvelles méthodes d'analyse qui exploreront les caractéristiques de ces transitoires** qui seront définis par de soudains changements dans les paramètres du signal observé. Ainsi, si nous considérons la formule analytique générale de n'importe quel signal, un transitoire sera donné par la formule suivante:

$$s(t) = A(t)\, e^{j\Phi(t)} \tag{C.1}$$

avec $A(t)$ son amplitude instantanée et $\Phi(t)$ sa phase instantanée. En fonction des changements de paramètres, nous considèrerons trois différentes classes de signaux transitoires largement rencontrées dans des applications réelles.

Les signaux sont caractérisés par des discontinuités de phase d'un ordre particulier :

Ces signaux sont modélisables de la façon suivante :

$$s(t) = \sum_k A_k e^{j a_k \cos(2k\pi t)} \tag{C.2}$$

Ces signaux sont composés de nombreuses composantes dont la phase instantanée est une fonction dérivable d'ordre supérieur. La très grande non-linéarité de cette fonction rend l'analyse très compliquée et de nouveaux domaines de représentation sont alors nécessaires. On retrouve ces signaux dans de nombreuses applications telles que le radar et l'acoustique.

Les signaux sont caractérisés par des changements d'amplitude soudains :

Ils traduisent généralement des phénomènes mécanique, électrique ou encore électromagnétique. De manière générale, nous considèrerons ces signaux de la manière suivante:

$$s(t) = A(t);\ t \in [t_0, t_0 + D] \tag{C.3}$$

avec D la durée du signal qui est beaucoup plus petite que la durée d'observation, et t_0 sa date d'apparition. On peut aussi noter que $A(t)$ est également une fonction hautement dérivable.

Les signaux ECG, de par ses variations typiques d'amplitude, sont une belle illustration de cette classe de signaux, mais nous pouvons également noter qu'une partie importante de notre étude concerne les signaux observés à une certaine distance de leur source d'émission. En effet, les signaux enregistrés contiennent des informatives relatives au signal émis à l'origine, mais aussi tous les effets introduits par la propagation et le traitement des capteurs d'enregistrement. Deux exemples de haute importance sont le cas des transitoires électriques et des signaux acoustiques de pression acquis dans des configurations passives.

Les signaux sont caractérisés par des variations non-linéaires de la phase instantanée :

$$s(t) = A(t)\, e^{j(2\pi f_0 t + \Phi(t))};\ \Phi(t) \in \mathcal{C}^4 \tag{C.4}$$

On retrouve ce genre de signaux dans de très nombreux contextes applicatifs. Nous pouvons en effet noter les signaux naturels tels que les vocalises de baleine ou les signaux de chauves-souris, dont la non-linéarité de leur phase instantanée est en effet très adaptée à leur propagation empêchant ainsi une trop grande perte d'information pour les autres spécimens. Un autre contexte applicatif très répandu concerne la transmission et propagation d'ondes acoustiques dans un milieu à des fins de caractérisation.

Tout au long du siècle dernier, de nombreuses méthodes de traitement ont été développées et sans prétendre faire un inventaire exhaustif de ces méthodes, nous proposons de les classer selon trois approches différentes qui seront développées un peu plus en détail dans le premier chapitre.

Dans cette thèse, nous proposons de développer de nouvelles techniques d'analyse pour les trois classes de signaux citées précédemment.

C.1 Rappel des méthodes existantes de traitement des signaux transitoires

Les méthodes développées pour traiter les transitoires peuvent être classées en trois grandes approches:

Les approches statistiques

Les signaux sont ici considérés uniquement comme des séries d'échantillons et on étudie leur propriétés statistiques tels que leur moyenne, leur variance et les différentes statistiques d'ordre supérieur. On part du principe que les transitoires n'ont pas un histogramme gaussien et qu'on peut donc facilement les dissocier d'un bruit blanc gaussien. Bien que ces approches permettent de faire des suppositions quant à la nature des transitoires et de bien les détecter, leur bonne caractérisation n'est pas pour autant garantie.

Les approches projectives

Il est dans la nature humaine de comparer les choses avec des référentiels connus. Cette philosophie a un équivalent en traitement du signal matérialisé par la décomposition de n'importe quel signal $s(t)$ sur des bases de fonctions élémentaires appartenant à un dictionnaire $\mathcal{D}$.

$$s(t) = \sum_{\Theta} C_{\Theta} \psi_{\Theta}(t) \tag{C.5}$$

où $\psi_{\Theta}(t)$ est une fonction élémentaire caractérisée par la liste de paramètres Θ et C_{Θ} sont les coefficients de projection montrant par leur amplitude quelle est la contribution de $\psi_{\Theta}(t)$ dans la structure de $s(t)$. Ces coefficients sont généralement calculés à l'aide du produit scalaire :

$$C_{\Theta} = \langle s(t), \psi_{\Theta}(t) \rangle \tag{C.6}$$

$$= \int_t s(t) \psi^*_{\Theta}(t) \, dt \tag{C.7}$$

Il existe un nombre important de représentations basées sur les approches projectives et nous n'en citerons que quelques unes.

La Transformée de Fourier

Cette approche permet d'exprimer un signal en termes de sinusoïdes de différentes fréquences en projetant le signal sur les fonctions élémentaires suivantes:

$$\psi_k(t) = e^{2j\pi f_k t} \tag{C.8}$$

où f_k correspond à la fréquence.

Le principal avantage de cette méthode est qu'elle permet de décrire parfaitement le contenu fréquentiel d'un signal. En revanche, si celui-ci varie au court du temps, elle ne permet pas d'en connaître l'évolution.

La Transformée de Fourier à court terme

La transformée de Fourier à court terme permet justement d'analyser le contenu fréquentiel d'un signal en fonction du temps. Pour cela, on utilise des fonctions élémentaires fenêtrées

définies comme suit:

$$\psi_{k,n}(t) = h(t - kT)\, e^{2j\pi f_n t} \tag{C.9}$$

où T correspond à la durée de la fenêtre $h(t)$.

Cette représentation est très utilisée en traitement du signal pour l'étude de signaux non-stationnaires, cependant, il est à noter qu'elle possède une sérieuse limitation quant à la résolution temps-fréquence. En effet, une bonne localisation temporelle ne pourra être obtenue qu'avec une perte d'information relative au contenu fréquentiel du signal, et inversement. Ce compromis est connu sous le nom du principe d'incertitude de Heisenberg. Afin d'améliorer un peu ce compromis, on peut toutefois utiliser des fenêtres de recouvrement.

La transformée en ondelette

Le signal est décomposé dans une base orthonormée construite à partir d'une famille de fonctions $\psi_{n,m}(t)$ appelées ondelettes:

$$\psi_{n,m}(t) = \frac{1}{\sqrt{2^m}} \psi_0 \left(\frac{t}{2m} - n \right) \tag{C.10}$$

où $\psi_0(t)$ correspond à l'ondelette mère, m est le facteur d'échelle et n est le déplacement temporel.

La base orthonormale est construite à partir des ondelettes dilatées et retardées. Ainsi, dans le plan temps-échelle, la transformée est maximale quand on obtient la meilleur correspondance entre l'ondelette dilatée et le signal étudié. Ceci pose un problème majeur puisqu'il est nécessaire d'utiliser une ondelette ressemblant au signal que l'on veut détecter pour obtenir de bons résultats et ainsi connaitre des informations à priori sur le signal recherché.

L'acquisition comprimée (compression numérique)

L'acquisition comprimée est un modèle d'échantillonnage qui nous permet de dépasser la limite de Shannon en utilisant la structure parcimonieuse d'un signal. Elle propose ainsi d'acquérir directement la version compressée du signal afin d'éviter de traiter des échantillons inutiles et permet également de reconstruire un signal avec des parties manquantes (sous certaines conditions).

Les distributions

Les distributions quadratiques proposent de projeter la fonction d'auto-corrélation des signaux sur la base de fonctions élémentaires de la transformée de Fourier. Nous pouvons citer entre autres la célèbre transformée de Wigner-Ville. Cependant, ce genre de représentation est mal adaptée aux signaux multi-composantes due à la création d'intraférences entre ces

composantes et aussi à des termes d'interférences causés par des non-linéarités. Afin de réduire ces effets, la distribution à temps complexe a été créée. Elle permet de produire des distributions concentrées autour des dérivées d'ordre K de la phase d'un signal, par contre, elle nécessite de prolonger le signal sur des contours non-réels qui limitent leur application aux signaux à bande étroite. Cette transformée sera l'objet d'un des prochains chapitres où nous proposerons d'étendre son application à des signaux plus large bande.

Les approches guidées par les données

Les approches guidées par les données permettent d'étudier des signaux sans les comparer à des choses existantes. En autre, nous pouvons citer la Décomposition en Modes Empiriques (EMD) qui permet de décomposer un signal en une série de modes intrinsèques, ainsi que l'analyse par récurrence de phase (RPA). Cette dernière permet d'obtenir une nouvelle représentation d'un signal dans un espace m-dimensionnel permettant ainsi de mettre en évidence les récurrences (retour à des états précédemment visités) dans des séries temporelles. Elle repose notamment sur le choix de 2 paramètres essentiels : la dimension m de l'espace des phases et le retard τ (ou lag). Bien que de nombreuses études aient été menées dans le but de proposer un choix optimal pour ces deux paramètres, la communauté s'accorde à dire qu'il n'en existe pas, puisqu'il dépend beaucoup du contexte d'application. Figure C.1 présente la construction d'un diagramme de phase pour un signal donné et $m = 3$.

C.2 Représentation des signaux ayant des composantes temps-fréquence variant rapidement

Dans ce chapitre, on propose de se concentrer sur les signaux ayant des composantes temps-fréquence variant rapidement. Dans une première partie, nous nous intéressons plus particulièrement aux distributions à temps complexe dont nous proposons d'étendre l'application à des signaux plus large bande en tirant profit d'une transformée temps-échelle. Dans une seconde partie, nous nous intéressons à la reconstruction de signaux à modulation de phase non linéaires dans le cadre de partie(s) manquante(s) dans le signal d'observation. Ceci sera effectué à l'aide d'opérateurs de warping et d'algorithmes de reconstruction basés sur l'acquisition comprimée.

C.2.1 Distributions à temps complexe

Les distributions à temps complexes fournissent des distributions concentrées autour des différentes dérivées de phase d'un signal. Pour ce faire, elle utilisent les moments d'ordre supérieurs du signal calculés à des temps complexes.

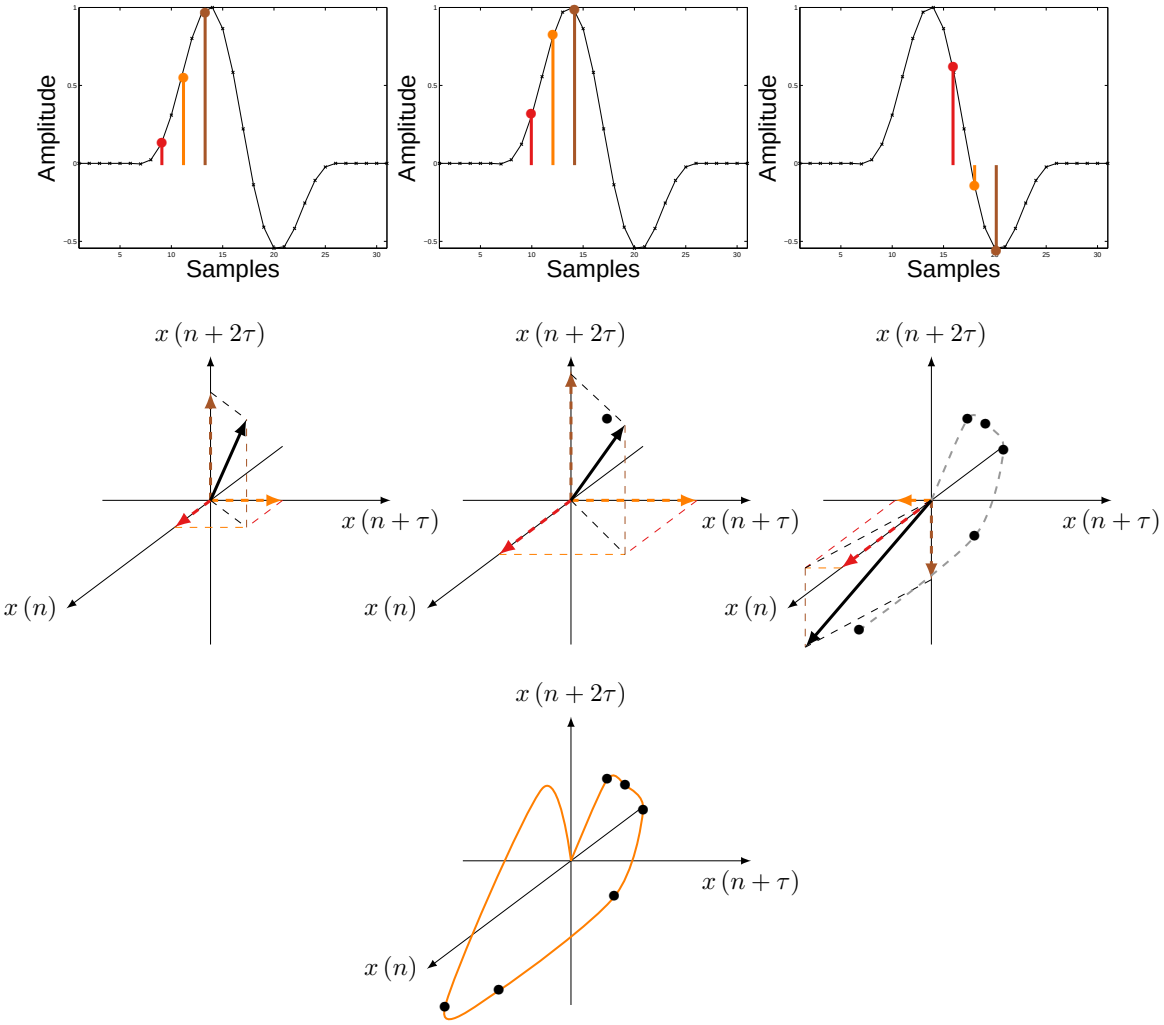

Figure C.1: Création d'un diagramme de phase pour un signal donné, $m = 3$ et $\tau = 2$.

Considérons un signal $s(t)$ défini tel que:

$$s(t) = Ae^{j\Phi(t)} \tag{C.11}$$

avec A l'amplitude du signal qui est supposée constante ou variant très lentement et $\Phi(t)$ sa loi de phase instantanée.

On définit alors la distribution généralisée à temps complexe GCD comme suit:

$$GCD_N^K[s](t,\omega) = TF_\tau\left[GCM_N^K[s](t,\tau)\right] \tag{C.12}$$

$$= \delta\left(\omega - \Phi^{(K)}(t)\right) \underset{\omega}{*} TF_\tau[Ae^{jQ(t,\tau)}] \tag{C.13}$$

avec le moment généralisé à temps complexe GCM:

$$GCM_N^K[s](t,\tau) = \prod_{p=0}^{N-1} s^{\omega_{N,p}^{N-K}} \left(t + \omega_{N,p} \sqrt[K]{\frac{K!}{N}\tau} \right) \tag{C.14}$$

$$= e^{j\Phi(K)(t)\tau + jQ(t,\tau)} \tag{C.15}$$

et la fonction d'étalement:

$$Q(t,\tau) = N \sum_{p=1}^{\infty} \Phi^{(Np+K)}(t) \frac{\tau^{\frac{Np}{K}+1}}{(Np+K)!} \left(\frac{K!}{N} \right)^{\frac{Np}{K}+1} \tag{C.16}$$

avec N étant le nombre de racine complexe de l'unité N-ième, K l'ordre de la dérivée de la phase et $\omega_{N,p}$ étant la racine de l'unité d'ordre p définie telle que:

$$\omega_{N,p} = e^{j2\pi p/N} \tag{C.17}$$

Comme on peut le constater la fonction d'étalement ne prend en compte que les dérivées de la phase d'ordre $K+N$, $K+2N$, etc... On peut donc en conclure que plus on utilisera de racine de l'unité pour calculer la distribution et plus la concentration autour de la dérivée de la phase d'ordre K sera optimale.

Cependant, pour calculer cette distribution, il est nécessaire de calculer des échantillons du signal à des temps complexes. Ceci est effectué à l'aide de la prolongation analytique calculée comme suit:

$$s(t+jm) = \int_{-\infty}^{\infty} S(f) e^{-2\pi m f} e^{j2\pi f t} df \tag{C.18}$$

où $S(f)$ est la transformée de Fourier du signal $s(t)$.

Ce calcul implique donc la multiplication du spectre du signal avec l'exponentiel $e^{-2\pi m f}$ qui va avoir différents effets sur le spectre. En effet, les fréquence positives vont être très fortement atténuées, tandis que les fréquences négatives seront très fortement amplifiées. Lorsque la bande de fréquence du signal est trop importante, ce calcul pourra même diverger. C'est cette prolongation qui limite l'utilisation de la distribution généralisée à temps complexe aux signaux à bande étroite. Afin d'étendre son utilisation aux signaux à plus large bande, on propose de modifier le support fréquentiel du signal étudié en utilisant une dilatation du signal.

Considérons le signal dilaté $s_\alpha(t)$ suivant:

$$s_\alpha(t) = s(\alpha t) \tag{C.19}$$

avec $\alpha > 1$ un facteur de dilatation et $s(t)$ le signal défini précédemment dans l'équation C.11. On a alors la correspondance suivante:

$$GCD_N^K[s](t,\omega) = \alpha GCD_N^K[s_\alpha](t,\omega) \tag{C.20}$$

Il suffit donc d'effectuer une distribution généralisée à temps complexe sur le signal dilaté, puis de la multiplier par α pour obtenir la distribution généralisée à temps complexe d'un signal à plus large bande.

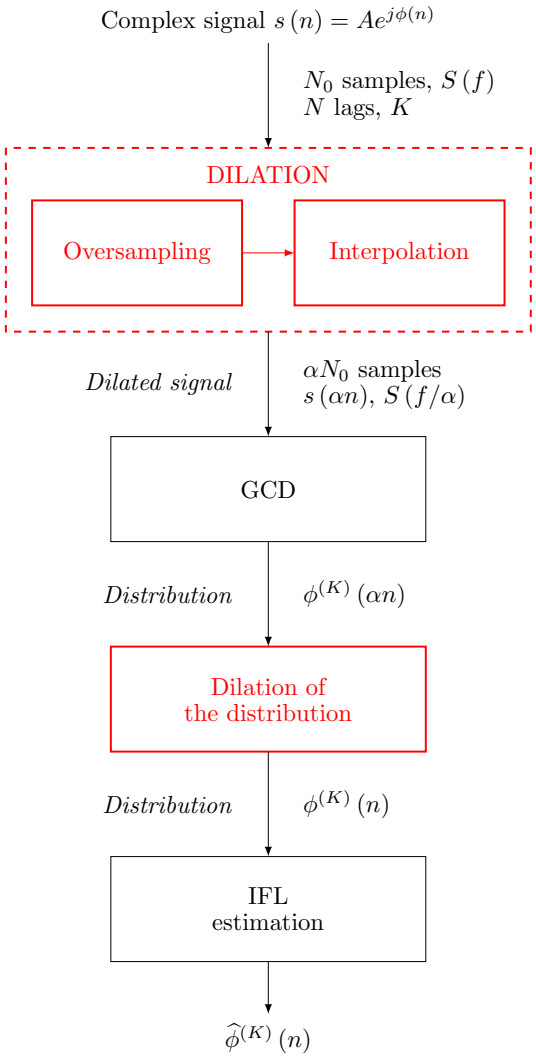

Figure C.2: Cette figure présente la procédure à suivre pour calculer la distribution temps-échelle à temps complexe.

Figure C.2 présente le schéma de fonctionnement de l'algorithme. Un exemple numérique est ensuite utilisé pour illustrer la distribution généralisée à temps complexe temps-échelle et les résultats obtenus sont comparés avec ceux obtenus avec le spectrogramme.

Le contour d'intégration choisi pour calculer la distribution complexe est d'une grande importance pour réaliser une bonne analyse, c'est pourquoi les travaux futurs devraient proposer une approche adaptative permettant de choisir un facteur d'échelle optimal en accord avec les variations de la bande passante du signal.

Ce travail a donné lieu à la rédaction d'un papier journal qui est actuellement en révision et un article conférence:

C. Bernard and C. Ioana. Generalized complex time distribution using modified analytical

continuation. In *21st European Signal Processing Conference EUSIPCO-2013*, September 2013.

C. Bernard, A. Digulescu and C. Ioana. Generalized complex time distribution using time-scale concept and modified analytical continuation. In *IEEE Transactions on Signal Processing*, en révision.

C.2.2 Analyse des signaux à modulation de phase non-linéaire basée sur les opérateurs de warping

Dans cette section, on s'intéresse à la reconstruction de signaux ayant un contenu temps-fréquentiel non stationnaire définis tels que:

$$s(t) = \sum_{i=1}^{N} s_i(t) = \sum_{i=1}^{N} A_i e^{j\psi_i(t)} \tag{C.21}$$

où N correspond au nombre de composantes, A_i leurs amplitudes et $\psi_i(t)$ leurs lois de phase instantanée non linéaire. L'étude se concentrera surtout sur deux classes particulières de signaux à modulation de phase non linéaire:

- La loi de phase logarithmique :

$$\psi_i(t) = 2\pi f_{0i} t + c_i \ln t;\ t \in [t_{0i}, t_{0i} + D_i] \tag{C.22}$$

  où f_{0i} est la fréquence centrale de la modulation, c_i le taux de modulation logarithmique, t_{0i} l'instant temporel où apparait la modulation et D_i sa durée.

- La loi de phase monomiale :

$$\psi_i(t) = 2\pi f_{0i} t + c_i t^k;\ t \in [t_{0i}, t_{0i} + D_i] \tag{C.23}$$

  avec f_{0i} la fréquence centrale de la modulation, c_i le taux de modulation, t_{0i} l'instant temporel où apparait la modulation, D_i sa durée et k l'ordre de la modulation.

On rencontre fréquemment ces signaux dans le monde de tous les jours, puisqu'ils sont utilisés notamment par les animaux pour communiquer, ou encore dans les domaines des radars et des sonars. En effet, de par leur nature, ils sont très robustes à l'effet Doppler et permettent ainsi d'être propagés sur de très longues distances sans pertes significatives. Cependant, puisque acquis dans des domaines naturels, les enregistrements sont très souvent pollués par des interférences stationnaires et non-stationnaires qui peuvent perturber leurs interprétations. Dans cette section, nous proposons de développer une technique permettant d'extraire ces composantes à partir d'observations très perturbées. La principale difficulté est que les différentes parties des signaux peuvent se superposer aussi bien en temps qu'en fréquence, ce qui rend les traditionnelles méthodes de tracking inefficaces.

Il est bien connu que les méthodes d'acquisition comprimée permettent de reconstruire des signaux à représentation parcimonieuse à partir d'un set incomplet d'échantillons. C'est cette propriété qui sera utilisée dans cette section. Cependant, comme les signaux à modulation de phase non-linéaires ne possèdent pas une représentation parcimonieuse dans le domaine de Fourier, ces signaux doivent être exprimés dans un autre domaine de représentation. Ceci est effectué à l'aide des opérateurs de warping qui permettent de modifier l'axe temporel de n'importe quel signal. Ainsi, si on considère un signal $s(t) \in \mathcal{L}(\mathbb{R})$ et l'opérateur de warping $\mathcal{W}$ défini tel que:

$$\{\mathcal{W}, \quad w(t) \in \mathcal{C}^1, \quad w'(t) > 0 : s(t) \to \mathcal{W}s(t)\} \tag{C.24}$$

où $\mathcal{C}^1$ correspond à la classe des fonctions dérivables. Alors les modifications engendrées sur le signal étudié sont exprimées tel que:

$$\mathcal{W}s(t) = s(w(t)) \tag{C.25}$$

où $w(t)$ est la fonction de warping.

En choisissant de manière appropriée cette fonction de warping, il est également possible de linéariser n'importe quel signal uniquement à partir de la donnée de quelques points de sa loi de phase instantanée. Ceci permet d'estimer cette fonction de warping même si des parties du signal sont manquantes dans le signal d'observation.

Ainsi, après la transformation de warping, on obtient un signal warpé dont la composante d'intérêt est une sinusoïde dans le domaine de Fourier mélangé à d'autres signaux stationnaires et non-stationnaires. L'étape suivante consiste ensuite à nettoyer le spectrogramme du signal warpé en enlevant les zones contenant uniquement du bruit, mais aussi les régions contenant les autres signaux. Ceci est effectué à l'aide des L-statistiques en rangeant par ordre de grandeur croissant les valeurs du spectrogramme pour chaque fréquence et en enlevant certaines valeurs. En effet, pour une fréquence donnée, il est possible d'avoir uniquement des composantes non désirées ou un mélange entre la composante recherchée et les autres composantes. En partant du principe que les plus fortes valeurs correspondent systématiquement à des termes d'interférence, on peut négliger ces valeurs. De plus, si les composantes des deux parties du signal (composantes désirées et non désirées) ont une amplitude du même ordre de grandeur, alors leur opposition de phase produit une faible amplitude à leur intersection. C'est pourquoi il est également nécessaire d'enlever les plus faibles valeurs du spectrogramme. Ainsi, pour chaque fréquence, on enlève du spectrogramme les Q plus faibles valeurs et les P plus grandes valeurs. Puis on reconstruit le spectrogramme sans ces valeurs. On obtient ainsi un spectrogramme nettoyé qui est censé ne contenir que des portions de la composante voulue. Celui ci permet ensuite de reconstruire le signal en utilisant un algorithme de reconstruction basé sur l'acquisition comprimée. Une transformation de warping inverse est ensuite nécessaire pour exprimer le signal extrait dans le domaine temporel original. Un schéma descriptif de la méthode est présenté dans la figure C.3.

Un exemple numérique est ensuite présenté où l'on montre l'intérêt de la méthode par rapport à une technique plus classique associant le warping à un filtrage passe-bande pour récupérer la fréquence d'intérêt.

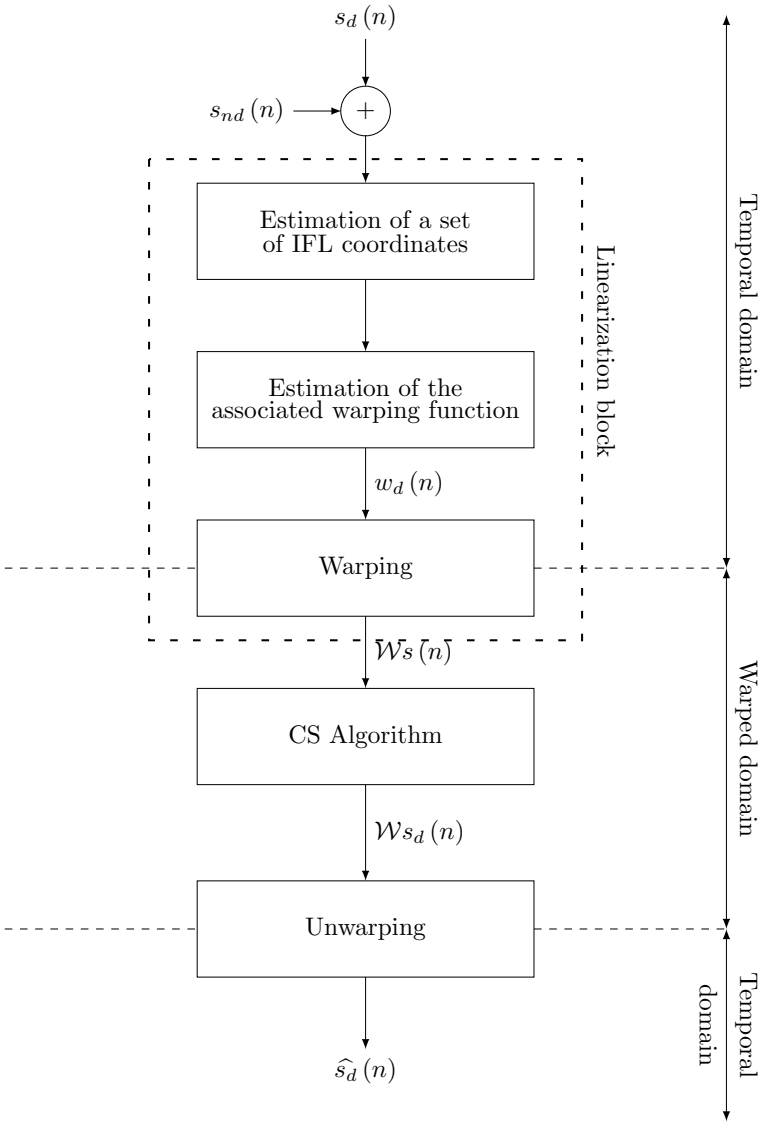

Figure C.3: Ce schéma décrit les différentes étapes permettant d'extraire un signal à modulation de phase non linéaire.

Ce travail a été réalisée en collaboration avec l'université du Monténégro et supporté financièrement par le Ministère monténégrin des sciences. (bourse de projet : "New ICT Compressive sensing based trends applied to: Multimedia, biomedicine and communications" (CS-ICT)). Un papier journal et un papier de conférence ont été rédigés lors de cette thèse.

C. Bernard, I. Orovic, C. Ioana. and S. Stanković. Compressive sensing based separation of nonlinear modulation phase signals. *IEEE Transactions on Signal Processing*, en révision.

C. Bernard, C. Ioana., I. Orovic and S. Stanković. Analysis of underwater signals with nonlinear time-frequency structures using warping-based compressive sensing algorithm. *IEEE Oceans Conference*, October 2015.

C.3 Analyse des transitoires par diagrammes de phase

Dans ce chapitre, nous nous intéresserons aux signaux de la deuxième classe qui seront modélisés par des cosinus modulés tels que:

$$s(n) = \begin{cases} \cos(2\pi f_0 n)\, w(n) & \text{if} \quad n \in [n_0, n_0 + \Delta] \\ 0 & \text{otherwise} \end{cases} \tag{C.26}$$

où $w(n)$ est une fenêtre modulante, f_0 la fréquence centrale de la modulation, n_0 l'échantillon d'arrivée du signal et Δ sa durée.

Comme nous l'avons vu dans le premier chapitre, l'analyse par récurrence de phase s'effectue en choisissant une dimension de travail m et un lag τ, mais bien souvent ces paramètres sont fixés manuellement après quelques essais sur les données applicatives. Cependant, on peut observer que de nombreuses informations différentes pourraient être extraites de chaque diagramme de phase en faisant varier les représentations en fonction du lag.

En effet, on montre dans ce chapitre, qu'il est possible d'identifier des opérateurs de déplacement temporel, d'échelles temporelles et également de modification d'amplitude en choisissant de manière intelligente les lags. Par exemple, deux signaux identiques n'apparaissant pas au même instant auront des diagrammes identiques dans l'espace des phases si les lags utilisés pour leur représentation sont les mêmes. On obtient ce même résultat pour deux signaux reliés par une dilatation d'ordre α si les lags choisis sont également multiple de α. En revanche, la modification d'amplitude est mise en évidence non pas par des représentations superposables, mais par un facteur d'échelle de ces représentations.

Nous proposons ensuite différentes méthodes permettant d'extraire des données réduites de chaque diagramme de phase. Nous explorons ensuite leur évolution par rapport à τ permettant ainsi de définir de nouvelles représentations des transitoires.

Modélisation des diagrammes de phase par des ellipses

La modélisation elliptique des signaux est assez naturelle puisqu'elle est spécifique aux signaux harmoniques. Elle nous permet d'extraire trois paramètres de chaque représentation: l'angle polaire de rotation θ (défini entre le premier axe du repère et l'axe principal de l'ellipse), le demi grand axe a et le demi petit axe b. L'évolution de l'angle polaire permet de mettre en lumière la périodicité apparente du signal, tandis que les deux autres paramètres permettent de connaitre la distribution des coordonnées de la trajectoire dans l'espace des phases. Une ellipse très fine fera état d'une distribution très concentrée, tandis qu'une ellipse large fera état d'une distribution très éparse des données.

Modélisation de la tendance des diagrammes de phase par un polynôme d'ordre 3

La modélisation par ellipse nous a fait prendre conscience que les données étaient plus ou moins concentrées autour d'une ligne dans l'espace des phases, c'est pour cette raison que nous proposons de modéliser cette tendance par un polynôme d'ordre 3 défini tel que:

$$y = \widehat{a}x^3 + \widehat{b}x^2 + \widehat{c}x + \widehat{d} \tag{C.27}$$

On extrait alors pour chaque représentation quatre paramètres: $\widehat{a}$, $\widehat{b}$, $\widehat{c}$ et $\widehat{d}$. Comme tous les signaux transitoires peuvent être défini comme ayant une moyenne nulle, on peut dès lors mettre de côté $\widehat{d}$ correspondant à l'ordonnée pour $x = 0$ qui sera nul sous cette hypothèse. Il nous reste ainsi trois paramètres qui nous permettent de mettre en évidence l'existence de modification d'échelle entre signaux en regardant leur évolution les uns par rapport aux autres (en faisant abstraction de la variation selon τ). En effet, s'ils présentent la même tendance pour plusieurs lags alors la relation est assurée.

Modélisation des diagrammes de phase par leur boite de confinement

Jusqu'ici les méthodes proposées ne nous ont pas permis d'assurer que les diagrammes étudiés étaient identiques et comme l'ajout de bruit léger a tendance à ne pas trop modifier le contour externe des diagrammes, nous proposons de définir quatre coordonnées spéciales déterminées par l'intersection entre la "boite confinement" du diagramme de phase et ce dernier tels que:

$$A: \quad \begin{cases} \forall n, \quad x(n_1) = \underset{n}{max}\,(x(n)) \\ y(n_1) \end{cases} \tag{C.28}$$

$$B: \quad \begin{cases} x(n_2) \\ \forall n, \quad y(n_2) = \underset{n}{max}\,(y(n)) \end{cases} \tag{C.29}$$

$$C: \quad \begin{cases} \forall n, \quad x(n_3) = \underset{n}{min}\,(x(n)) \\ y(n_3) \end{cases} \tag{C.30}$$

$$D: \quad \begin{cases} x(n_4) \\ \forall n, \quad y(n_4) = \underset{n}{min}\,(y(n)) \end{cases} \tag{C.31}$$

L'idée ensuite est de récupérer ces coordonnées pour tous les diagrammes de phase de plusieurs signaux et pour plusieurs valeurs de τ, puis de calculer les matrices de distance H_A, H_N,H_C et H_D définies telles que:

$$H_X = \{h_{X,i,j}\}_{i,j\in[1,\ldots,\tau_{max}]} \tag{C.32}$$

$$= \{\mathcal{D}(X_{1,i}, X_{2,j})\} \tag{C.33}$$

où $\mathcal{D}$ décrit une métrique et X la coordonnée de référence (A, B, C ou D).

Ces matrices permettent de repérer les sets de lags pour lesquels les coordonnées des points extrêmes sont très proches entre les diagrammes de phase et ainsi mettre en évidence des rapports d'échelle entre signaux.

Modélisation par l'aire sous la trajectoire

Bien que la méthode précédente permette de repérer les diagrammes de phase où les points extrêmes correspondent, cela ne garantit pas que les diagrammes se superposent pour autant. C'est pour cette raison que nous proposons de calculer l'aire sous la courbe des trajectoires, afin de rajouter un paramètre de contrôle. Pour ce faire, le diagramme de phase est considérée en coordonnées polaires $[\rho(n), \theta(n)]$ et l'aire est calculée comme suit:

$$\mathcal{A}[s] = \int_{\theta(1)}^{\theta(N)} \rho^2(n) \, |d\theta(n)| \tag{C.34}$$

On peut ensuite surveiller l'évolution de ce paramètre et comparer avec l'aire d'autres diagrammes de phase.

Analyse par coordonnées polaires

La dernière analyse présentée permet de mettre en évidence les relations d'échelles pouvant exister entre deux diagrammes de phase dont les signaux sont connectés par une modification d'amplitude constante. De même que précédemment, on considère les coordonnées polaires des diagrammes et plus particulièrement les graphes $\rho = f(\theta)$. L'idée revient à dire que pour un angle polaire donné, s'il existe une relation d'amplitude alors celle-ci se retrouve dans le ratio des deux radius correspondants. Cette méthode se révèle efficace pour repérer des modifications d'échelle constantes sur des portions de signal, cependant, l'étude demeure plus complexe dans le cas de modification d'amplitude non constante.

Dans ce chapitre, nous avons montré qu'il était possible de mettre en évidence des relations temps-échelle et des modifications d'amplitude existant entre des signaux grâce à l'analyse par diagramme de phase. Nous avons également proposé quelques méthodes d'analyse qui se sont révélées efficaces dans le cas de simulations numériques. Elles seront d'ailleurs testées dans le prochain chapitre dans le cadre de contextes applicatifs réels.

Ces travaux ont donné lieu à la rédaction d'un rapport pour EDF R&D et un papier conférence. De plus, la rédaction d'un chapitre de livre est également prévue d'ici la fin de la thèse.

C. Bernard, T. Petrut, G. Vasile, and C. Ioana. Multi-lag Phase Space Representations for Transient Signals Characterization. In *22nd European Signal Processing Conference EUSIPCO-2014*, September 2014.

C. Bernard, A. Digulescu, and C. Ioana, Multi-lag recurrence plot analysis for transient

signal characterization. To appear in 6^{th} *RPA Symposium Proceedings*, Springer (Physics section), 2015.

C.4 Résultats applicatifs

Dans ce chapitre, on s'intéresse à quatre contextes applicatifs que l'on retrouve dans la vie courante. On utilise les travaux développés dans cette thèse pour mettre en évidence certaines caractéristiques des signaux.

C.4.1 Segmentation d'ECG

Dans un premier temps, on s'intéresse à la segmentation d'ECG. En effet, chaque battement de coeur donne lieu à trois ondes: P, QRS et T (Figure C.4) qui sont d'un grand intérêt pour le diagnostique de maladies cardiaques. C'est pour cette raison que la communauté scientifique s'intéresse énormément à la segmentation de ces données et notamment au monitoring de l'évolution des intervalles de temps entre ces différentes ondes.

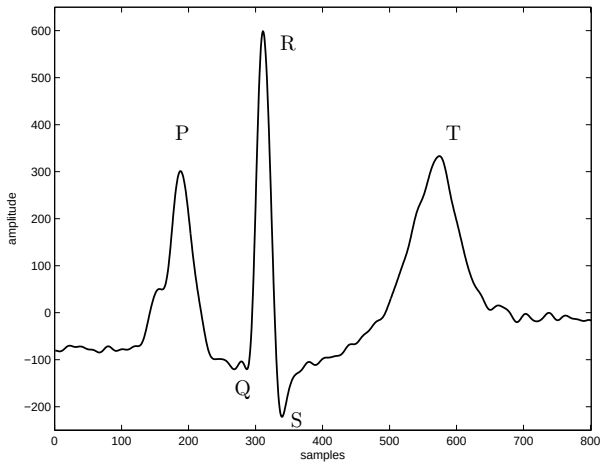

Figure C.4: Un battement de coeur classique est composé de trois ondes principales: P, QRS et T. Elles sont d'un grand intérêt pour le diagnostique cardiaque.

Pour réaliser la segmentation, on propose d'utiliser la représentation en diagramme de phase pour détecter tous les changements brusques d'amplitude. Pour ce faire l'algorithme est composée de trois étapes:

Dans un premier temps, on commence par effectuer un filtrage passe bas de la série temporelle afin d'enlever les variations rapides du signal qui sont dues aux bruits de mesure. On effectue ensuite un filtrage médian afin d'enlever une éventuelle variation de la moyenne du signal.

La deuxième étape correspond à la détection des ondes. Pour ce faire, on compare la

différence maximale d'amplitude entre deux vecteurs successifs de l'espace des phases au ratio rA_{max} où A_{max} correspond à l'amplitude maximale de la série temporelle. Le résultat de la détection est ensuite enregistré dans le vecteur binaire D.

Les détections obtenues doivent ensuite être traitées avec une morphologie mathématique afin de regrouper des détections consécutives (qui correspondent à la même onde) et de supprimer certaines détections (qui ne correspondent à rien). Pour ce faire, on commence par regrouper les détections qui sont séparées de moins de N_{dil} échantillons, puis on supprime les détections qui sont constituées de moins de N_{ero} échantillons. Cette morphologie mathématique correspond à une fermeture morphologique.

Dans les faits, la différence d'amplitude entre l'onde QRS et les ondes P et T est tellement grande qu'il n'est pas possible de détecter en même temps les ondes P et T et les ondes QRS. Nous commencerons donc par détecter les ondes QRS, puis nous les filtrerons de la série temporelle et enfin on relancera l'algorithme pour détecter les autres ondes.

Un algorithme de post-processing a également été développé afin de vérifier qu'il n'existe que deux détections entre deux ondes QRS consécutives (correspondant à une onde P et une onde T). Les conditions sont présentées dans la figure C.5.

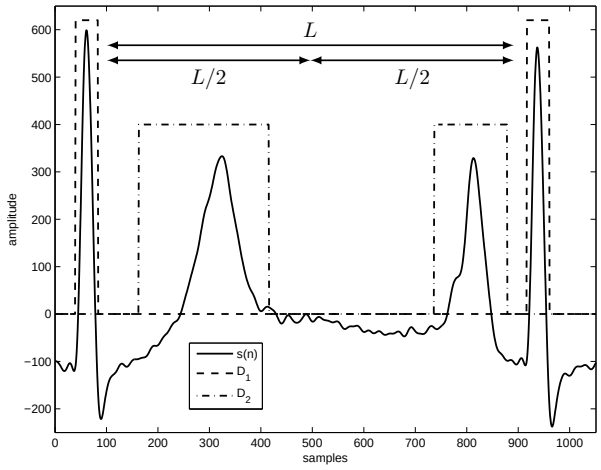

Figure C.5: Intervalle compris entre deux ondes QRS consécutives. On identifie deux parties distinctes ne contenant chacune qu'une seule onde (P ou T).

L'algorithme est ensuite testé sur une base de données ECG très connue dans la communauté scientifique: MIT-BIH. Les résultats sont évalués à partir de plusieurs critères statistiques: la sensibilité S_e, la valeur prédictive positive $+P$, le taux d'erreur de détection DER et le score $F1$. Les résultats obtenus pour la détection des QRS sont satisfaisants, par contre les résultats obtenus pour les deux autres ondes pourraient être améliorés.

Ce travail fera l'objet d'une soumission à la conférence ISSPIT en septembre 2015:

C. Bernard, C. Ioana, M. A. Hasan, and S. Krishnan. Spatial-embedding signal processing for recurrent time series: a case study with ECG signal. In 15^{th} *IEEE Symposium on Signal*

Processing and Information Technology, Décembre 2015, à soumettre.

C.4.2 Caractérisation de décharges partielles

Les transitoires électriques générés dans les équipements électriques traduisent différent phénomènes qui ont besoin d'être monitorés pour assurer la surveillance prédictive des systèmes. Leur nature peut tout aussi bien être normale (créée par un interrupteur, des changements de paramètres de charge, etc...) qu'anormale (créée par des problèmes de matériaux par exemple). Dans tous les cas, les effets tels que les arcs électriques et les décharges partielles doivent être surveillés continuellement (détection et caractérisation) pour assurer le bon fonctionnement du système.

Les décharges partielles correspondent à des défauts électriques localisés sur des systèmes isolants soumis à de forts voltages. Elles ne sont généralement pas visibles et représentent une des causes les plus courantes de panne dans les systèmes électriques. Leurs apparitions sont imprévisibles, soudaines et couvrent une large bande passante. Toutes ces propriétés rendent donc très difficile la tâche de les prévoir, les localiser et les caractériser. Dans cet exemple, on s'intéressera uniquement à leur caractérisation sachant qu'au niveau de l'enregistrement, les transitoires contiennent non seulement la forme du défaut à l'origine, mais également tous les effets induits par la propagation et l'enregistrement des capteurs. On utilisera ainsi les outils développés dans le cadre de l'analyse par diagramme de phase pour caractériser les signaux reçus après propagation d'une décharge partielle simulée en laboratoire dans des câbles électriques.

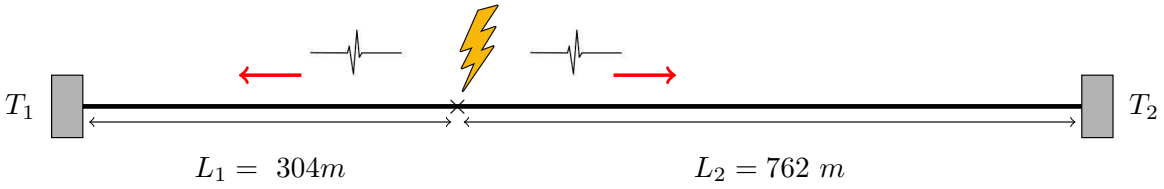

Figure C.6: Schéma expérimental de l'expérience

Pour ce faire, on enregistre les signaux électriques reçus aux deux extrémités d'un câble électrique après simulation d'une décharge partielle (Figure C.6). La distance parcourue par les signaux est différente si bien que les signaux enregistrés présentent une dilatation non-linéaire et des modifications d'amplitude plus ou moins importantes en fonction de la distance de propagation.

On montre rapidement que la transformée en ondelette n'est pas adaptée à la caractérisation de ces signaux puisque leurs formes sont modifiées. On utilise donc le méthode de la boite de confinement sur les signaux normalisés par leur valeur maximale puis minimale pour mettre en évidence deux relations temps-échelle pour les parties positives et négatives des signaux. Un facteur de dilatation est également mis en évidence pour la partie positive. Il ne fut pas possible de déterminer avec certitude la facteur de dilatation de la partie négative. Une analyse en coordonnées polaires a ensuite permis de déterminer un facteur de modification

d'amplitude constante pour la partie positive.

C.4.3 Cas d'application en acoustique passive

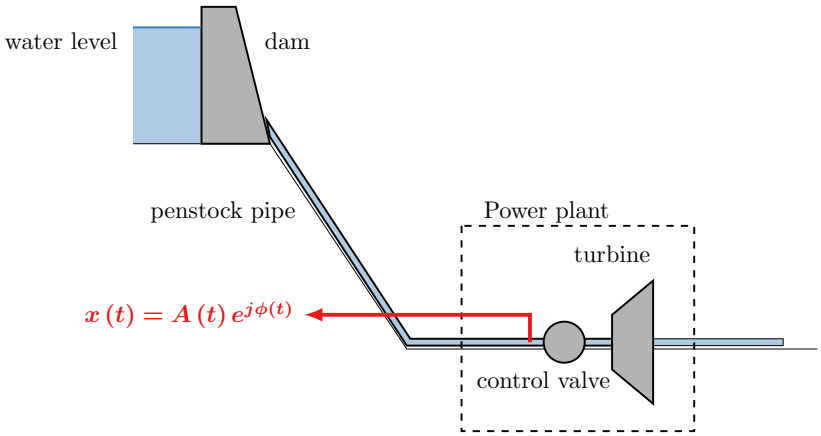

Figure C.7: Schéma général d'une centrale hydraulique.

Un autre exemple capital de monitoring est la surveillance continue des coups de bélier dans les conduites forcées des centrales hydrauliques (Figure C.7). Ils apparaissent toujours à la fermeture d'une vanne puisqu'une onde de pression est générée et remonte tout le long de la conduite. Si celle ci se propage trop rapidement, elle peut mettre en péril l'installation et occasionner de nombreux dégâts matériels. Leur surveillance est d'un grand intérêt puisque leurs caractéristiques normales de fonctionnement sont bien connues et qu'il est ainsi facile de détecter une mise en danger du système. Dans cet exemple, nous proposons de mettre en évidence le temps de montée des transitoires de pression qui est un indicateur de la vitesse de propagation du coup de bélier.

Pour commencer, on présente quelques caractéristiques générales du profil de pression généré par un coup de bélier. Quand la valve se ferme, l'onde de pression se met à osciller et s'atténue rapidement. La périodicité T est bien connue puisqu'elle dépend des paramètres de la conduite:

$$T = \frac{4L}{a} \tag{C.35}$$

avec L la longueur de la conduite et a la célérité de l'onde de pression dans l'eau. Si le temps de montée de l'onde de pression est inférieur à $T/2$, on peut en conclure que l'onde se propage trop rapidement dans la conduite forcée et que des dégâts plus ou moins importants seront occasionnés.

L'algorithme mis en place pour détecter ces temps de montée est le même que celui utilisé pour détecter les changements brusques d'amplitudes pour les ECG sauf qu'ici on ne s'intéresse qu'à la première montée positive de la détection. Les résultats obtenus ont été jugés satisfaisants et l'algorithme a été mis en place au sein de EDF DTG pour le traitement industriel des signaux de pression du parc hydraulique de EDF.

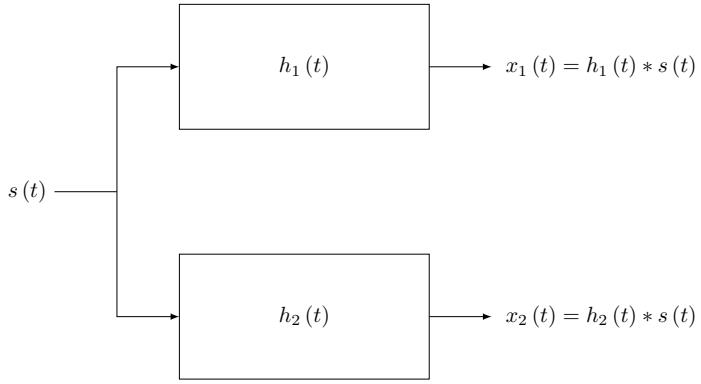

Figure C.8: Schéma de la simulation

C.4.4 Cas d'application de propagation d'onde acoustique dans un milieu immergé

La propagation active d'ondes acoustiques pose le problème de la caractérisation d'un milieu. En effet, lors de la propagation de $s(t)$ transmis par un émetteur T_x à travers un milieu dispersif comme un environnement sous-marin, l'onde subit de nombreuses modifications telles que des dilatations (ou contractions) et des modifications d'amplitude. De manière générale, un capteur R_x enregistrera un signal $x(t)$ qui correspondra à la convolution entre le signal transmis $s(t)$ et la réponse impulsionnelle du milieu $h(t)$:

$$x(t) = h(t) * s(t) \tag{C.36}$$

Cette fonction de transfert caractérise non seulement le milieu dispersif mais également tout ce qui se trouve sur le chemin de l'onde transmise. Ainsi, si on considère deux capteurs de réception situés à différents endroits, les formes des ondes reçues (même si provenant de la même origine) seront différentes.

L'idée de cette exemple est de comparer deux signaux simulés après propagation dans deux canaux dispersifs différents dont les fonctions de transfert sont connectées.

On considère ainsi les fonctions de transfert $h_1(t)$ et $h_2(t)$ modélisées par deux filtres passe-bas d'ordre respectifs 128 et 512 et de fréquences de coupure égales à $0,3$ et $0,15$. Le signal transmis $s(t)$ correspond à une période de sinusoïde ayant une durée de deux échantillons et une amplitude de 1. On ajoute également du bruit gaussien aux signaux reçus.

Le calcul de différence des temps d'arrivée nous permet facilement de retrouver le rapport entre les ordres des filtres, par contre il est difficile d'évaluer un rapport entre les fréquences des signaux. Nous utilisons donc le modélisation de la tendance des diagrammes de phase par des polynômes d'ordre 3 pour déterminer la périodicité apparente des deux signaux et le calcul de l'aire des diagrammes. Nous en concluons qu'il existe un rapport temps-échelle entre les deux signaux même si la modification d'amplitude ne nous permet pas de superposer complètement les diagrammes de phase. Ce rapport est également le même que celui existant entre les fréquences de coupure des deux filtres.

Conclusions et perspectives

Cette thèse pose le problème de l'analyse des signaux transitoires, qui de par leur nature sont très différents et possèdent de nombreuses caractéristiques. L'idée principale était donc de proposer et examiner des méthodes alternatives d'analyse pour explorer les différentes caractéristiques de ces signaux.

Dans un premier temps, trois différentes classes de signaux transitoires ont été mises en évidence et en fonction des caractéristiques recherchées, différentes pistes d'étude ont été explorées. Les traditionnelles méthodes d'analyse ont également été classées en trois approches: l'analyse statistique, les techniques projectives et les méthodes guidées par les données, et ont été développées dans le premier chapitre.

Le deuxième chapitre s'intéresse aux signaux ayant des représentations temps-fréquence variant rapidement car ils se rencontrent fréquemment dans les applications réelles tels que le radar, les signaux de mammifères marins, etc... Dans un premier temps, on s'est concentré sur les distributions généralisées à temps complexe qui permettent de caractériser les différents ordres de dérivée de la phase instantanée d'un signal. Nous avons proposé une méthode pour étendre son application aux signaux à plus large bande en tirant profit d'une transformation temps-échelle. Cette méthode donne des résultats satisfaisants, mais il serait bon de proposer une approche guidée par les données pour déterminer le choix optimal du facteur d'échelle. Ceci pourrait éventuellement être proposé à l'aide d'une approche par analyse par diagramme de phase. Dans un second temps, on s'est intéressé à la reconstruction de signaux à modulation de phase non linéaires dans le cas de données manquantes dans le signal d'observation. On tire profit d'une opération de warping visant à linéariser la composante d'intérêt et des L-statistiques pour nettoyer le spectrogramme. On utilise ensuite un algorithme de reconstruction basée sur l'acquisition comprimée pour reconstruire la sinusoïde. Puis une opération inverse de warping permet de récupérer la composante d'intérêt dans le domaine temporel original. Cette méthode a montré son efficacité dans un exemple et sa supériorité vis-à-vis d'une approche plus classique associant un warping avec un filtrage passe-bande.

Le troisième chapitre pose le problème de la caractérisation des signaux ayant de soudains changements d'amplitudes par le biais de l'analyse par diagramme de phase. Comme les opérations de déplacement temporel, d'échelle temporelle et également de modification d'amplitude peuvent être mis en évidence en choisissant de manière intelligente le lag dans les diagrammes de phase, on propose différentes méthodes permettant de révéler les invariances dans les diagrammes de phase. Pour ce faire, on propose différentes approches permettant d'extraire un nombre de paramètres réduit de chaque diagramme calculé pour différent lag. Ces paramètres sont ensuite comparés permettant ainsi la mise évidence des propriétés précédemment citées. Les futurs axes de recherche pourront proposer d'étendre ces travaux à des dimensions d'ordre supérieur. Une solution possible est d'utiliser les mêmes méthodes développées aux projections des diagrammes de phase sur les différents plans de l'espace des phases. On pourra également continuer l'étude des modifications d'amplitude linéaires et non-linéaires.

Le quatrième chapitre propose d'explorer quatre contextes applicatifs qui sont la segmen-

tation d'ECG, la caractérisation de décharge partielle, un cas d'acoustique passive et un autre cas d'acoustique active. Les méthodes d'analyse par diagramme de phase sont utilisées et permettent d'extraire de nombreuses informations des signaux étudiés.

Bibliography

[AaB07] R. V. Andreão and J. Boudy. Combining Wavelet Transform and Hidden Markov Models for ECG Segmentation. *EURASIP Journal on Advances in Signal Processing*, 2007(1), January 2007.

[AaDB06] R. V. Andreão, B. Dorizzi, and J. Boudy. ECG signal analysis through hidden Markov models. *IEEE Transactions on Biomedical Engineering*, 53(8):1541–1549, August 2006.

[AKSA07] A. Ahmadian, S. Karimifard, H. Sadoughi, and M. Abdoli. An efficient piecewise modeling of ECG signals based on Hermitian basis functions. *IEEE Engineering in Medicine and Biology Society. Annual Conference*, pages 3180–3183, January 2007.

[Bar07] R.G. Baraniuk. Compressive Sensing. *IEEE Signal Processing Magazine*, 24(4):118–121, 2007.

[BGZF01] D. Benitez, P.A. Gaydecki, A. Zaidi, and A.P. Fitzpatrick. The use of the Hilbert transform in ECG signal analysis. *Computers in Biology and Medicine*, 31(5):399–406, September 2001.

[BJ93a] R.G. Baraniuk and D.L. Jones. Unitary Equivalence and Signal Processing. In *International Symposium on the Mathematical Theory of Networks*, pages 617–620, 1993.

[BJ93b] R.G. Baraniuk and D.L. Jones. Warped Wavelet Bases: Unitary Equivalence And Signal Processing. In *IEEE International Conference on Acoustics, Speech, and Signal Processing*, pages 320–323, 1993.

[BJ95] R.G. Baraniuk and D.L. Jones. Unitary equivalence: a new twist on signal processing. *IEEE Transactions on Signal Processing*, 43(10):2269–2282, 1995.

[Coh95] L. Cohen. *Time-frequency analysis*. Prentice Hall, 1995.

[Cor06] Cedric Cornu. *Extraction de signaux et caracterisation de lois de phase instantanée : Application aux modulations non linéaires*. PhD thesis, Université de Bretagne Occidentale, October 2006.

[CRT06] E.J. Candes, J. Romberg, and T. Tao. Robust uncertainty principles: exact signal reconstruction from highly incomplete frequency information. *IEEE Transactions on Information Theory*, 52(2):489–509, 2006.

[CSI+07] C. Cornu, S. Stanković, C. Ioana, A. Quinquis, and L. Stanković. Generalized Representation of Phase Derivatives for Regular Signals. *IEEE Transactions on Signal Processing*, 55(10):4831–4838, October 2007.

[CT06] E.J. Candes and T. Tao. Near-Optimal Signal Recovery From Random Projections: Universal Encoding Strategies? *IEEE Transactions on Information Theory*, 52(12):5406–5425, 2006.

[Dau90] I. Daubechies. The wavelet transform, time-frequency localization and signal analysis. *IEEE Transactions on Information Theory*, 36(5):961–1005, 1990.

[Dau92] I. Daubechies. *Ten Lectures on Wavelets*. CBMS-NSF Regional Conference Series in Applied Mathematics, 1992.

[dCOR04] P. de Chazal, M. O'Dwyer, and R. B. Reilly. Automatic classification of heartbeats using ECG morphology and heartbeat interval features. *IEEE transactions on bio-medical engineering*, 51(7):1196–1206, July 2004.

[dCR03] P. de Chazal and R.B. Reilly. Automatic classification of ECG beats using waveform shape and heart beat interval features. In *IEEE International Conference on Acoustics, Speech, and Signal Processing*, volume 2, pages 269–272, 2003.

[Don06] D.L. Donoho. Compressed sensing. *IEEE Transactions on Information Theory*, 52(4):1289–1306, 2006.

[EKR87] J.-P Eckmann, S. O. Kamphorst, and D Ruelle. Recurrence Plots of Dynamical Systems. *Europhysics Letters (EPL)*, 4(9):973–977, November 1987.

[Faw06] T. Fawcett. An introduction to ROC analysis. *Pattern Recognition Letters*, 27(8):861–874, June 2006.

[FB10] P. Flandrin and P. Borgnat. Time-Frequency Energy Distributions Meet Compressed Sensing. *IEEE Transactions on Signal Processing*, 58(6):2974–2982, 2010.

[GAG+00] A. L. Goldberger, L. A. N. Amaral, L. Glass, J. M. Hausdorff, P. Ch. Ivanov, R. G. Mark, J. E. Mietus, G. B. Moody, C.-K. Peng, and H. E. Stanley. PhysioBank, PhysioToolkit, and PhysioNet : Components of a New Research Resource for Complex Physiologic Signals. *Circulation*, 101(23):215–220, June 2000.

[GB03] S. Graja and J. Boucher. Multiscale hidden Markov model applied to ECG segmentation. In *2003 IEEE International Symposium on Intelligent Signal Processing*, pages 105–109, 2003.

[GGG08] A. Ghaffari, H. Golbayani, and M. Ghasemi. A new mathematical based QRS detector using continuous wavelet transform. *Computers & Electrical Engineering*, 34(2):81–91, March 2008.

[GIS+08] B. Gottin, C. Ioana, S. Stanković, L. Stanković, and J. Chanussot. On the concept of time-frequency distributions based on complex-lag moments. In *16th European Signal Processing Conference EUSIPCO-2008 EURASIP*, 2008.

[Got10] Bertrand Gottin. *Analyse multi-capteurs de signaux transitoires issus de systèmes électriques*. PhD thesis, Université de Grenoble, September 2010.

[HAB12] M. A. Hasan, D. Abbott, and M. Baumert. Beat-to-beat vectorcardiographic analysis of ventricular depolarization and repolarization in myocardial infarction. *PloS one*, 7(11), January 2012.

[HAB13] M. A. Hasan, D. Abbott, and M. Baumert. Beat-to-beat QT interval variability and T-wave amplitude in patients with myocardial infarction. *Physiological measurement*, 34(9):1075–1083, September 2013.

[HCIS98] Q.Q. Huynh, L.N. Cooper, N. Intrator, and H. Shouval. Classification of underwater mammals using feature extraction based on time-frequency analysis and BCM theory. *IEEE Transactions on Signal Processing*, 46(5):1202–1207, May 1998.

[HPSBB99] F. Hlawatsch, A. Papandreou-Suppappola, and G. Boudreaux-Bartels. The power classes-quadratic time-frequency representations with scale covariance and dispersive time-shift covariance. *IEEE Transactions on Signal Processing*, 47(11):3067–3083, 1999.

[HS05] N. E. Huang and S. S. Shen. *Hilbert-Huang Transform and Its Applications*. World Scientific, 2005.

[HW08] N. E. Huang and Z. Wu. A review on Hilbert-Huang transform: Method and its applications to geophysical studies. *Reviews of Geophysics*, 46(2), June 2008.

[IDS+14] C. Ioana, A. Digulescu, A. Serbanescu, I. Candel, and F.-M. Birleanu. Recent Advances in Non-stationary Signal Processing Based on the Concept of Recurence Plot Analysis. In N. Marwan, M. Riley, A. Giuliani, and C. L. Jr. Webber, editors, *Translational Recurrences: From Mathematical Theory to Real-World Applications*, pages 75–93. Springer P, 2014.

[IGSM10] C. Ioana, C. Gervaise, Y. Stéphan, and J. I. Mars. Analysis of underwater mammal vocalisations using time–frequency-phase tracker. *Applied Acoustics*, 71(11):1070–1080, November 2010.

[IQS06] C. Ioana, A. Quinquis, and Y. Stephan. Feature Extraction from Underwater Signals using Time-Frequency Warping Operators. *IEEE Journal of Oceanic Engineering*, 31(3):628–646, July 2006.

[JAS13] B. Jokanović, M. Amin, and S. Stanković. Instantaneous frequency and time-frequency signature estimation using compressive sensing. In Kenneth I. Ranney and Armin Doerry, editors, *SPIE Defense, Security, and Sensing*. International Society for Optics and Photonics, 2013.

[JIQ06] A. Jarrot, C. Ioana, and A. Quinquis. An Extension of the Class Of Unitary Time–Warping Projectors To Discrete–Time Sequences. In *IEEE International Conference on Acoustics, Speech, and Signal Processing*, volume 3, pages 412–415, 2006.

[Jos10] Nicolas Josso. *Caractérisation des milieux sous marins en utilisant des sources mobiles d'opportunité*. PhD thesis, Université de Grenoble, January 2010.

[LAC97] J-L Lacoume, P-O Amblard, and P. Comon. *Statistiques d'ordre supérieur pour le traitement du signal*. MASSON, 1997.

[LBBC01] R. Lepage, J.-M. Boucher, J.-J. Blanc, and J.-C. Cornilly. ECG segmentation and P-wave feature extraction: application to patients prone to atrial fibrillation. In *Engineering in Medicine and Biology Society*, volume 1, pages 298–301. IEEE, 2001.

[LZT95] C. Li, C. Zheng, and C. Tai. Detection of ECG characteristic points using wavelet transforms. *IEEE Transactions on Biomedical Engineering*, 42(1):21–28, 1995.

[Mal99] S. G. Mallat. *A wavelet tour of signal processing*. Academic Press, San Diego, 2nd edition, 1999.

[MAO+04] J. P. Martínez, R. Almeida, S. Olmos, A. P. Rocha, and P. Laguna. A wavelet-based ECG delineator: evaluation on standard databases. *IEEE transactions on bio-medical engineering*, 51(4):570–81, April 2004.

[Mar08] N. Marwan. A historical review of recurrence plots. *The European Physical Journal Special Topics*, 164(1):3–12, November 2008.

[MCOS07] J. P. V. Madeiro, P. C. Cortez, F. I. Oliveira, and R. S. Siqueira. A new approach to QRS segmentation based on wavelet bases and adaptive threshold technique. *Medical engineering & physics*, 29(1):26–37, January 2007.

[MCTK07] N. Marwan, M. Carmenromano, M. Thiel, and J. Kurths. Recurrence plots for the analysis of complex systems. *Physics Reports*, 438(5-6):237–329, January 2007.

[Mei02] E. Meijering. A chronology of interpolation: from ancient astronomy to modern signal and image processing. *Proceedings of the IEEE*, 90(3):319–342, March 2002.

[MK02] N. Marwan and J. Kurths. Nonlinear analysis of bivariate data with cross recurrence plots. *Physics Letters A*, 302(5-6):299–307, September 2002.

[MS95] Y. Meyer and D. H. Salinger. *Wavelets and Operators*, volume 1. 1995.

[OSS14] I. Orovic, S. Stanković, and L. Stanković. Compressive sensing based separation of LFM signals. In *IEEE Proceedings ELMAR-2014*, pages 1–4, September 2014.

[PCFS80] N. Packard, J. Crutchfield, J. Farmer, and R. Shaw. Geometry from a Time Series. *Physical Review Letters*, 45(9):712–716, September 1980.

[PHBB93] A. Papandreou, F. Hlawatsch, and G.F. Boudreaux-Bartels. The hyperbolic class of quadratic time-frequency representations. I. Constant-Q warping, the hyperbolic paradigm, properties, and members. *IEEE Transactions on Signal Processing*, 41(12):3425–3444, 1993.

[Phy] PhysioNet. The MIT-BIH Normal Sinus Rhythm Database. `http://physionet.org/physiobank/database/nsrdb/`.

[Pow11] D. M. Powers. Evaluation: from Precision, Recall and F-measure to ROC, Informedness, Markedness and Correlation. *Journal of Machine Learning Technologies*, 2(1):37–63, December 2011.

[PS95] A. Papandreou-Suppappola. Generalized time-shift covariant quadratic time-frequency representations with arbitrary group delays. In *Conference Record of The Twenty-Ninth Asilomar Conference on Signals, Systems and Computers*, volume 1, pages 553–557. IEEE Comput. Soc. Press, 1995.

[PSHBB98] A. Papandreou-Suppappola, F. Hlawatsch, and G.Faye Boudreaux-Bartels. Quadratic Time-Frequency Representations with Scale Covariance and Generalized Time-Shift Covariance: A Unified Framework for the Affine, Hyperbolic, and Power Classes. *Digital Signal Processing*, 8(1):3–48, January 1998.

[RA98] P. Ravier and P-O Amblard. Combining an adapted wavelet analysis with fourth-order statistics for transient detection. *Signal Processing*, 70(2):115–128, October 1998.

[RA01] P. Ravier and P-O Amblard. Wavelet packets and de-noising based on higher-order-statistics for transient detection. *Signal Processing*, 81(9):1909–1926, September 2001.

[RPA] Recurrence plots and cross recurrence plots. `http://www.recurrence-plot.tk/`. Accessed: 2015-07-05.

[Rud87] W. Rudin. *Real and Complex Analysis*. McGraw Hil, Boston, Mass, USA, 1987.

[Sma05] M. Small. Applied nonlinear time series analysis. Applications in physics, physiology and finance. 2005.

[SMF10] J-L Starck, F. Murtagh, and J. M. Fadili. *Sparse image and signal processing: Wavelets, Curvelets, Morphological Diversity*. Cambridge University Press, 2010.

[SOSA13] L. Stanković, I. Orovic, S. Stanković, and M. Amin. Compressive Sensing Based Separation of Nonstationary and Stationary Signals Overlapping in Time-Frequency. *IEEE Transactions on Signal Processing*, 61(18):4562–4572, 2013.

[SS96] S. Stanković and L. Stanković. Introducing time-frequency distribution with a 'complex-time' argument. *Electronics Letters*, 32(14):1265, 1996.

[SS09] O. Sayadi and M. B. Shamsollahi. A model-based Bayesian framework for ECG beat segmentation. *Physiological measurement*, 30(3):335–52, March 2009.

[SSA14] L. Stanković, S. Stanković, and M. Amin. Missing samples analysis in signals for applications to L-estimation and compressive sensing. *Signal Processing*, 94:401–408, January 2014.

[Sta02] L. Stanković. Time-frequency distributions with complex argument. *IEEE Transactions on Signal Processing*, 50(3):475–486, March 2002.

[STD06] L. Stankovic, T. Thayaparan, and M. Dakovic. Signal Decomposition by Using the S-Method With Application to the Analysis of HF Radar Signals in Sea-Clutter. *IEEE Transactions on Signal Processing*, 54(11):4332–4342, November 2006.

[Tak81] F. Takens. *Dynamical Systems and Turbulence, Warwick 1980*, volume 898 of *Lecture Notes in Mathematics*. Springer Berlin Heidelberg, 1981.

[TAR+07] T. Thayaparan, S. Abrol, E. Riseborough, L. Stankovic, D. Lamothe, and G. Duff. Analysis of radar micro-Doppler signatures from experimental helicopter and human data. *IET Radar, Sonar & Navigation*, 1(4):289, August 2007.

[TBU00] P. Thévenaz, T. Blu, and M. Unser. Interpolation revisited. *IEEE transactions on medical imaging*, 19(7):739–58, July 2000.

[VVV98] H.J.L.M. Vullings, M.H.G. Verhaegen, and H.B. Verbruggen. Automated ECG segmentation with dynamic time warping. In *IEEE Engineering in Medicine and Biology Society*, volume 1, pages 163–166. IEEE, 1998.

[ZW92] J. P. Zbilut and C. L. Webber. Embeddings and delays as derived from quantification of recurrence plots. *Physics Letters A*, 171(3-4):199–203, December 1992.

Résumé — Les signaux transitoires, de par leur unicité, sont très difficiles à caractériser. Ils se rencontrent partout et sont généralement le reflet d'un phénomène physique très complexe traduisant de nombreuses informations telles que le signal à l'origine, les effets de la propagation dans le milieu considéré et aussi les effets induits par les capteurs. Ils peuvent aussi bien correspondre à un phénomène de communication entre animaux, qu'être le reflet d'un défaut dans un système électrique ou hydraulique par exemple. Tout ceci rend leur étude très difficile, mais aussi primordiale. De nombreuses techniques en traitement du signal ont été développées ces dernières années pour les étudier: elles reposent souvent sur des approches statistiques, des approches projectives sur différents dictionnaires et des techniques auto-adaptatives. Toutes ces méthodes présentent des avantages et des inconvénients, puisqu'elles permettent souvent de les détecter correctement, néanmoins leur caractérisation à des fins de classification et de discrimination reste compliquée. Cette thèse s'inscrit dans cette optique et propose de nouvelles approches d'étude des transitoires. Après un rapide descriptif des techniques d'étude des signaux transitoires, ce travail s'intéressera dans un premier temps à la représentation des signaux ayant des composantes fréquentielles variant très rapidement. De manière générale l'utilisation des distributions généralisées à temps complexe présente un cadre d'analyse adéquat, mais il est limité aux signaux possédant une bande passante étroite, nous proposons dans une première partie d'étendre cette utilisation à des signaux possédant une bande passante plus large en appliquant un changement d'échelle des signaux. Une deuxième partie s'intéressera davantage à l'extraction de signaux à modulation de phase dans le contexte d'un mélange de bruit non-stationnaire et d'autres signaux cohérents. Ceci sera effectué par des opérateurs de warping couplé à des techniques de débruitage basée sur la compression de données. Le troisième chapitre s'intéressera aux techniques guidées par les données basées sur la représentation des signaux en diagrammes de phase. La contribution principale porte sur la diversité des lags qui permet en effet de mettre en évidence les effets des opérateurs de temps-échelles, mais aussi de modification d'amplitude entre des signaux. Nous développerons donc des méthodes permettant de mettre en évidence ces propriétés. Finalement, les travaux présentés dans les premiers chapitres seront développés dans le cadre de quatre domaines applicatifs qui sont : la segmentation d'ECG, la caractérisation de transitoires électriques, un cas d'acoustique passive et l'étude de signaux acoustiques en milieu immergé. Nous terminerons enfin par une conclusion et quelques perspectives de travail.
Mots clés : Transitoire, Caractérisation, Analyse de signaux, Non-stationnarité

Abstract — For their uniqueness, transient are really difficult to characterize. They are met everywhere and are generally the result of very complex physical phenomena that contain a lot of information such as the transient at its origin, the effect of the propagation through the medium and the effects induced by the transducers. They can correspond to communication between mammals as well as being the reflection of a fault in electrical or hydraulic networks for instance. Hence their study is of great importance even though it is quite complicated. Numerous signal processing methods have been developed in the last decades: they often rely on statistical approaches, linear projections of the signal onto dictionaries and data-driven techniques. All those methods have pros and cons since they often provide good detections, nevertheless their characterization for classification and discrimination purposes remains complicated. In this spirit, this thesis proposes new approaches to study transients. After a brief overview of the existing methods, this work first focuses on the representation of signals having fast-varying time-frequency components. Generally, general complex-time distributions present a proper framework to study them but remain limited to narrow band signals. In a first part, we propose to overcome this limitation in the case of signals with a spread time-frequency variation. This method is based on the compression of the signal's spectrum to a bandwidth that ensures the efficiency of the technique. A second part then focuses on the extraction of nonlinear modulation phase signals in the context of nonstationary noise and other coherent signals. This is performed with warping operators and compressive sensing reconstruction techniques. The third chapter then focuses on data-driven methods based on the representation of the signal in phase space. The main contribution takes advantage of the lag diversity that enables to highlight time scale transformations as well as amplitude modifications between transients. Hence, we develop different techniques enabling to highlight those properties. Finally, works presented in the first chapters are developed in applicative contexts such as: ECG segmentation, electrical transient characterization, a passive acoustic configuration and the study of acoustic signals in an immerse environment. We then end up by some conclusions and perspectives for future works.
Keywords: Transient, Characterization, Signal Analysis, Non-stationarity

GIPSA-lab, 11 rue des Mathématiques, Grenoble Campus
Saint Martin d'Hères